TAMPEREEN TEKNILLINEN YLIOPISTO
TAMPERE UNIVERSITY OF TECHNOLOGY

Antti Rantamäki

Scaling the Power and Tailoring the Wavelength of Semiconductor Disk Lasers

Julkaisu 1286 • Publication 1286

Tampere 2015

Tampereen teknillinen yliopisto. Julkaisu 1286
Tampere University of Technology. Publication 1286

Antti Rantamäki

Scaling the Power and Tailoring the Wavelength of Semiconductor Disk Lasers

Thesis for the degree of Doctor of Science in Technology to be presented with due permission for public examination and criticism in Sähkötalo Building, Auditorium S2, at Tampere University of Technology, on the 20th of March 2015, at 12 noon.

Tampereen teknillinen yliopisto - Tampere University of Technology
Tampere 2015

ISBN 978-952-15-3480-5 (printed)
ISBN 978-952-15-3489-8 (PDF)
ISSN 1459-2045

Abstract

Optically pumped semiconductor disk lasers (SDLs) provide a unique combination of high output power, high beam quality and possible emission wavelengths spanning from the ultraviolet to the mid-infrared spectral range. In essence, SDLs combine the wavelength versatility of semiconductor gain media with the power scaling principles of optically pumped solid state disk lasers. The emission wavelength of SDLs can be tailored to match the desired application simply by altering the composition of the gain material. High power operation, however, requires efficient thermal management, which can be realized using thin structures that are integrated with industrial diamond heat spreaders.

The main objective of this thesis was to develop methods for increasing the output power of optically pumped SDLs, especially in challenging wavelength regions. The work included integrating SDL gain elements onto diamond heat spreaders using thin intermediate gold layers. This configuration enabled 45–50 % higher output powers than conventional bonding with indium solder. In addition, the reflectivity of the SDL gain mirror was enhanced using a semiconductor-dielectric-metal compound mirror. This procedure enabled 30 % thinner mirror structures when compared with the conventional design, where the reflectivity of the semiconductor mirror is enhanced with a metal layer. Finally, thin GaAs-based semiconductor mirrors were integrated with InP-based active regions. Such integration is necessary for high power operation in the spectral range 1.3–1.6 μm, because InP-based compounds for a highly reflective thin mirror section are not available. The configuration enabled record-high output powers of 6.6 W and 4.6 W at the wavelengths of 1.3 μm and 1.58 μm, respectively.

The second objective of this thesis was to generate high output powers in single-frequency operation and via intracavity frequency-doubling. In single-frequency opera-

tion, record-high output powers of 4.6 W and 1 W were demonstrated at the wavelengths of 1.05 μm and 1.56 μm, respectively. Such light sources are required for numerous applications including free-space communications and high resolution spectroscopy. In addition, second-harmonic generation was demonstrated with SDLs emitting at 1.3 μm and 1.57 μm. The output powers reached 3 W at 650 nm and 1 W at 785 nm, which represent record-high output powers from SDLs in this wavelength range. These types of lasers could be especially useful in biophotonics and medical applications.

Acknowledgements

The work presented in this thesis was carried out at the Optoelectronics Research Centre (ORC), Tampere University of Technology, during the years 2010–2014. I want to express my gratitude to my supervisor, Professor Oleg Okhotnikov, for his support during this work. I also want to thank the former director of ORC Professor Emeritus Markus Pessa and the current director of ORC Pekka Savolainen for giving me the opportunity to work at ORC. The assistance provided by Professor Mircea Guina and Professor Mika Valden is also acknowledged. The development manager Anne Viherkoski and secretary Eija Heliniemi are recognized for handling the administrative work.

I want to thank all my co-workers at ORC. Notable recognition goes to Esa Saarinen and Alexander Chamorovskiy for innumerable valuable discussions and the help that they provided. Alexander Chamorovskiy was also the best officemate I could have had, so cheers to the years we spent together. Warm thanks also to my optics lab colleagues Jari Nikkinen, Jussi Rautiainen, Juho Kerttula, Regina Gumenyuk, Samuli Kivistö, Antti Härkönen, Tomi Leinonen and Lasse Orsila. You were always there for me if I needed your help.

I gratefully acknowledge the considerable amount of help that I received from my processing fellows Jukka Lindfors, Marko Silvennoinen, Maija Karjalainen, Mariia Bister, Pirjo Leinonen, Juha Kontio, Jussi-Pekka Penttinen, Juha Tommila, Kimmo Haring and Kimmo Lahtonen. The crystal growers Jari Lyytikäinen, Miki Tavast, Sanna Ranta and Ville-Markus Korpijärvi are also acknowledged for their contribution. Without you, this work would not have been possible. The guys in the mechanical workshop are acknowledged for always being in good spirits and ready to offer their help. Thanks also to Charis Reith for proofreading the thesis. The remaining typos were added by the author

afterwards.

The collaborators at École Polytechnique Fédérale de Lausanne are acknowledged for their expertise in wafer fusion and semiconductor growth.

The pre-reviewers Professor Anders Larsson and Assistant Professor Arash Rahimi-Iman are gratefully acknowledged for their insightful comments and for taking the time to review my thesis.

Finally, I want to thank my family and friends for the support they have given me. Special notion goes to Tarmo Äijö for the long evenings we spent in scientific(ish) discussions. I'm also very grateful to Petra for all the support and patience she showed me during this work.

Tampere, March 2015
Antti Rantamäki

Contents

Abstract i

Acknowledgements iii

Contents v

List of publications viii

Author's contribution x

List of abbreviations and symbols xi

1 Introduction 1

1.1 Background . . . 1

1.2 The scope of the thesis . . . 2

2 Semiconductor disk lasers 5

2.1 Introduction . . . 5

2.2 SDL configuration . . . 8

2.2.1 The gain section . . . 8

2.2.2 The DBR section . . . 9

2.2.3 Resonant periodic gain structure . . . 10

2.3 Thermal management . . . 11

2.4 The cavity and pump configuration . . . 13

2.5 Wavelength coverage . . . 14

3 **Flip-chip semiconductor disk lasers with GaAs-based active regions** **16**
3.1 Introduction 16
3.1.1 Reliability 16
3.1.2 Thermal conductance 17
3.1.3 Residual stress 17
3.2 Low temperature Au-Au thermocompression bonding 18
3.3 Semiconductor-dielectric-metal compound mirrors 21
3.3.1 Enhancing the DBR reflectivity 21
3.3.2 SDLs with GaAs/AlAs-Al_2O_3-Al compound mirrors 22
3.4 Single-frequency operation 27
3.4.1 Longitudinal modes in SDLs 27
3.4.2 Properties of single-frequency SDLs 28
3.4.3 Single-frequency SDL emitting at 1.05 μm 29

4 **Semiconductor disk lasers with InP-based active regions** **33**
4.1 Introduction 33
4.2 Wafer bonding 34
4.2.1 Direct bonding with Si-based materials 34
4.2.2 Direct bonding with III-V materials 35
4.2.3 Bonding of III-V materials with intermediate Si-based layers . . 35
4.3 SDLs in the 1.3 μm wavelength band 36
4.3.1 Wafer-fused SDLs emitting at 1.27–1.31 μm 37
4.3.2 Wafer-bonded SDLs emitting at 1.32 μm 39
4.4 SDLs in the 1.5 μm wavelength band 41
4.4.1 Wafer-fused SDL emitting at 1.58 μm 41
4.4.2 Single-frequency wafer-fused SDL emitting at 1.56 μm 42

5 **Frequency conversion in semiconductor disk lasers** **45**
5.1 Introduction 45
5.2 Nonlinear frequency conversion in SDLs 45
5.3 Second-harmonic generation 46
5.4 Intracavity second-harmonic generation 51
5.5 Intracavity second-harmonic generation with 1.3–1.6 μm SDLs 52
5.5.1 Frequency-doubled SDL at 650 nm 53

5.5.2 Frequency-doubled SDL at 785 nm 54

6 Conclusion **56**

Bibliography **58**

List of publications

[P1] A. Rantamäki, J. Lindfors, M. Silvennoinen, J. Kontio, M. Tavast, and O. Okhotnikov, "Low temperature gold-to-gold bonded semiconductor disk laser," *IEEE Photonics Technology Letters*, vol. 25, no. 11, pp. 1062–1065, 2013.

[P2] A. Rantamäki, E. Saarinen, J. Lyytikäinen, K. Lahtonen, M. Valden, and O. Okhotnikov, "High power semiconductor disk laser with a semiconductor-dielectric-metal compound mirror," *Applied Physics Letters*, vol. 104, no. 10, pp. 101 110:1–101 110:4, 2014.

[P3] A. Rantamäki, A. Chamorovskiy, J. Lyytikäinen, and O. Okhotnikov, "4.6-W single frequency semiconductor disk laser with < 75 kHz linewidth," *IEEE Photonics Technology Letters*, vol. 24, no. 16, pp. 1378–1380, 2012.

[P4] A. Rantamäki, A. Sirbu, E. Saarinen, J. Lyytikäinen, A. Mereuta, V. Iakovlev, E. Kapon, and O. Okhotnikov, "High-power flip-chip semiconductor disk laser in the 1.3 μm wavelength band," *Optics Letters*, vol. 39, no. 16, pp. 4855–4858, 2014.

[P5] A. Rantamäki, J. Lyytikäinen, J. Heikkinen, J. Kontio, and O. Okhotnikov, "Multi-watt semiconductor disk laser by low temperature wafer bonding," *IEEE Photonics Technology Letters*, vol. 25, no. 22, pp. 2233–2235, 2013.

[P6] A. Rantamäki, J. Rautiainen, A. Sirbu, A. Mereuta, E. Kapon, and O. Okhotnikov, "1.56 μm 1 watt single frequency semiconductor disk laser," *Optics Express*, vol. 21, no. 2, pp. 2355–2360, 2013.

[P7] A. Rantamäki, A. Sirbu, A. Mereuta, E. Kapon, and O. Okhotnikov, "3 W of 650 nm red emission by frequency doubling of wafer-fused semiconductor disk laser," *Optics Express*, vol. 18, no. 21, pp. 21 645–21 650, 2010.

[P8] A. Rantamäki, J. Rautiainen, J. Lyytikäinen, A. Sirbu, A. Mereuta, E. Kapon, and O. Okhotnikov, "1 W at 785 nm from a frequency-doubled wafer-fused semiconductor disk laser," *Optics Express*, vol. 20, no. 8, pp. 9046–9051, 2012.

Author's contribution

The author built the experimental setup and made the measurements in all the publications. In addition, the processing steps in publications [P1–P3, P5] were developed and performed by the author. However, the author also benefited from the work of various co-authors, especially in growing the semiconductor structures, the wafer fusion process, the Al_2O_3 deposition and the fiber optics used for characterization. The author also received general guidance in processing related issues. A summary of the author's contribution to the research work and manuscript preparation is given in the table below.

Paper #	Contribution to research work	Contribution to writing the paper
P1	Group work (80 %)	Main author
P2	Group work (80 %)	Main author
P3	Group work (60 %)	Main author
P4	Group work (60 %)	Main author
P5	Group work (60 %)	Main author
P6	Group work (80 %)	Main author
P7	Group work (70 %)	Main author
P8	Group work (70 %)	Main author

Table 1: Author's contribution to the papers included in the dissertation.

List of abbreviations and symbols

Abbreviations

Ag	Silver
Al	Aluminium
AlAs	Aluminium-arsenide
AlGaAs	Aluminium-gallium-arsenide
AlGaInAs	Aluminium-gallium-indium-arsenide
Al_2O_3	Aluminium oxide
AOM	Acousto-optic modulator
AR	Anti-reflection
ASE	Amplified spontaneous emission
Au	Gold
AuGe	Gold-germanium
AuIn	Gold-indium
AuSi	Gold-silicon
AuSn	Gold-tin
$Au_{80}Sn_{20}$	Eutectic gold-tin
BaF_2	Barium fluoride
BBO	Beta barium borate
CPM	Critical phase matching
Cr	Chromium
CSL	Current spreading layer
CTE	Coefficient of thermal expansion
Cu	Copper
CVD	Chemical vapor deposition

CW	Continuous wave
DBR	Distributed Bragg reflector
DFG	Difference-frequency generation
DSHI	Delayed self-heterodyne interferometer
EP-SDL	Electrically pumped semiconductor disk laser
EP-VECSEL	Electrically pumped vertical-external-cavity surface-emitting laser
FCA	Free carrier absorption
FPI	Fabry–Pérot interferometer
FWHM	Full-width at half maximum
GaAs	Gallium-arsenide
GaInP	Gallium-indium-phosphide
GaInAsP	Gallium-indium-arsenide-phosphide
GaInNAs	Gallium-indium-nitrogen-arsenide
GaN	Gallium-nitride
GaSb	Gallium-antimonide
H_2	Hydrogen
HCl	Hydrochloric acid
HF	Hydrofluoric acid
H_2O	Water
HR	High-reflective
IC	Integrated circuit
ICOPO	Intracavity optical parametric oscillator
In	Indium
InAs	Indium-arsenide
InGaAs	Indium-gallium-arsenide
InGaAsP	Indium-gallium-arsenide-phosphide
InP	Indium-phosphide
LBO	Lithium triborate
LIDAR	Light detection and ranging
M_i	Optical cavity mirrors with $i = 1, 2, 3$
MBE	Molecular beam epitaxy
MEMS	Micro-electro-mechanical system
MOVPE	Metalorganic vapor phase epitaxy
MPTMS	(3-Mercaptopropyl)trimethoxysilane

NCPM	Noncritical phase matching
NH_2	Amino group
NH_4OH	Ammonium hydroxide
OC	Output coupler
OH	Hydroxyl group
OPSL	Optically pumped semiconductor laser
ORC	Optoelectronics Research Centre
P	Phosphorus
PIC	Photonic integrated circuit
PL	Photoluminescence
Pt	Platinum
QD	Quantum dot
QW	Quantum well
RF	Radio frequency
RoC	Radius of curvature
RPG	Resonant periodic gain
SAM	Self-assembled monolayer
SDL	Semiconductor disk laser
SEM	Scanning electron microscope
SESAM	Semiconductor saturable absorber mirror
SFG	Sum-frequency generation
SH	Thiol group
SHB	Spatial hole burning
SHG	Second-harmonic generation
Si	Silicon
SiO_2	Silicon dioxide
Sn	Tin
SOI	Silicon-on-insulator
TDL	Thin disk laser
TEM	Transverse electromagnetic mode
Ti	Titanium
TiO_2	Titanium dioxide
UV	Ultraviolet
VCSEL	Vertical-cavity surface-emitting laser

VECSEL	Vertical-external-cavity surface-emitting laser

Symbols, Greek alphabet

α	Linewidth enhancement factor
α_{loss}	Total losses in an optical cavity
Γ_g	Gain or filter bandwidth
δ	Linear loss in an optical cavity
ε_0	Permittivity
$\mathcal{F}$	Finesse of an optical cavity
θ	Propagation angle in second-harmonic generation
κ	Nonlinear coupling coefficient in second-harmonic generation
κ_{hs}	Thermal conductivity of a heat sink
κ_{max}	Optimal value of the nonlinear coupling coefficient
κ_{se}	Thermal conductivity of a semiconductor structure
λ	Wavelength
$\Delta\lambda$	Bandwidth in wavelength domain
λ_1	Wavelength of the fundamental field in second-harmonic generation
λ_2	Wavelength of the second-harmonic field in second-harmonic generation
λ_B	Center wavelength of a distributed Bragg reflector
$\Delta\lambda_B$	Reflectivity bandwidth of a distributed Bragg reflector
λ_t	Target wavelength in a resonant periodic gain structure
ν	Optical frequency
$\Delta\nu_c$	Longitudinal mode linewidth in an optical cavity
$\Delta\nu_{FSR}$	Free spectral range of an optical cavity in frequency domain
$\Delta\nu_G$	Linewidth for a Gaussian spectral distribution
$\Delta\nu_{gain}$	Gain bandwidth
$\Delta\nu_L$	Linewidth for a Lorentzian spectral distribution
χ^n	n-th order susceptibility
σ_{em}	Emission cross section
τ_c	Coherence time of a laser
τ_{char}	Characteristic time of a laser
τ_d	Delay time in delayed self-heterodyne interferometer
τ_f	Fluorescence or upper state lifetime
τ_{ph}	Photon lifetime in an optical cavity
ω_1	Optical angular frequency for the fundamental frequency

ω_2	Optical angular frequency for the second-harmonic frequency

Symbols, other

A_1	Slowly varying amplitude for the fundamental frequency
A_2	Slowly varying amplitude for the second-harmonic frequency
c	Speed of light
d	Thickness
d_{eff}	Effective nonlinear coefficient
E_1	Electric field for the fundamental frequency
E_2	Electric field for the second-harmonic frequency
E_{c}	Conduction band energy
E_{g}	Bandgap energy
E_{QW}	Bandgap energy, quantum well
E_{v}	Valence band energy
g_0	Unsaturated small-signal round-trip gain
h	Boltzmann constant
I_1	Intensity of the fundamental field
$I_{1,\mathrm{ge}}$	Intensity of the fundamental field in the gain element
$I_{1,\mathrm{nc}}$	Intensity of the fundamental field in the nonlinear crystal
I_2	Intensity of the second-harmonic field
I_{S}	Saturation intensity
k	Wave vector
Δk	Phase mismatch in second-harmonic generation
k_1	Wave vector for the fundamental frequency
k_2	Wave vector for the second-harmonic frequency
L_{c}	Coherence length in second-harmonic generation
L_{cav}	Optical cavity length
$L_{\mathrm{coh,\,G}}$	Coherence length for a Gaussian spectral distribution
$L_{\mathrm{coh,\,L}}$	Coherence length for a Lorentzian spectral distribution
M^2	Beam quality parameter
N	Number of layer pairs in a distributed Bragg reflector
n	Refractive index

n_1	Refractive index for the fundamental frequency
n_2	Refractive index for the second-harmonic frequency
n_{e}	Refractive index in the extraordinary polarization direction
n_{H}	High refractive index in a distributed Bragg reflector
n_{i}	Refractive index of the surrounding medium
n_{L}	Low refractive index in a distributed Bragg reflector
n_{o}	Refractive index in the ordinary polarization direction
n_{sp}	Spontaneous emission factor
$P^{(\mathrm{n})}$	n-th order polarization
P_{out}	Output power
R	Reflectivity
R_{th}	Thermal resistance
$S(\nu)$	Power spectrum
T	Temperature
t	Time
ΔT	Temperature difference
T_{rt}	Round-trip time of an optical cavity
w_{cr}	Critical pump radius
z	Distance

Chapter 1

Introduction

1.1 Background

Electrically pumped semiconductor lasers have become the most common type of laser, because they offer a unique combination of low power consumption, small size, mass-scale fabrication and possible emission wavelengths spanning from the ultraviolet to the terahertz range. These lasers are found in many common devices such as DVD players, laser printers and barcode scanners, but also in fields such as medicine and optical communications. However, the beam quality of these lasers degrades at high power levels, which is a drawback in applications that require long propagation distances with minimal beam divergence or focusing of a high power beam onto a small spot. Therefore, high power semiconductor lasers are often used in applications that have relaxed requirements for the beam quality, such as welding and optical pumping of solid state lasers.

On the other hand, a combination of high power and good beam quality is required in several applications that include remote sensing, metrology, medicine and laser displays. These requirements can be met by solid state lasers and gas lasers. However, specific additional requirements for the operation wavelength are problematic for these lasers, because their operation wavelengths are limited to the discrete emission lines of the available active materials.

The work presented in this thesis focuses on a particular type of semiconductor laser called the semiconductor disk laser (SDL). These lasers are also known as vertical-external-cavity surface-emitting lasers (VECSELs), or simply optically pumped semi-

conductor lasers (OPSLs) [1]. SDLs combine the power scaling principles originally developed for solid state lasers [2] with the wavelength versatility of semiconductor lasers [3]. Consequently, SDLs are capable of providing a unique combination of multi-watt output powers, high beam quality, and emission at the desired wavelength. SDLs are also very suitable for single-frequency operation and nonlinear frequency conversion when compared with solid state lasers, gas lasers or other types of semiconductor lasers [4–9]. These features have enabled SDLs to find use in several fields such as metrology, medicine, life sciences, the movie industry and optical pumping of certain solid state materials [10–13].

1.2 The scope of the thesis

The main objective of this thesis was to develop methods for increasing the output power of optically pumped semiconductor disk lasers (SDLs), especially in challenging wavelength regions. This task required efficient thermal management of the SDL gain structures, because the output power of these lasers is limited by pump-induced heating. In particular, the excess heat is most effectively removed from thin structures with high thermal conductances. This issue was addressed by developing processes for

- integrating SDL gain elements onto chemical vapor deposition (CVD) diamond heat spreaders using very thin intermediate layers,
- enhancing the reflectivity of the mirror section and thereby enabling thinner mirror structures, and
- integrating thin GaAs-based mirrors onto InP-based active regions.

The first two issues are essential for SDLs utilizing the so called flip-chip configuration for thermal management, which is preferred for several SDL applications. The last issue is essential for InP-based SDLs emitting in the wavelength range 1.25–1.7 μm, because high-reflective thin mirror sections cannot be fabricated using InP-based compounds. Special attention was paid to the processing temperature, because low temperature processes offer relaxed requirements for matching of the coefficients of thermal expansion (CTE) between disparate materials.

As for the spectral versatility, the emission wavelength of the demonstrated InP-based SDLs can be tailored by controlling the material composition of the gain element. Such wavelength flexibility is not available from solid state lasers in the wavelength

range 1.25–1.7 μm, due to the lack of appropriate gain materials [14]. Furthermore, InP-based SDLs enable emission in the wavelength range 625–800 nm via intracavity frequency-doubling. Consequently, they avoid the drawbacks of directly emitting SDLs at wavelengths below 800 nm. These drawbacks include mirror sections with relatively low thermal conductivities, temperature-sensitive gain regions that hinder high power operation, and the requirement for pump lasers emitting in the visible wavelength range. Therefore, frequency-doubled InP-based SDLs can provide an alternative to the expensive and bulky titanium-sapphire lasers when a broad wavelength tunability is not required [15].

The main properties and operation principles of SDLs are presented in Chapter 2. The discussion is opened by comparing SDLs with electrically pumped semiconductor lasers and optically pumped solid state thin disk lasers (TDLs), because SDLs combine the benefits of both laser types. This is followed by an introduction to the functional components and the thermal management of SDLs. The optical pumping and external cavity configurations of SDLs are described next. The chapter is concluded with a review of the wavelength coverage of SDLs.

Chapter 3 presents the results that were obtained with GaAs-based structures emitting at wavelengths close to 1 μm. The chapter devotes special attention to the thermal management of SDLs using the so called flip-chip configuration. In this scheme, a thin semiconductor chip is covalently bonded onto a CVD diamond heat spreader. The bonding is preferably performed at a low temperature to prevent excessive residual stress in the assembly. Furthermore, the bonding should be performed with thin intermediate layers to minimise the thermal resistance of the structure, and with materials that can withstand high power operation. All these requirements are fulfilled by gold-gold thermocompression bonding, which was demonstrated to enable 45–50 % higher output powers than conventional bonding with indium. Chapter 3 also presents a procedure for reducing the thickness of the SDL mirror section. This is accomplished by finishing the SDL mirror section with a thin dielectric layer and a highly reflecting metal layer. The design is demonstrated to enable 30 % thinner mirror structures when compared with the conventional design, where the semiconductor mirror is finished with a highly reflecting metal layer. The chapter is concluded with a review on single-frequency SDLs, and the demonstration of an output power of 4.6 W in single-frequency operation at a wavelength of 1.05 μm, which was a record at the time.

Chapter 4 covers wafer-fused and wafer-bonded SDLs emitting at the wavelengths of 1.3 μm and 1.6 μm. In these SDLs, the gain structure was fabricated by integrating InP-based gain sections with GaAs-based mirror sections. The discussion is started by introducing the basic concepts of wafer bonding using Si-based materials. These concepts are then utilized in a review of the special features and requirements for direct III-V semiconductor wafer bonding, also known as wafer fusion. The introductory part is concluded by a presentation of low temperature wafer bonding methods for III-V semiconductors using thin Si-based intermediate layers. The experimental section includes SDLs fabricated with wafer fusion at 650 °C, wafer bonding at 200 °C using Si-based intermediate layers, and wafer bonding at 200 °C using a self-assembling monolayer (SAM). The wafer fusion processes were performed at École Polytechnique Fédérale de Lausanne in Switzerland, while the last two processes were developed by the author. The three methods enabled multi-watt output powers at the wavelengths of 1.3 μm and 1.6 μm. Furthermore, record-high output powers were demonstrated with 6.6 W at 1.3 μm, 4.6 W at 1.58 μm and 1 W in single-frequency operation at 1.56 μm.

Chapter 5 begins with a review of nonlinear frequency conversion in SDLs. This is followed by an introduction to intracavity second-harmonic generation, where a nonlinear crystal is placed inside the laser cavity. The chapter is concluded by a presentation of second-harmonic generation with SDLs emitting at the wavelengths 1.3 μm and 1.58 μm. The frequency-converted output powers reach of 3 W at 650 nm and 1 W at 785 nm, which represent the highest output powers reported from SDLs in this wavelength range.

Chapter 2

Semiconductor disk lasers

Semiconductor disk lasers (SDLs) are essentially brightness and wavelength converters that transform low-brightness light from pump diodes into a high-brightness output beam at the desired wavelength. This chapter provides an overview of the operation principles of SDLs by comparing them with other types of semiconductor lasers and optically pumped solid state thin disk lasers (TDL)s. The chapter is concluded with a presentation of the functional blocks, cavity configuration, power scaling and wavelength coverage of SDLs.

2.1 Introduction

A schematic diagram of an edge-emitting semiconductor diode laser is shown in Fig. 2.1(a). The device is pumped by injecting electric current into the narrow stripe on top of the structure that confines the carriers in the horizontal direction. As the current flows through the structure, light is emitted in the plane of the active region that is marked by the dark area in the figure. The generated light is then horizontally guided by the surrounding layers in the vertical direction and emitted from the edge of the device. Due to the small and asymmetric emission apertures of these devices, their output beams are highly divergent and asymmetrical. The small emission aperture can also lead to catastrophic optical damage at the emission edge of the diode, while a small active region volume can lead to excessive device heating. Both problems can be alleviated by increasing the stripe width, which allows lower optical intensities and lower heat densities within the diode. However, such an approach also deteriorates the quality of the output

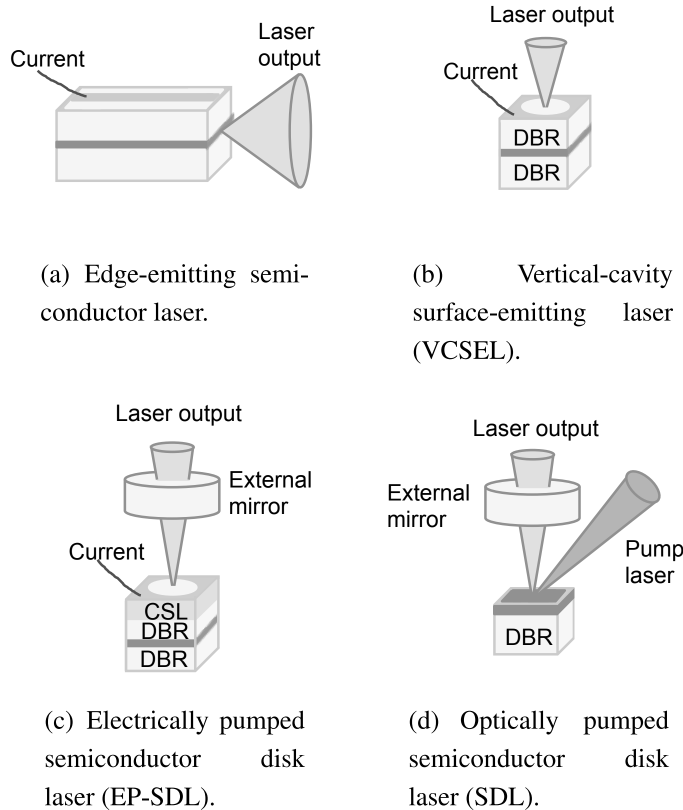

(a) Edge-emitting semiconductor laser.

(b) Vertical-cavity surface-emitting laser (VCSEL).

(c) Electrically pumped semiconductor disk laser (EP-SDL).

(d) Optically pumped semiconductor disk laser (SDL).

Figure 2.1: Schematic diagrams of semiconductor lasers. The dark region represents the gain region in all cases. DBR - distributed Bragg reflector, CSL - current spreading layer.

beam.

Vertical-cavity surface-emitting lasers (VCSELs) emit light from the surface of the device, as illustrated in Fig. 2.1(b). In this case, the thin active region in is embedded between two semiconductor distributed Bragg reflector (DBR) mirrors. The device is pumped by injecting electric current into the small top-aperture of the device. Since the volume of the active region is orders of magnitude smaller than in edge-emitting laser diodes, the threshold currents are significantly lower. The symmetrical apertures also allow VCSELs to produce output beams with low divergence and circular profiles. These devices are widely used in applications that require low output powers, high modulation speeds, high quality output beams and low power consumption [16]. However, VCSEL arrays have also been utilized to generate high output powers, though only with poor

beam qualities [17].

Electrically pumped semiconductor disk lasers (EP-SDLs), or electrically pumped vertical-external-cavity surface-emitting lasers (EP-VECSELs), are similar to VCSELs. However, in EP-SDLs the top DBR is less-reflective than in VCSELs, and the laser cavity is completed with at least one external mirror, as shown in Fig. 2.1(c). EP-SDLs also have larger emission apertures than VCSELs, and therefore require additional current spreading layers (CSLs). These arrangements increase the complexity of the laser, but the external cavity also allows [18–20]

- the properties of the laser beam to be controlled and therefore power scaling with high quality output beams, and
- the utilization of intracavity optical elements such as optical filters for wavelength selection, nonlinear crystals for frequency conversion and saturable absorbers for mode-locked operation.

However, the performance of EP-SDLs is limited by a fundamental trade-off between electrical and optical losses: the electrical resistance can be reduced by increasing the doping level, but the consequent increase in free carrier absorption (FCA) increases the optical losses [21–23]. A more suitable approach for high power operation is provided by optical pumping, which enables [24]

- uniform excitation to be created on a large area of the gain element, which is essential for obtaining high beam quality,
- doped layers in the structure to be avoided, and therefore reduced free carrier absorption losses,
- electrical power loss from parasitic electrical resistance to be avoided, and
- carrier transport limitations in thick gain structures to be circumvented.

A schematic diagram of an optically pumped SDL is shown in Fig. 2.1(d). These devices resemble solid state TDLs, which are known for providing high output powers without compromising the beam quality [25]. However, they also have several disparities. For instance, the operation wavelength of solid state TDLs is limited to the discrete emission lines of the available materials, whereas the emission wavelength of SDLs is determined by bandgap engineering. This is a clear advantage of SDLs, because their emission wavelength can be tailored to match specific applications. Another advantage of SDLs is related to the requirements for the diode pump lasers. Solid state materials

usually require pumping at specific wavelengths that correspond to the narrow absorption lines of the given materials. There is no such restriction associated with SDLs, because the pump photon energy only needs to exceed the bandgap of the pump absorbing layers [6]. Solid state TDLs also require optics for recirculating the residual pump radiation, because only a fraction of the pump light is absorbed in a single pass through the 100–300 μm thick gain section [2, 25]. SDLs do not require such arrangements, because up to 90% of the pump radiation can be absorbed in a single pass through 2 μm of semiconductor material. Furthermore, the DBR can be designed to reflect the pump radiation, which essentially doubles the pump absorption length and allows even thinner SDL structures to be utilized [26].

2.2 SDL configuration

Optically pumped SDLs and solid state TDLs both comprise a gain section on top of a mirror section. However, in solid state TDLs the gain section is uniform, whereas in SDLs it comprises several disparate functional layers. The gain section and the DBR section also form a so called resonant periodic gain (RPG) structure in SDLs. These concepts are introduced in the following sections.

2.2.1 The gain section

The periodic atomic structure of semiconductors confines the carriers to a valence band E_{v} and a conduction band E_{c}, which are illustrated in Fig. 2.2. The separation of these bands is called the bandgap energy E_{g}. It corresponds to the minimum energy that has to be provided by the pump laser to excite electrons from the valence band to the conduction band.

Upon pumping, the excited electrons in the spacer and barrier layers diffuse into the lower energy states in the quantum wells (QWs). The electrons then drop back into the valence band and may emit light at a wavelength corresponding to the QW energy E_{QW}. The window layer on top of the structure prevents the carriers from reaching the gain element surface, where they would be lost to non-radiative recombination. Some structures also include a cap layer that protects the window layer from oxidation.

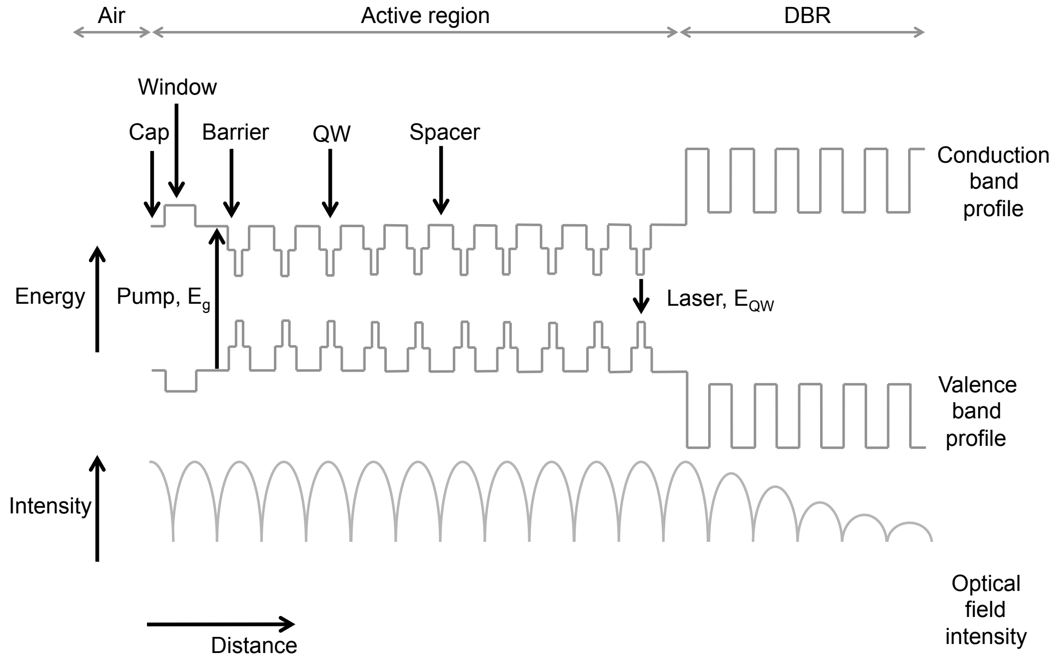

Figure 2.2: A schematic diagram of an SDL structure with 10 QWs and a DBR.

2.2.2 The DBR section

The DBR section comprises a periodic stack of transparent semiconductor layers with high and low refractive indices denoted by n_{H} and n_{L}. The DBR operation is based on the fact that a portion of the incoming light is reflected at each layer boundary, and that light reflected from the low refractive index layer experiences an additional phase shift of 180°. These reflections reinforce one another through constructive interference if the optical thickness of each layer corresponds to one quarter of a full wavelength

$$d = \frac{\lambda_{\mathrm{B}}}{4n(\lambda_{\mathrm{B}})}, \tag{2.1}$$

where λ_B is the center wavelength and $n(\lambda_{\mathrm{B}})$ the corresponding refractive index. If the DBR is formed on a substrate with a refractive index n_{s}, the DBR reflectivity at the center wavelength λ_{B} is given by [27]

$$R_{2\mathrm{N}}(\lambda_{\mathrm{B}}) = \left(\frac{1 - \left(\frac{n_{\mathrm{s}}}{n_{\mathrm{i}}}\right)\left(\frac{n_{\mathrm{H}}}{n_{\mathrm{L}}}\right)^{2\mathrm{N}}}{1 + \left(\frac{n_{\mathrm{s}}}{n_{\mathrm{i}}}\right)\left(\frac{n_{\mathrm{H}}}{n_{\mathrm{L}}}\right)^{2\mathrm{N}}} \right)^2 \tag{2.2}$$

for a structure with an even number of layers (2N), and by

$$R_{2N+1}(\lambda_B) = \left(\frac{1 - \left(\frac{n_H}{n_i}\right)\left(\frac{n_H}{n_s}\right)\left(\frac{n_H}{n_L}\right)^{2N}}{1 + \left(\frac{n_H}{n_i}\right)\left(\frac{n_H}{n_s}\right)\left(\frac{n_H}{n_L}\right)^{2N}} \right)^2 \tag{2.3}$$

for a structure with an odd number (2N+1) of layers. The letter N refers to the number of DBR layers and n_i denotes the refractive index of the surrounding medium. The refractive indices of the substrate and the surrounding material determine whether an even or an odd number of DBR layer pairs is chosen. For maximized reflectivity, the DBR should start and end with a layer that provides the highest refractive index contrast to the surrounding material. The bandwidth of the DBR is determined by the refractive index contrast between the DBR layers, and is given by [28]

$$\Delta\lambda_B = \frac{4\lambda_B}{\pi} \arcsin\left(\frac{1 - \frac{n_L}{n_H}}{1 + \frac{n_L}{n_H}} \right). \tag{2.4}$$

2.2.3 Resonant periodic gain structure

In VCSELs and SDLs, the active region and the DBR section form a resonant periodic gain (RPG) structure [29, 30]. In an RPG structure, the QWs are placed at the antinodes of the standing optical wave at the target wavelength λ_t. Consequently, the excited carriers are confined to the positions of maximum optical intensity, where the interaction between the gain material and the optical field is the strongest.

The optical length of the RPG structure is often chosen as a multiple of $\lambda_t/2$ in order to make the structure resonant at λ_t. Such a resonant structure provides the highest gain, because it increases the optical field confinement within the RPG structure. The most efficient operation is obtained when the resonance wavelength, the QW positioning, the QW peak gain and the DBR center wavelength correspond to the same wavelength, λ_t [31].

However, a resonant design also introduces high group delay dispersion and decreases the gain bandwidth. This can be detrimental e.g. for mode locking [32], wavelength tunability [33] and single-frequency operation [4]. Therefore, the gain structure is sometimes designed to be antiresonant, even though such an approach inevitably reduces the gain and makes the laser more susceptible to cavity losses.

2.3 Thermal management

The main heat sources in SDLs are the energy difference between the pump and the laser photons, called the quantum defect, and non-radiative recombination [34, 35]. The temperature of SDLs increases with pump power and brings forth issues such as an increased amount of non-radiative recombination and reduced material gain [35–39]. In addition, the QW peak gain shifts to longer wavelengths by $\sim$ 0.3–0.5 nm/K, while the optical length of the RPG structure and the DBR center wavelength shift at a rate of $\sim$ 0.1–0.2 nm/K. Consequently, the QW peak gain wavelength cannot match the RPG resonance wavelength or the center of the DBR bandwidth at all pump power levels. Therefore, the QW peak gain is designed to locate at shorter wavelengths than the optical length of the RPG structure at room temperature, so that they coincide at the typical SDL operating temperature [40, 41]. Otherwise, the gain is reduced at low pump powers and the output power remains low [35].

The power scaling of SDLs relates to thermal management and is based on the thin disk approach. This configuration allows efficient cooling, because the cooled area of the disk-shaped gain element is large with respect to its volume. Therefore, the heat flow occurs mainly along the thickness of the disk and is nearly one-dimensional. In an ideal case, the output power can be doubled, without increasing the temperature of the gain element, by doubling the pumped area.

However, this concept of power scaling is eventually limited by lateral heat flow in the heat sink and the gain element [42–44]. In particular, the thermal resistance of the heat sink starts to limit the power scalability beyond a critical pump spot radius given by [42]

$$w_{\mathrm{cr}} = \sqrt{\frac{8}{\pi}\frac{\kappa_{\mathrm{hs}} d}{\kappa_{\mathrm{se}}}}, \tag{2.5}$$

where κ_{hs} is the thermal conductivity of the heat sink, κ_{se} the thermal conductivity of the semiconductor structure and d the thickness of the gain element. Beyond the critical radius, the power scaling becomes increasingly less efficient. Eventually, the threshold pump intensity exceeds the thermal roll-over pump intensity [45]. In addition, the power scaling can be limited by scattering losses, diffraction losses [34, 46–48] and amplified spontaneous emission (ASE) [34, 49, 50]. Nevertheless, additional power scaling can be obtained by using multiple gain elements within the same cavity [45, 51–54].

Thermal management of SDLs is typically achieved by bonding a heat spreader to

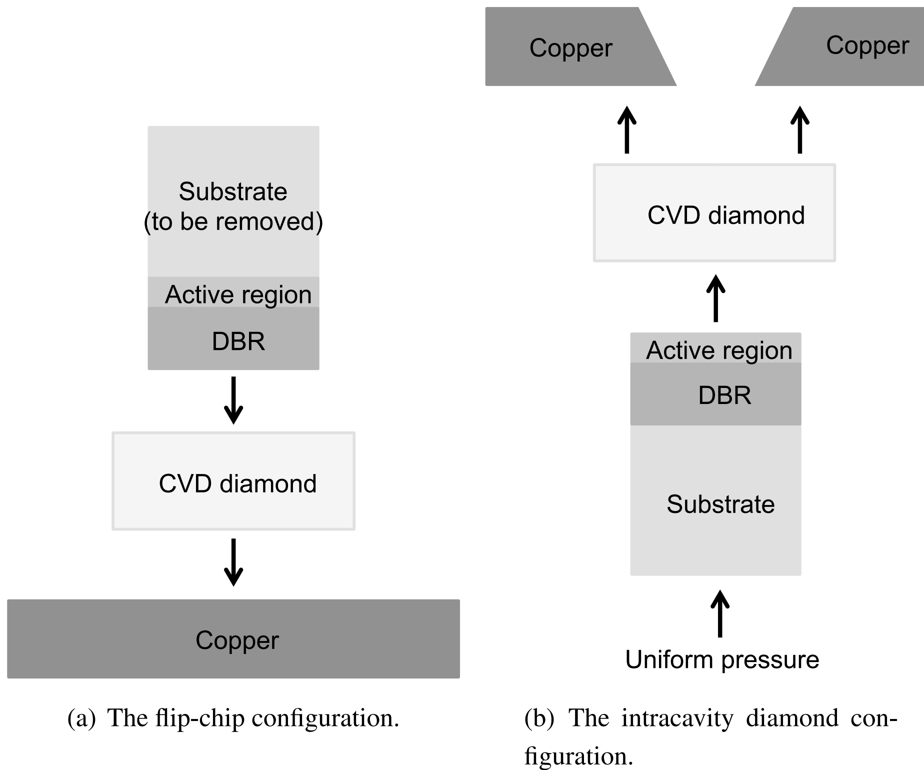

(a) The flip-chip configuration.

(b) The intracavity diamond configuration.

Figure 2.3: Thermal management schematics of semiconductor lasers.

the bottom of the DBR, or by bonding a transparent heat spreader to the top emitting surface of the SDL. These procedures are called the flip-chip approach and the intracavity diamond approach, respectively, with illustrations shown in Figs. 2.3(a) and 2.3(b).

In the flip-chip approach, the SDL structure is usually bonded onto a CVD diamond heat spreader using intermediate metal layers. The substrate is then removed from the top of the structure and the diamond-SDL assembly is bonded onto a water-cooled copper heat sink. The excess heat in the active region is extracted through the DBR section, so the thermal conductivity of the DBR section is essential in this configuration.

In the intracavity diamond heat spreader configuration, the as-grown structures are simply capillary bonded onto the diamond heat spreaders at room temperature using water or alcohol [55]. The assembly is kept intact during laser operation by applying uniform mechanical pressure from the bottom of the SDL chip. In this case, the excess heat is extracted directly from the active region, so the thermal conductivity of the DBR is less critical. The top surface of the intracavity diamond is often completed with an an-

tireflection (AR) coating to reduce the pump and signal reflections. The AR coating has been found to improve the beam quality of the SDLs, but it also reduces the confinement of the optical field within the RPG structure, and therefore the SDL gain [56].

2.4 The cavity and pump configuration

Light confined in any laser cavity comprises certain transverse and longitudinal modes that reproduce themselves after each round-trip [57]. The divergence, diameter and energy distribution of laser beams are determined by the transverse modes, while the spectral characteristics are determined by the longitudinal modes. This section focuses on the transverse modes that determine the beam quality of the laser. The longitudinal modes are covered in section 3.4.

The lowest order transverse mode is denoted TEM_{00} and has a Gaussian intensity distribution with an intensity maximum on the beam axis. It also has the smallest radius, the smallest divergence and the highest power density of the transverse cavity modes. The higher order transverse modes have intensity maxima outside the beam axis, and are denoted TEM_{mn} in Cartesian and TEM_{pl} in cylindrical coordinate systems. The beam radius and divergence increase with increasing mode number (n, m, p, l).

Lasers that have most of their energy in the TEM_{00}-mode are considered to have "good beam quality". The beam quality is often described with a beam quality parameter M^2. It describes how fast the laser beam diverges when compared to a diffraction-limited beam that has an M^2 value of one.

For SDLs, designing optical cavities that favour lower order transverse modes is usually simple and can be done analytically. The main requirements relate to the fundamental cavity mode size at the gain element and the cavity stability. The cavity mode at the gain element should be closely matched to the pump spot, because a smaller pump spot will introduce additional losses while a larger pump spot can excite higher order transverse modes. It is also beneficial to build stable laser cavities in order to minimize the effects of small external disturbances and misalignment on the laser operation. Schematics of typical I-, V- and Z-cavities are shown in Fig. 2.4.

In general, SDL cavities are simpler to design than solid state laser cavities [58], because the thinner SDL structures have smaller thermal gradients and shorter interaction lengths with the laser light. Consequently, the optical distortions caused by thermal lensing in the gain element are kept to a minimum, and the SDL cavities stay essentially

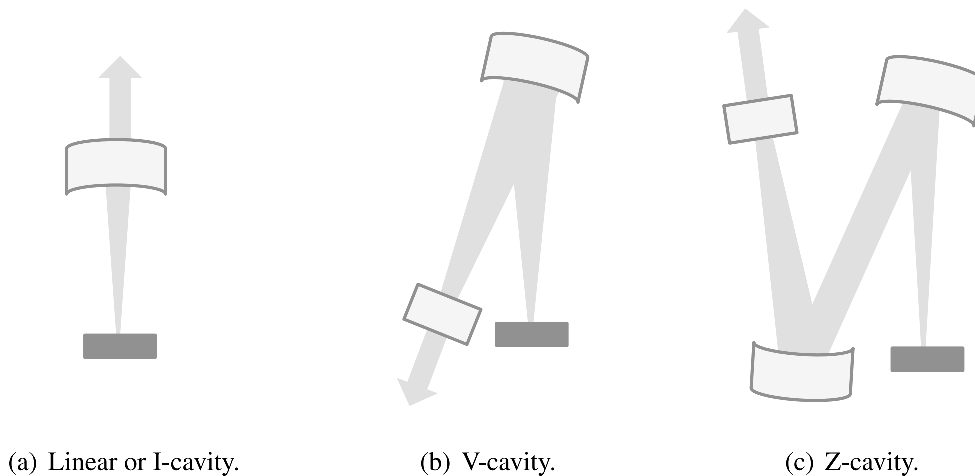

(a) Linear or I-cavity. (b) V-cavity. (c) Z-cavity.

Figure 2.4: External cavity schematics. The gain chip is shown by the dark bar and the cavity mirrors as light boxes.

unchanged over a large range of output power [44, 53, 59, 60].

Matching the pump spot to the fundamental cavity mode is also relatively simple in SDLs [45, 61, 62]. In particular, the requirements for the pump beam quality are very relaxed, because even a highly divergent pump beam can be matched with a low divergence SDL mode over a short distance of a few μm in the SDL gain section. Furthermore, it is relatively easy to produce a Gaussian intensity distribution over a distance of a few μm even with diode lasers that have very poor beam quality. Consequently, the spatial profile of the pump beam can be well-matched to the Gaussian fundamental cavity mode of the SDL, which is favourable for obtaining high beam quality [63, 64]. However, it should be noted that a uniform pump profile does introduce smaller temperature gradients and a lower peak temperature than a Gaussian pump profile [65]. Such uniform pump profiles are easily obtained from high power diode lasers [66] and have been used in SDLs with large pump areas [67, 68].

2.5 Wavelength coverage

The most impressive SDL performances have been obtained in the wavelength range 0.92-1.18 μm using GaAs-based structures with InGaAs QWs. These demonstrations include tens of watts of output power in single transverse mode operation and over 100 watts in multiple transverse mode operation [53, 68, 69]. Such performance is made

possible by the material properties of the GaAs-based structures emitting at ~ 1 μm. These properties include high material reliability and high thermal conductivity [70–72]. Furthermore, the DBRs can be fabricated using GaAs/AlAs layers that have a high refractive index contrast and therefore enable thin DBR structures with good optical properties.

SDLs operating in the 1.3–1.6 μm region are usually fabricated on InP substrates with InGaAsP QWs. However, these structures suffer from poor-performance DBRs. The reflective properties of the DBRs are degraded, because the materials lattice-matched to InP possess low refractive index contrast. This shortcoming limits the DBR bandwidth and essentially doubles the number of required layer pairs when compared with GaAs-based DBRs around 1 μm. Furthermore, the large number of DBR layer pairs and the increased $\lambda/4$ layer thickness lead to very thick DBR structures, which results in increased absorption losses and increased thermal resistances [73]. In addition, the materials lattice-matched to InP possess low thermal conductivity and the gain in InGaAsP QWs is sensitive to temperature [74,75]. Consequently, InP-based structures usually utilize intracavity diamond heat spreaders that circumvent the thermal impedance brought by the thick DBR [76].

SDLs emitting below 800 nm can be fabricated on GaAs substrates using various material combinations for the gain section [77, 78]. However, these structures also have their own challenges, such as low carrier confinement in the QWs which leads to increased temperature sensitivity, material degradation, AlGaAs/AlAs DBRs with reduced refractive index contrast and thermal conductivity, and the requirement for pump lasers emitting in the visible wavelength range [56,78–80]. Therefore, the performance of these devices has remained modest when compared with GaAs-based SDLs emitting around 1 μm.

Finally, SDLs have also been demonstrated at 800–900 nm using GaAs-based materials [81, 82], at 2–3 μm using GaSb-based materials [48], at 4–5 μm using materials grown on BaF_2 substrates [83, 84], and even at 440 nm using GaN-based materials [85]. However, these wavelength regions are beyond the scope of this thesis and are not covered further.

Chapter 3

Flip-chip semiconductor disk lasers with GaAs-based active regions

3.1 Introduction

Even though the intracavity diamond configuration requires less device processing and little consideration for the thermal conductivity of the DBR, the flip-chip configuration is preferred for several key SDL applications due to the drawbacks of intracavity diamonds. These drawbacks include beam distortion, spectral modulation [56], lower power scaling capabilities via increasing the pump spot size [86], intracavity losses [54, 87–92], birefringence [93] and higher cost. However, the flip-chip configuration does impose more demanding requirements for the bonding process. Namely, the bonding interface should provide reliable operation at elevated temperatures, provide high thermal conductance, and minimize the residual stress in the assembly.

3.1.1 Reliability

The reliability of a bonding interface relates to its deformation temperature. Soft solders such as In possess low melting temperatures and therefore exhibit low deformation resistance [94]. Better reliability can be obtained using Au-rich eutectic alloys such as AuSn, AuIn, AuSi and AuGe that have higher melting temperatures. The preferred alloys are AuSn and AuIn, because they provide relatively low bonding temperatures, high thermal conductivities and high strengths [95, 96]. Another option is to use metal-metal thermo-

compression bonding with Au, Al or Cu, which have much higher melting temperatures than the conventional solders and bonding alloys [97].

3.1.2 Thermal conductance

The thermal conductance of a bonding layer relates to its thermal conductivity and thickness. With conventional solders and eutectic alloys, the thickness of the bonding layer is in the range of a few micrometers [98, 99] and produces a non-negligible contribution to the thermal resistance of the structure. In addition, multiphase alloys possess inferior thermal conductivities when compared with the constituent metals, because their heterogeneous microstructure impedes the transfer of thermal energy [100, 101]. The thermal conductivity of the bonding layer can also decrease in time due to the formation of defects and voids [102–104].

3.1.3 Residual stress

The SDL gain elements tend to contract more than the CVD diamond heat spreaders during the cooling phase of the bonding process. Consequently, residual stress is introduced into the assembly, because the relative motion between the components is prevented by a rigid bonding layer. This stress increases with the bonding temperature, the size of the gain element, and the difference in the coefficients of thermal expansion (CTE). More detailed descriptions of these stress factors can be found in the literature [105].

The residual stress can be minimized by using heat sinks that are CTE-matched to the laser chip [106] or by using thick Au or In layers between the laser chip and the heat spreader [98, 107]. However, the former approach is limited by the low thermal conductivity of the CTE-matched heat spreaders, while the latter approach increases the thermal resistance of the structure by increasing the thickness of the bonding layer.

The residual stress can also be addressed by forcing the bonding layer to deform and therefore accommodate the CTE difference between the heat spreader and the SDL gain element. With solder alloys, this can be done by applying a relatively slow cooling rate of 2–3 °C/s, which is fast enough to prevent accelerated ageing and slow enough to allow stress relaxation [108–111]. The stress relaxation can be further enhanced by applying an annealing stage at least 50 °C below the melting temperature of the bonding interface [112–114]. However, such deformation can also degrade the bonding layer by

introducing accelerated ageing [115–119].

3.2 Low temperature Au-Au thermocompression bonding

This section presents a low temperature Au-Au bonding technique for integrating flip-chip SDLs onto CVD diamond heat spreaders [P1]. To date, Au-Au bonding has been demonstrated for VCSELs at 350 °C using thermocompression bonding [120], at 180 °C using thermosonic bonding [121, 122] and at 100 °C using surface activated bonding [123]. Au-Au bonding has also been demonstrated for edge-emitting lasers at 300 °C [124] and for various optical components at 100-150 °C [125, 126].

The Au-Au thermocompression bonding in this work was performed at a relatively low temperature of 150 °C to minimize the residual stress in the assembly. The bonding was also carried out using very thin Au layers in order to attain high thermal conductance in the bonding interface. Furthermore, the high melting temperature of Au is expected to provide a reliable bonding interface that can withstand high power operation and elevated temperatures. The performance of Au-Au bonded SDLs was evaluated by comparing them with SDLs that were bonded onto CTE-matched copper-diamond heat spreaders using $Au_{80}Sn_{20}$ and onto CVD diamond heat spreaders using In.

The thermal conductivities (k_{th}) of the 350 μm thick copper-diamond and CVD diamond heat spreaders were 500 W/mK and > 1800 W/mK, respectively. The $Au_{80}Sn_{20}$ and In bonded SDLs were metallized with 15 nm Ti - 100 nm Pt - 125 nm Au layers and the Au-Au bonded SDLs with 15 nm Ti - 125 nm Au layers using electron beam evaporation. For In bonding, the CVD diamond heat spreaders were metallized with 15 nm Ti - 100 nm Pt - 125 nm Au layers using electron beam evaporation and 7 μm of In using resistive heating. For Au-Au bonding, a monolayer of (3-Mercaptopropyl)trimethoxysilane (MPTMS) was deposited on the CVD diamond surface in low vacuum [127] before the deposition of 125 nm Au by electron beam evaporation.

The Au-Au thermocompression bonding was begun with an initial oxygen plasma treatment in order to remove organic contamination and render the Au surfaces active for bonding. The plasma treatment was immediately followed by oxide removal [128], which can be performed using ethanol or NH_4OH [129, 130]. After 20 min in ethanol, the SDL chips were pressed onto the CVD diamonds without drying, placed under uni-

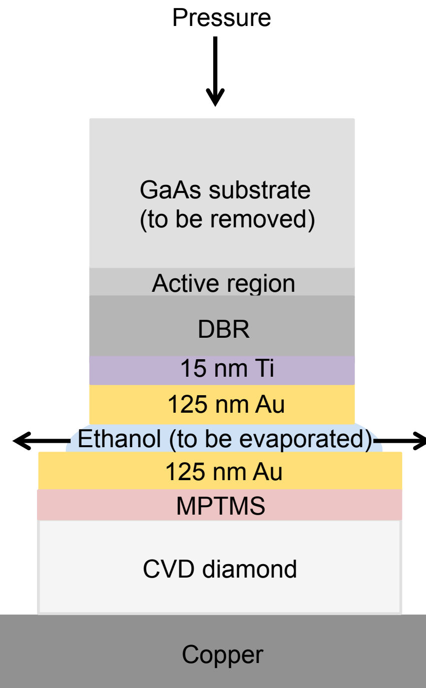

Figure 3.1: A schematic diagram of the Au-Au thermocompression bonding.

form pressure and annealed overnight at 150 °C. A schematic diagram of the process is illustrated in Fig. 3.1. The GaAs substrate was then removed by wet etching and the SDL-diamond assembly was bonded onto a water-cooled copper block.

The first gain structure was grown by solid source molecular beam epitaxy (MBE) and was designed to operate at 1050 nm. The gain section comprised 3 InGaAs quantum wells (QWs) that were placed at the antinodes of the optical field using GaInAsP spacer layers. The DBR comprised 28.5 pairs of GaAs/AlAs layers. All three chips were tested in a V-cavity with the gain element as an end mirror, a highly reflective curved folding mirror and a plane 2% output coupler (OC). The pump radiation from a fiber-coupled 808 nm diode laser was focused onto a spot with a diameter of 300 μm on the gain element. The cavity was designed to ensure good overlap between the pump spot and the fundamental cavity mode.

The output characteristics of the 3 QW SDLs are shown in Fig. 3.2. The output power reached 1.9 W with the CTE-matched copper-diamond heat spreader, 2.8 W with the In bonded chip and 4.2 W with the Au-Au bonded chip. The corresponding thermal resistances (R_{th}) are given in the legend of Fig. 3.2. The R_{th} values were derived from

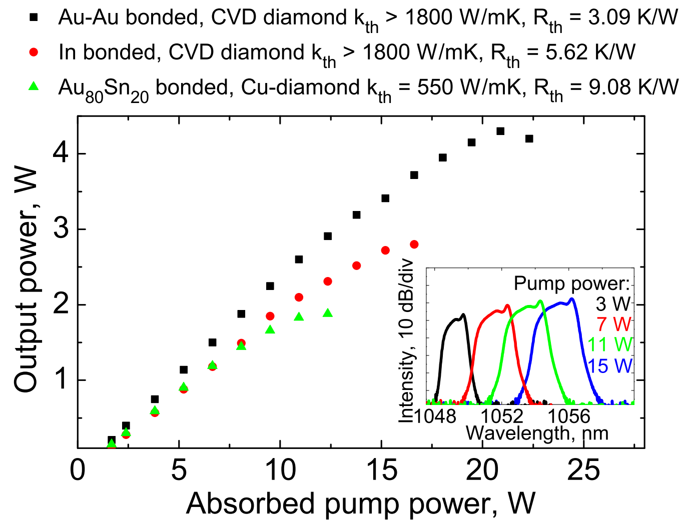

Figure 3.2: The output power as a function of pump power for $Au_{80}Sn_{20}$, In, and Au-Au bonded SDLs with 3 QWs. The optical spectra for the $Au_{80}Sn_{20}$ bonded SDL are shown in the inset.

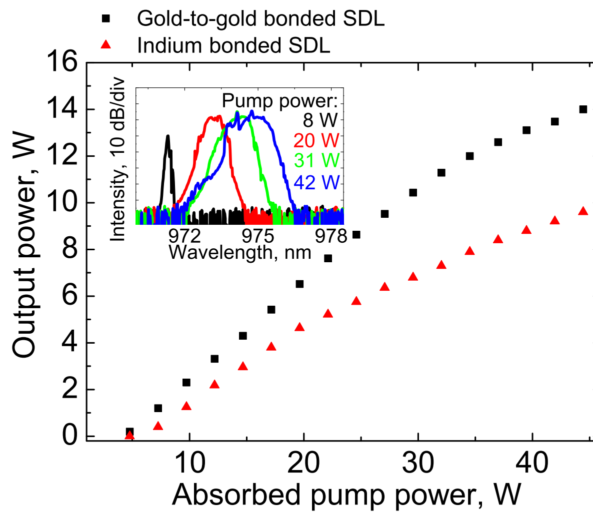

Figure 3.3: The output power as a function of pump power for In and Au-Au bonded SDLs with 10 QWs. The optical spectra for the Au-Au bonded SDL are shown in the inset.

the shift rates of the longest wavelength component in the emission spectra [131]. They were 9.08 K/W, 5.62 K/W and 3.09 K/W for the $Au_{80}Sn_{20}$, In, and Au-Au bonded chips, respectively.

The Au-Au and In bonding processes were also performed with a gain structure that was more suitable for high power operation. In this case, the MBE-grown structure comprised 10 InGaAs QWs that were placed at the antinodes of the optical field using GaAs spacer layers. The DBR comprised 23 pairs of GaAs/AlAs layers. The SDLs were tested in a V-cavity as before, but now the fundamental mode diameter on the gain element was 430 μm and the output coupling ratio 4%. The corresponding output powers as a function of pump power are shown in Fig. 3.3. In this case, the Au-Au bonded SDL produced a maximum output power of 14 W and the In bonded SDL 9.6 W at a pump power of 44 W. The beam quality parameter M^2 was measured to be below 1.4 in both cases at all pump powers.

3.3 Semiconductor-dielectric-metal compound mirrors

In addition to the thickness of the bonding layer, the performance of flip-chip SDLs also depends on the thermal and optical properties of the DBR. Reflectivities > 99.8 % are typically required at the laser wavelength and can be easily obtained with just a few pairs of silicon and dielectric layers. Such designs have been utilized in edge-emitting semiconductor lasers [132], VCSELs [133] and SDLs [134], but the thermal resistance of these materials limits their applicability [135]. Therefore, the DBRs in SDLs typically comprise 20-40 layer pairs of semiconductor materials with relatively high thermal conductivities. However, the optimal approach often relies on a combination of various materials, and depends on the SDL wavelength. This section provides an introduction to these different SDL mirror designs and presents SDLs with semiconductor-dielectric-metal compound mirrors.

3.3.1 Enhancing the DBR reflectivity

The thermal conductance of GaAs-based DBRs at $\sim 1\ \mu$m is relatively high, because they can be fabricated using thin GaAs/AlAs layers with high thermal conductivity and high refractive index contrast. However, the thermal resistance of the DBR increases with wavelength due to the increasing $\lambda/4$ layer thickness. Furthermore, the quantum defect tends to increase with wavelength, because GaAs-based structures are generally pumped with 808 nm diode modules and InP-based structures with 980 nm diode modules.

The increase in DBR thermal resistance can be alleviated by using a lower number of DBR layer pairs and by applying an Au layer to enhance the reflectivity of the DBR. In particular, using an Au layer as the last DBR layer, the number of layer pairs can be reduced from $\sim$ 25 to $\sim$18 with GaAs/AlAs DBRs while maintaining a reflectivity > 99.8 % [136]. In principle, such a configuration could enable an even lower number of DBR layers, but the Au layer also requires an absorbing Ti/Cr adhesion layer that reduces the reflectivity of the structure [137]. However, even if the Au layer could be deposited directly onto the semiconductor DBR, the Au atoms could diffuse into the semiconductor DBR at elevated temperatures [138].

An alternative approach is to place a thin dielectric layer between the semiconductor DBR and the highly reflective metal interface. This approach has been used in edge-emitting lasers with SiO_2-Ti-Au layers [139] and in semiconductor saturable absorber mirrors (SESAMs) with Al_2O_3-Ag [140] and SiO_2-Au layers [141, 142]. The dielectric layer allows thinner DBRs without compromising the reflectivity of the structure when compared with the conventional semiconductor-metal mirror design. Furthermore, the dielectric layer can provide high thermal conductance, provided it is thin enough.

However, care should be taken when combining semiconductors, dielectrics and highly reflecting metals. Specifically, the layers should provide a combination of high adhesion and limited diffusion between the materials. These conditions are fulfilled using Al_2O_3-Al layers due to the high stability of Al_2O_3 [138, 143]. Another option could be to use fluorine-based dielectrics with Au [144, 145]. Such an approach would allow a lower number of DBR layer pairs than the Al_2O_3-Al design, because Au has a higher reflectivity than Al.

3.3.2 SDLs with GaAs/AlAs-Al_2O_3-Al compound mirrors

This section presents MBE-grown flip-chip SDLs with GaAs/AlAs-Al_2O_3-Al compound mirrors [P2]. The active region comprised 13 InGaAs QWs that were placed at the antinodes of the optical field using GaInAsP spacer layers. The DBR comprised 28.5 pairs of GaAs/AlAs layers. The wafer was cut into pieces and different numbers of DBR layer pairs were removed by wet etching. The GaAs layers were removed using $C_6H_8O_7$:H_2O_2 (4:1) and the AlAs layers using H_3PO_4:H_2O_2:H_2O (3:1:50) [146]. After the wet etching, the set of SDL structures comprised gain elements with 11.5, 18.5 and 28.8 DBR layer pairs. The top-most GaAs surfaces were then treated with NH_3 plasma before de-

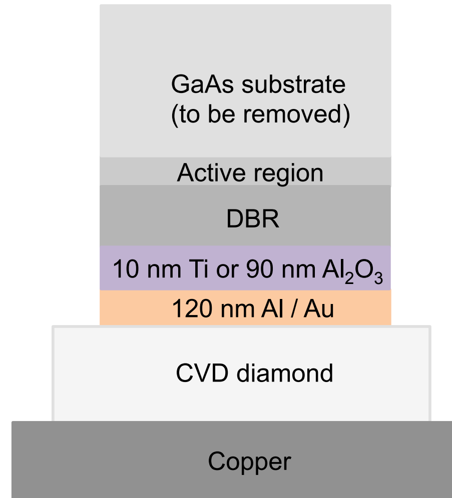

Figure 3.4: A schematic diagram of the SDLs structures with the GaAs/AlAs-Al_2O_3-Al and GaAs/AlAs-Ti-Al mirrors.

positing 90 nm of Al_2O_3 by atomic layer deposition (ALD) [147]. The structures were finished by depositing 120 nm Al by electron beam evaporation. Thermal management was achieved by bonding the 2 × 2 mm^2 gain chips onto CVD diamond heat spreaders with dimensions of 3 × 3 × 0.3 mm^3. A schematic diagram of the SDL structures is shown in Fig. 3.4.

As a reference for the thermal properties of the GaAs/AlAs-Al_2O_3-Al design, SDLs with 10 nm Ti - 120 nm Al metallization layers were also fabricated. The highly reflecting metal layer was chosen to be Al instead of Au, so that the only difference between the SDLs was the substitution of Al_2O_3 by Ti. The Ti-Al metallized SDLs were only tested with the full 28.8 DBR layer pairs, which provided a theoretical reflectivity > 99.98 % at the signal wavelength.

All the DBR configurations were also tested with a TiO_2-SiO_2 AR coating. The AR coating was designed to reduce the reflectivity of the top surface to below 0.3 % at the signal wavelength. The AR coating introduced more stringent requirements on the reflectivity of the compound mirror, because it reduced the gain enhancement in the active region.

Simulated reflectivity curves for the uncoated SDLs with the Al_2O_3-Al and the Ti-Au design are shown in Figs. 3.5(a) and 3.5(b), respectively. Figures 3.6(a) and 3.6(b) show the same reflectivity curves for the AR-coated SDLs. The reflectivity curves are summarized in Figs. 3.7(a) and 3.7(b), which highlight the differences between the two

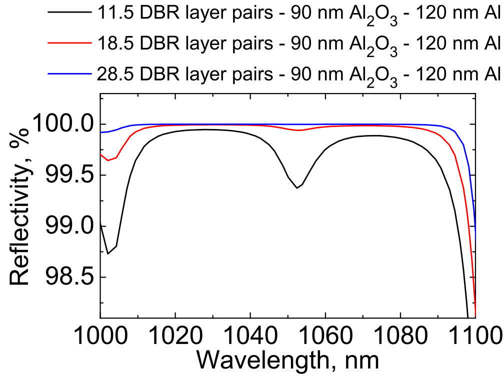

(a) Uncoated SDL structure with the semiconductor-Al_2O_3-Al mirror.

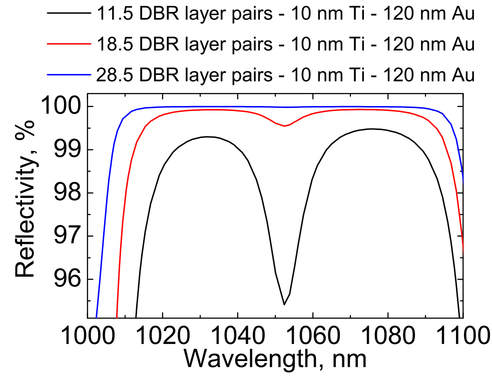

(b) Uncoated SDL structure with the semiconductor-Ti-Au mirror.

Figure 3.5: Simulated reflectivity for the uncoated SDL structure.

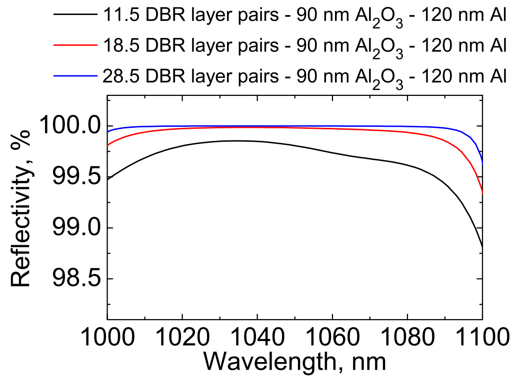

(a) AR-coated SDL structure with the semiconductor-Al_2O_3-Al mirror.

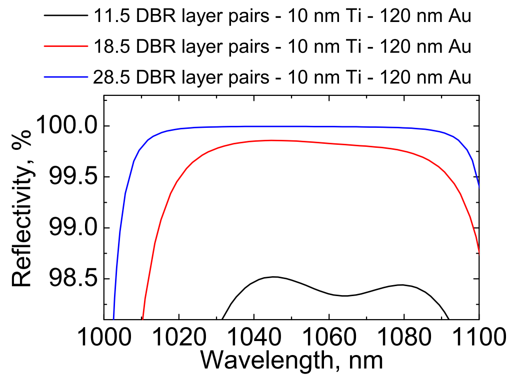

(b) AR-coated SDLs structure with the semiconductor-Ti-Au mirror.

Figure 3.6: Simulated reflectivity for the AR-coated SDL structure.

designs. For a reflectivity > 99.8 %, a minimum of 18.5 DBR pairs are needed with the conventional Ti-Au mirror design, whereas 11.5 DBR layer pairs is sufficient with the Al_2O_3-Al design.

The SDL gain elements were tested in a V-cavity that had the gain element as an end mirror, a highly reflective curved mirror and a plane output coupler. The optical pumping was performed with a fiber-coupled diode laser that was focused onto a spot with a 400 μm diameter on the gain elements. The output characteristics of the uncoated and the AR-coated SDLs are shown in Figs. 3.8 and 3.9, respectively. The output powers reached 16 W with the uncoated and 14 W with the AR-coated SDLs, regardless of the

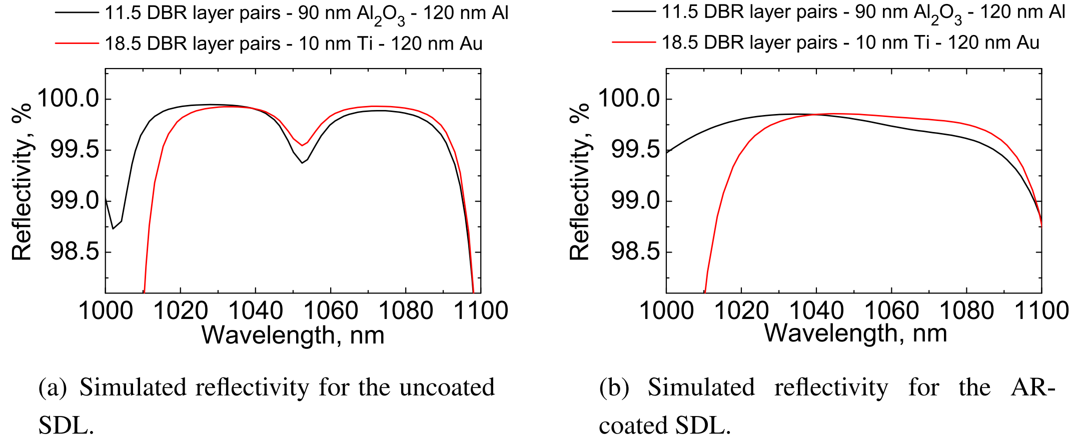

(a) Simulated reflectivity for the uncoated SDL.

(b) Simulated reflectivity for the AR-coated SDL.

Figure 3.7: Comparison of the semiconductor-Al_2O_3-Al mirror and semiconductor-Ti-Au mirror reflectivities.

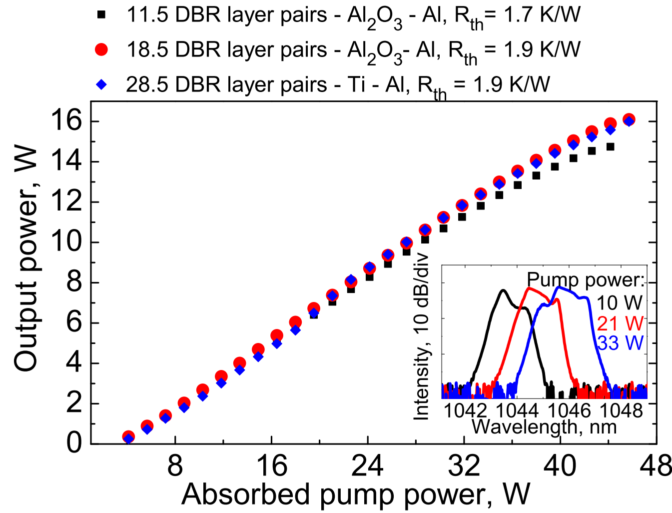

Figure 3.8: Output characteristics for the uncoated SDL structures with the semiconductor-Al_2O_3-Al mirror. The corresponding thermal resistances are given in the legend.

DBR thickness. The values for R_{th} were obtained as in section 3.2 and are shown in the legends of Figs. 3.8 and 3.9. Thermal roll-over was observed at slightly lower pump densities with the AR-coated SDLs than with the uncoated SDLs, as predicted in Ref. [35]. The beam quality parameter M^2 was measured to be below 1.3 for the uncoated chips and below 1.4 for the AR-coated chips at all pump powers.

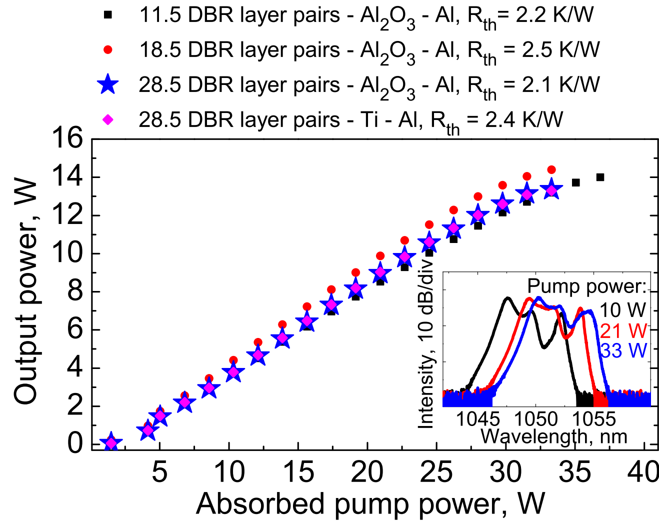

Figure 3.9: Output characteristics for the AR-coated SDL structures with the semiconductor-Al_2O_3-Al mirror. The corresponding thermal resistances are given in the legend.

In all cases, the optimal OC transmission was 5% for all the uncoated chips and 2.5 % for the AR-coated chips. This indicates that additional losses were not introduced into the cavity with the reduction in DBR thickness. Furthermore, the output power was the same with the full DBR for the Ti-Al and the Al_2O_3-Al designs, which indicates that the introduction of the thin Al_2O_3 layer didn't increase the thermal resistance of the SDLs.

The negligible effect of the number of DBR layer pairs on the output power and R_{th} was likely due to the high conductance of the relatively thin GaAs/AlAs DBR [148]. Nevertheless, reducing the number of DBR layer pairs can be beneficial for SDLs emitting at longer wavelengths, where the $\lambda/4$-thick DBR layers are thicker and the thermal resistance of the DBR is larger [136]. Furthermore, even at emission wavelengths close to 1 μm, thinner DBR sections can provide reduced misfit dislocation density [149], shorter growth times, less material use and lower cost.

3.4 Single-frequency operation

In addition to their power scalability and high beam quality, SDLs have been considered very suitable for single-frequency operation. This feature originates from the high-Q external cavity and the properties of the SDL gain element. This section provides an introduction to these properties and presents a single-frequency SDL with 4.6 W of output power.

3.4.1 Longitudinal modes in SDLs

The longitudinal modes of SDLs are determined by the resonant frequencies of the external cavity and the bandwidth of the gain element, $\Delta\nu_{\mathrm{gain}}$. The separation $\Delta\nu_{\mathrm{FSR}}$ of the cavity resonance frequencies, i.e. the free spectral range (FSR) of the cavity, is given by [150]

$$\Delta\nu_{\mathrm{FSR}} = \frac{c}{2L_{\mathrm{cav}}} = \frac{1}{T_{\mathrm{rt}}}, \tag{3.1}$$

where c, L_{cav} and T_{rt} are the the velocity of light, the optical cavity length and the cavity round-trip time, respectively.

The finesse for an optical cavity with low losses α_{loss} is related to the free spectral range and given by

$$\mathcal{F} = \frac{\Delta\nu_{\mathrm{FSR}}}{\Delta\nu_{\mathrm{c}}} \approx \frac{2\pi}{\alpha_{\mathrm{loss}}}, \tag{3.2}$$

where $\Delta\nu_{\mathrm{c}}$ is the linewidth of a longitudinal cavity mode and α_{loss} the total optical losses in the cavity. Another essential parameter is the Q factor, which is defined as

$$Q = 2\pi\frac{\text{energy stored in the laser cavity}}{\text{energy lost in one oscillation cycle}} = 2\pi\nu\frac{T_{\mathrm{rt}}}{\alpha_{\mathrm{loss}}} = 2\pi\nu\tau_{\mathrm{ph}} = \frac{\nu}{\Delta\nu_{\mathrm{c}}}, \tag{3.3}$$

where ν and τ_{ph} are the optical frequency and the photon lifetime in the cavity, respectively. Therefore, the cavity linewidth $\Delta\nu_{\mathrm{c}}$ can now be expressed as

$$\Delta\nu_{\mathrm{c}} = \frac{1}{2\pi}\frac{\alpha_{\mathrm{loss}}}{T_{\mathrm{rt}}} = \frac{1}{T_{\mathrm{rt}}\mathcal{F}} = \frac{1}{2\pi\tau_{\mathrm{ph}}} \tag{3.4}$$

and the photon lifetime as

$$\tau_{\mathrm{ph}} = \frac{T_{\mathrm{rt}}}{\alpha_{\mathrm{loss}}} = \frac{1}{c\pi}\mathcal{F}L_{\mathrm{cav}}. \tag{3.5}$$

Consequently, narrow linewidth operation and long photon lifetimes can be obtained in long high-finesse cavities, which are characteristic of SDLs [5, 151].

3.4.2 Properties of single-frequency SDLs

The spectral width of any laser has a fundamental lower limit, because spontaneous emission and cavity losses introduce fluctuations into the phase of the optical field within the laser cavity. Lasers operating at this fundamental quantum limit exhibit frequency-independent white noise, a Lorentzian emission spectrum and a linewidth (FWHM) given by the Schawlow-Townes equation [152, 153]. However, additional noise is added in semiconductor lasers due to intensity-phase coupling, because both the gain and the refractive index depend on the carrier density [154].

For SDLs, the fundamental limit for the linewidth is given by the modified Shawlow-Townes equation [155, 156]

$$\Delta\nu_{\mathrm{laser}} = \frac{2\pi h\nu}{P_{\mathrm{out}}} (\Delta\nu_{\mathrm{c}})^2 n_{\mathrm{sp}} \left(1+\alpha^2\right) = \frac{h\nu}{2\pi P_{\mathrm{out}}} \left(\frac{\alpha_{\mathrm{loss}} c}{2L_{\mathrm{cav}}}\right)^2 n_{\mathrm{sp}} \left(1+\alpha^2\right), \tag{3.6}$$

where n_{sp} is the spontaneous emission factor ($n_{\mathrm{sp}} \sim$ 1-3) and α the linewidth enhancement factor ($\alpha \sim$ 2-3) that takes into account the intensity-phase coupling in semiconductor lasers. In SDLs, this limit is on the sub-Hz level, and very difficult to reach due to technical noise [155,156]. This noise includes acoustic noise, mechanical vibrations and temperature fluctuations caused by the (multimode) pump laser [157–160]. The consequent cavity length fluctuations then translate into frequency fluctuations in the output beam. Furthermore, the frequency fluctuations can also translate into intensity fluctuations if wavelength selective elements are placed into the cavity, because the wavelength selective elements modulate the intracavity losses depending on the wavelength.

Nevertheless, when compared with other types of lasers [4, 5, 161, 162], SDLs can provide very narrow linewidths, low noise, high side-mode suppression ratios and low sensitivity to optical feedback due to the negligible amount of amplified spontaneous emission (ASE). In particular, in SDLs [5, 156, 160, 163, 164]

- spontaneous emission is filtered by the external cavity for the emitted mode due to a very narrow cavity linewidth $\Delta\nu_{\mathrm{c}}$ (or high-Q cavity, or long photon lifetime τ_{ph}, or long high-finesse cavity),
- spontaneous emission easily leaks out from the long air-filled external cavity,
- the RPG structure provides spatially and spectrally homogeneous gain without nonlinear mode interactions, and
- the RPG structure confines the excited carriers to the antinodes of the optical field,

where they are efficiently extracted by the laser and not lost to spontaneous emission.

An essential parameter for single-frequency SDLs is the characteristic time. It is the time that is required for a homogeneously broadened laser to collapse into single-frequency operation after a strong perturbation, e.g. 100 % pump fluctuation. The characteristic time is given by [156, 165, 166]

$$\tau_{char} = \frac{8\ln(2)}{\pi^2 c^3}\frac{\Gamma_g^2 L_{\mathrm{cav}}^3}{\alpha_{\mathrm{loss}}}, \tag{3.7}$$

where Γ_g is the gain or filter bandwidth. Single-frequency operation is obtained if the characteristic time of the laser is shorter than the thermal, mechanical or pump fluctuation time [48]. This can be achieved by using short cavities of 5–30 mm or by introducing wavelength selective elements into the cavity. To date, these configurations have been utilized to demonstrate single-frequency SDLs at wavelengths spanning from the ultraviolet to 2.8 μm [167–169] and with output powers up to 23 W [157]. Such a combination of high output power and narrow linewidth makes single-frequency SDLs particularly suitable for applications such as light detection and ranging (LIDAR), free space communications and high resolution spectroscopy [161, 170, 171].

3.4.3 Single-frequency SDL emitting at 1.05 μm

This section presents the results that were obtained with a flip-chip single-frequency SDL emitting at 1.05 μm [P3]. The SDL structure was grown by MBE on GaAs substrate. The gain section comprised 10 InGaAs QWs that were placed at the antinodes of the optical field using GaInAsP spacer layers. The DBR comprised 28.5 pairs of GaAs/AlAs layers.

Thermal management was achieved by bonding the 2 $\times$ 2 mm^2 gain chip onto a CVD diamond with dimensions of 3 $\times$ 3 $\times$ 0.3 mm^3. The substrate was removed by wet etching and the assembly was bonded onto a copper block using indium. The copper block was cooled using a Peltier element without water circulation to avoid mechanical vibrations. The SDL was also placed inside a styrofoam box to protect it from noise originating from the environment.

The optical pumping was performed with a fiber-coupled diode laser that was focused onto a spot with a diameter of 400 μm on the gain element. The $\sim$ 128 mm long V-cavity

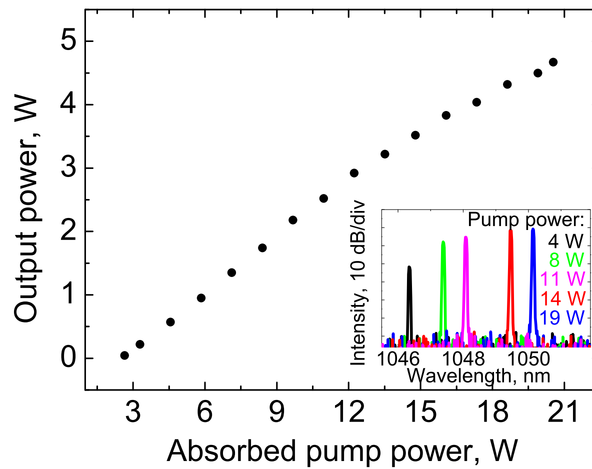

Figure 3.10: Output characteristics of the SDL in single-frequency operation. The optical spectra at various pump powers are shown in the inset.

had the gain element as an end mirror, a curved highly reflective folding mirror and a plane 3% output coupler. Single-frequency operation was obtained by placing a 1-mm thick UV-grade fused silica etalon into the laser cavity.

The output characteristics of the single-frequency SDL are shown in Fig. 3.10. The output power reached 4.6 W at a pump power of 21 W. The optical spectra at various pump powers are shown in the inset. Single-frequency operation was confirmed with a scanning Fabry–Pérot interferometer (FPI) with a free spectral range of 1.5 GHz. The FPI spectrum is shown in Fig. 3.11 with a close-up of the resolution-limited 15 MHz (FWHM) peak shown in the inset.

The linewidth of the SDL was further characterized using delayed self-heterodyne interferometer (DSHI) measurements, where the laser output is divided into two beams [172, 173]. One beam is propagated through a long optical fiber that provides a time delay, and the other beam is propagated through an acousto-optic modulator (AOM) that provides an optical frequency shift. The beams are then combined and the linewidth is calculated from the corresponding radio frequency (RF) beat note that is centered at the AOM frequency. An illustration of the measurement setup is shown in Fig. 3.12

However, accurate DSHI measurements typically require very long fiber delay lines, because the delay line needs to be $\sim$ 6 times longer than the coherence length of the

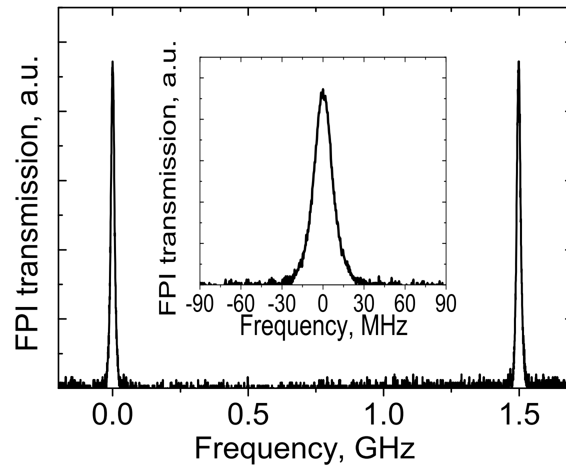

Figure 3.11: Scanning Fabry–Pérot interferometer spectrum taken at a pump power of 16 W. A close-up of the 15 MHz (FWHM) interferometer peak is shown in the inset.

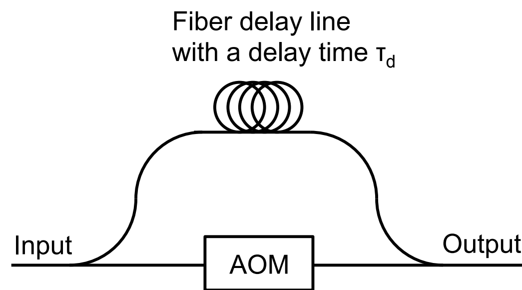

Figure 3.12: A schematic of the delayed self-heterodyne measurement setup.

laser [174, 175]. This makes direct linewidth measurements using DSHI somewhat impractical, especially for measuring very narrow linewidths in the kHz range. Consequently, the SDL linewidth was estimated using a delay line that was below the coherence length of the laser. Such characterisation provides a rougher estimate for the laser linewidth, but it also allows substantially shorter fiber delay lines.

When the delay line in DSHI is shorter than the coherence length of the laser, the two beams stay partially correlated and the DSHI spectrum comprises an oscillating pattern with a period corresponding to the inverse of the delay time [176, 177]. The measured DSHI spectrum is shown in Fig. 3.13. It is centered at 150 MHz, which corresponds to

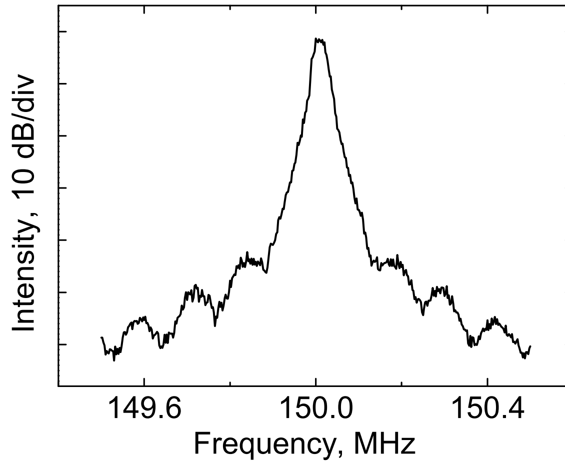

Figure 3.13: Delayed self-heterodyne interferometer RF signal taken at a pump power of 16 W.

the frequency shift of the fiber-coupled AOM. The 120 kHz oscillations indicate that the coherence length of the SDL is considerably longer than the 1.7 km fiber delay. Now, the measured lower limit for the SDL coherence length allows the upper limit for the laser linewidth to be estimated from [178]

$$\Delta\nu_{\mathrm{G}} = \sqrt{\frac{2\ln(2)}{\pi}} \frac{c}{L_{\mathrm{coh,\,G}}} \tag{3.8}$$

for a Gaussian spectral distribution and from

$$\Delta\nu_{\mathrm{L}} = \frac{c}{\pi L_{\mathrm{coh,\,L}}} \tag{3.9}$$

for a Lorenzian spectral distribution. The corresponding linewidth values in this case are 78 kHz and 38 kHz for Gaussian and Lorentzian spectral distributions, respectively. However, it should be noted that the actual laser linewidth is expected to have a Gaussian spectral distribution [159, 170].

Chapter 4

Semiconductor disk lasers with InP-based active regions

4.1 Introduction

As already covered in section 2.5, InP-based materials are suitable for emitting in the wavelength range 1.2–1.7 μm, but appropriate compound materials for the DBR section are not available. On the other hand, GaAs-based structures can provide DBRs with very good optical and thermal properties, but they suffer from low gain at wavelengths above 1.3 μm [179]. Furthermore, since metamorphic growth [180] and dielectric DBRs [134] have provided only limited performance with InP-based active regions, the optimal solution seems to reside in combining the properties of InP-based active regions with GaAs-based DBRs. This type of integration was initially demonstrated using a process called wafer fusion for optically pumped VCSELs [181, 182], but it was later also extended to SDLs [183, 184].

This chapter provides an introduction to wafer bonding of Si-based materials, wafer fusion of III-V semiconductors, and wafer bonding of III-V semiconductors with intermediate Si-based layers. The discussion is followed by a presentation of three different bonding methods that were used to obtain multi-watt output powers from SDLs emitting at 1.3 μm and 1.6 μm. The experimental results also include single-frequency operation at 1.56 μm with 1 W of output power.

4.2 Wafer bonding

In essence, wafer bonding provides a route for integrating materials that cannot be grown monolithically without introducing excessive amounts of defects. It has been widely utilized in silicon-on-insulator (SOI) technology, which is used in the fabrication of integrated circuits (ICs), micro-electro-mechanical systems (MEMS) and silicon photonics [185–188]. Wafer bonding has also been utilized in photonic integrated circuits (PICs) for integrating III-V optoelectronics onto Si wafers [188–191], because these materials possess mismatched lattice constants and CTEs that hinder high-quality monolithic growth [192]. In addition, wafer bonding has been utilized in III-V optoelectronic devices such as photodetectors, edge-emitting semiconductor lasers and solar cells [193–195].

4.2.1 Direct bonding with Si-based materials

The bonding techniques for Si-based wafers are conventionally divided into hydrophilic and hydrophobic bonding. In hydrophilic bonding, the Si wafers are covered with an oxide layer that is terminated by OH or NH_2 groups. The wafer surfaces are also covered with a few monolayers of polar H_2O molecules that provide room temperature adhesion via van der Waals forces upon joining the wafers. When the wafer stack is annealed above 150 °C, the H_2O molecules diffuse away from the bonding interface or react with the surrounding material. In the case of Si wafers, hydrophilic bonding takes place via the following reactions [196, 197]

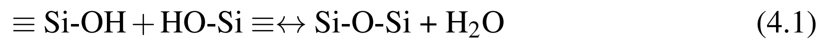

$$\equiv \text{Si-OH} + \text{HO-Si} \equiv \leftrightarrow \text{Si-O-Si} + \text{H}_2\text{O} \tag{4.1}$$

$$\equiv \text{Si-NH}_2 + \text{NH}_2\text{-Si} \equiv \leftrightarrow \equiv \text{Si-N-N-Si} \equiv +2\text{H}_2. \tag{4.2}$$

In hydrophobic bonding, the surface oxides are removed using HF and the wafer surfaces are terminated with H and/or F atoms [198, 199]. In this case, room temperature adhesion is provided by polar HF molecules [200]. When the wafer stack is annealed at several hundreds of degrees, the H and F atoms desorb from the wafer surfaces and diffuse away from the bonding interface. In the case of Si wafers, hydrophobic bonding takes place via the reaction [198]

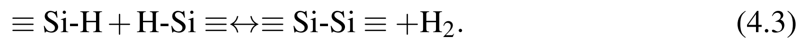

$$\equiv \text{Si-H} + \text{H-Si} \equiv \leftrightarrow \equiv \text{Si-Si} \equiv +\text{H}_2. \tag{4.3}$$

4.2.2 Direct bonding with III-V materials

While both hydrophilic and hydrophobic bonding are routinely used with Si-based wafers, direct bonding of III-V wafers is conventionally performed using hydrophobic bonding. This process is also called wafer fusion [201] or bonding by atomic rearrangement [202]. The description of the wafer fusion process given here follows the one given in Refs. [194, 203, 204].

The wafer fusion process comprises surface preparation, wafer contacting and annealing at elevated temperatures (> 500 °C). The surface preparation usually includes patterning in order to generate outgassing channels for the gasses that are released from III-V surfaces during high temperature annealing. Organic contaminants are then removed from the wafer surfaces using oxygen plasma or UV-ozone treatments. The consequent oxide layers are removed using appropriate chemicals such as HF for InP and HCl for GaAs, but the oxide removal can also be done in an environment with reduced oxygen partial pressure. Finally, the wafers are contacted with uniform pressure of 3 kPa – 3 MPa and the temperature of the assembly is increased to > 500 °C for about 30 min. In the case of bonding InP and GaAs, phosphorus (P) and indium (In) are said to be the mobile species that provide uniform contacting via atomic diffusion.

The wafer fusion processes in this thesis were performed at École Polytechnique Fédérale de Lausanne in Switzerland. The process was initially developed for fabricating VCSELs with GaAs-based DBRs and InP-based active regions [205, 206]. In this process, the GaAs and InP wafers are contacted at 600 °C in a vacuum or purified nitrogen environment. Upon annealing and applying uniform pressure, the wafers undergo slight plastic deformation that allows uniform contacting on a wafer scale. When the assembly is cooled to room temperature, the wafer stack bows with a radius of curvature of about 1 m due to mismatched CTEs between GaAs and InP. However, the planarity of the stack is restored once one of the substrates is removed [207].

4.2.3 Bonding of III-V materials with intermediate Si-based layers

In many cases, the temperature of the wafer bonding process is kept as low as possible to prevent residual stress [208–210]. With Si-based materials, low temperature bonding is usually performed using hydrophilic bonding. However, hydrophilic bonding with III-V materials is not straightforward, because the characteristics of the surface oxides are less known and the surface cleaning procedures less developed in comparison to Si-based

materials. In particular, the oxides of GaAs are unstable and the surfaces are prone to roughening upon wet chemical cleaning [211]. Furthermore, III-V materials react with water at elevated temperatures and form gaseous side products, which can lead to large interface bubbles [208, 212, 213].

A common method for low temperature bonding of III-V materials is to use thin intermediate layers. The intermediate layers are usually Si-based dielectric layers [214, 215], metal layers [97], adhesive layers [216] or ultra thin polymer layers [217–219]. As compared to direct hydrophobic III-V wafer bonding, this approach allows the use of well-developed bonding procedures and provides less sensitivity to surface microroughness [220].

The most common intermediate layer bonding method utilizes dielectric layers on both III-V semiconductor surfaces. The surface activation is often done with plasma [220, 221], but it can also be done chemically [196] or with UV light [222]. Another particularly attractive method is the utilization of self-assembling monolayers. In this case, a molecule with at least two different functional groups is deposited on the wafer surface. The first functional group is used to attach the molecule to the first wafer, while the second functional group is used to obtain bonding to the opposing wafer.

4.3 SDLs in the 1.3 μm wavelength band

High power operation in GaAs-based SDLs is hindered at wavelengths above 1.18 μm due to increased lattice mismatch between the InGaAs QWs and GaAs [223, 224]. The procedures for extending the emission wavelength beyond 1.18 μm include introducing small amounts of nitrogen into the InGaAs QWs [225] and embedding InAs quantum dots (QDs) into the InGaAs QWs [226, 227]. The dilute nitride structures preferably contain a high indium content for minimizing the amount of required nitrogen [228], while the QD structures should be fabricated with one QD layer per antinode [229]. These schemes have provided maximum output powers of 4.7 W at 1.25 μm using InAs QDs [230] and 0.6 W at 1.32 μm using dilute nitride QWs [231]. However, the operation of QD structures is unclear at 1.3 μm [232] and the dilute nitride structures suffer from increased non-radiative processes with increasing wavelength [233]. Consequently, the optimal solution for SDLs emitting at 1.3 μm seems to be the integration of GaAs-based DBRs and InP-based active regions. The first demonstration of such an SDL produced 2.7 W of output power in the intracavity diamond configuration [183].

4.3.1 Wafer-fused SDLs emitting at 1.27–1.31 μm

This section presents the results that were obtained with wafer-fused SDLs in the intracavity diamond and the flip-chip configuration [P4, P7]. Both structures were processed at École Polytechnique Fédérale de Lausanne in Switzerland using the wafer fusion process described in section 4.2.2. The SDLs were pumped at 980 nm using a fiber-coupled diode laser and characterised in V-cavities with a curved folding mirror and a plane 2.5 % output coupler. The fundamental cavity mode was designed to match the pumped spot and the temperature of the gain element was set to 7 °C in all cases.

In the intracavity diamond configuration, the InP-based gain section was grown by metallorganic vapor phase epitaxy (MOVPE) and comprised 10 compressively strained AlGaInAs QWs. The QWs were placed at five antinodes of the optical field with a distribution of 2-2-2-2-2 using lattice-matched AlGaInAs spacer layers and an InP window layer. The photoluminescence (PL) peak of the QWs was centered at 1263 nm at room temperature. The DBR was grown by MBE on GaAs substrate and comprised 35 $Al_{0.9}Ga_{0.1}As$/GaAs layer pairs.

After the wafer fusion process, the InP substrate was removed by wet etching and the structure was cut into chips of 2.5 $\times$ 2.5 mm^2. The CVD intracavity diamond heat spreader had dimensions of 3 $\times$ 3 $\times$ 0.3 mm^3 and a 2° wedge to avoid the etalon effect. The top surface of the diamond was AR-coated for the pump and signal wavelengths with TiO_2-SiO_2 layers. The pump spot diameter at the gain element was set to 300 μm. The output characteristics are shown in Fig. 4.1 with a maximum output power of 6.6 W. However, the output power was later increased to 7.1 W using a similar configuration [234].

The SDL in the flip-chip configuration had a similar structure, but now the AlGaInAs QWs were placed at four antinodes of the optical field with a distribution of 3-3-2-2. In addition, a λ-thick defect blocking layer was placed below the gain section at the fusion interface [235]. The PL peak of the QWs was centered at 1255 nm at room temperature. The DBR was grown by MBE on GaAs substrate and comprised 24 GaAs/AlAs layer pairs.

After the fusion process, the GaAs substrate was removed by wet etching and Ti-Au layers were deposited onto the bottom of the DBR. The structure was then cut into pieces of 3 $\times$ 3 mm^2 and a chip was Au-Au bonded onto a 5 $\times$ 5 $\times$ 0.3 mm^3 CVD diamond heat spreader. Finally, the InP substrate was removed by wet etching and the gain assembly

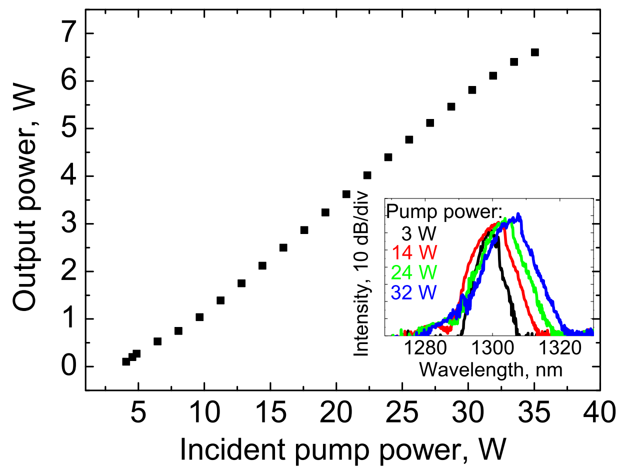

Figure 4.1: Output characteristics of the wafer-fused SDL with intracavity diamond configuration. The optical spectra are shown in the inset at various pump powers.

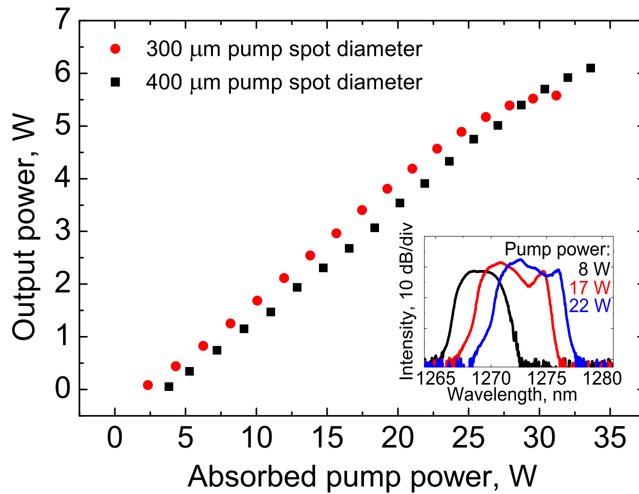

Figure 4.2: Output characteristics of the wafer-fused SDL with flip-chip configuration. The optical spectra are shown in the inset at various pump powers with a pump spot diameter of 300 μm.

was bonded onto a water-cooled copper block using In.

The output characteristics of the flip-chip SDL are shown in Fig. 4.2. The maximum output powers reached 5.6 W and 6.1 W with pump spot diameters of 300 μm and

400 μm, respectively. The beam quality parameter M^2 was measured to be below 1.25 at all pump powers. The limited increase in output power with increasing pump area was due to not having a good enough spot on the gain element with a 400 μm diameter. Nevertheless, even the relatively small pump spot of 300 μm enabled output powers that were comparable to those obtained in the intracavity diamond configuration.

4.3.2 Wafer-bonded SDLs emitting at 1.32 μm

This section presents the results for wafer-bonded SDL structures with two different intermediate layer bonding processes [P5]. In the first method, the DBR and the active region were bonded using thin hydrophilic SiO_2 layers on both surfaces. In the second method, the bonding was carried out utilizing a self-assembling monolayer of (3-Mercaptopropyl)trimethoxysilane (MPTMS).

The InP-based active region was grown by MBE and comprised 10 compressively strained AlGaInAs QWs. The QWs were placed at four antinodes of the optical field with a distribution of 3-3-2-2 using lattice-matched AlGaInAs spacer layers and an InP window layer. The PL peak of the QWs was centered at 1277 nm at room temperature. The DBR was grown by MBE on GaAs substrate and comprised 25.5 GaAs/AlAs layer pairs.

In the first bonding process, the SiO_2-covered active region and the SiO_2-covered DBR were dipped into NH_4OH to render them hydrophilic with NH_2 and OH groups [196, 215]. After drying with nitrogen, the wafers were bonded at room temperature via van der Waals forces by placing them face-to-face and pressing the assembly in the middle.

In the second bonding process, the SiO_2-covered DBR structure was dipped into NH_4OH, dried with nitrogen and placed in a low-vacuum chamber with an open container of MPTMS. This allowed the hydrophilic silanol groups $Si(OCH_3)_3$ of the MPTMS vapour to react with the hydrophilic NH_2 and OH groups on the DBR surface [127]. Consequently, the DBR surface became covered with hydrophobic SH groups that were located at the other end of the MPTMS molecules and could bond with a hydrophobic InP surface [236]. The InP-based active region was then dipped into 0.5% HF, dried with nitrogen, placed on the SH-terminated DBR, and bonded via van der Waals forces at room temperature.

In both bonding processes, covalent bonding was achieved by applying a uniform

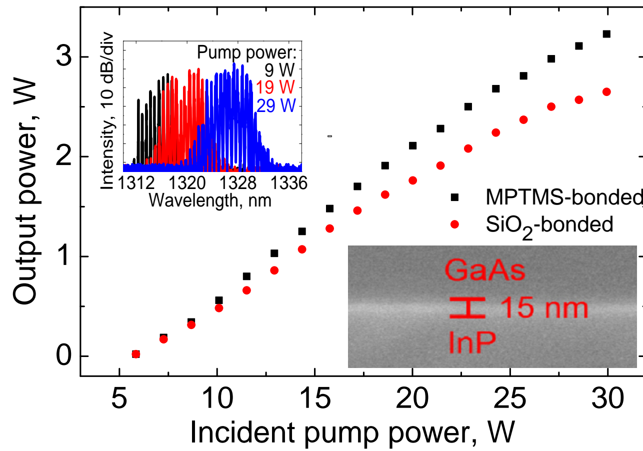

Figure 4.3: Output characteristics of the wafer-bonded SDLs. The optical spectra at various pump powers for the MPTMS-bonded SDL is shown in the inset. The multiline spectra originate from the Fabry–Pérot etalon effect induced by the intracavity diamond heat spreader. A scanning electron micrograph of the MPTMS-bonding interface is also shown in the inset.

pressure of 0.5 MPa and annealing the assemblies overnight at 200 °C. The InP substrate was then removed by wet etching and the 8×8 mm^2 wafers were cut into pieces of 2×2 mm^2. Thermal management was achieved by capillary bonding 530 μm thick CVD intracavity diamond heat spreaders onto the gain elements. The top surfaces of the intracavity diamonds were AR-coated for the pump and signal wavelengths with TiO_2-SiO_2 layers. The optical pumping was performed with a 980 nm fiber-coupled diode laser and the pump spot diameter was set to 300 μm. The fundamental cavity mode of the V-cavity was designed to match the pumped spot. The temperature of the gain elements was set to 15 °C.

The SDL output characteristics for both bonding processes are shown in Fig. 4.3. The maximum output powers were 2.65 W and 3.23 W with the SiO_2- and the MPTMS-bonded SDL, respectively. The corresponding beam quality parameters M^2 were measured to be below 1.7 and 1.8 at all pump powers. However, it was later observed that the output power and the beam quality were limited by the poor quality of the intracavity diamond in both cases. A higher output power of ~ 4 W was later reported from this

same batch using a smaller pump spot with a diameter of 200 μm [237] .

4.4 SDLs in the 1.5 μm wavelength band

The first SDL demonstrations at wavelengths around 1.55 μm included a flip-chip structure with a dielectric DBR [134] and a monolithic InP-based structure with a thinned substrate [238]. However, the output powers were limited to some tens of mW due to the high thermal resistances of the DBRs. The output power was later scaled up using intracavity diamond heat spreaders. These results include 100 mW at 20 °C with a monolithic InP-based structure [239] and 2.6 W at 10 °C with a wafer-fused SDL having a GaAs-based DBR [184].

There have also been several reports of single-frequency SDL operation at 1.55 μm. The most notable results include 77 mW in the flip-chip configuration with a metamorphically grown GaAs-based DBR [180] and 170 mW in the intracavity diamond configuration with a monolithic InP-based structure [168]. Both results were obtained at a gain element temperature of 20 °C. Such light sources could find use for example in optical links [240].

4.4.1 Wafer-fused SDL emitting at 1.58 μm

This section presents the results that were obtained with a wafer-fused SDL emitting at 1.58 μm [P8]. The InP-based gain section was grown by MOVPE and comprised 10 compressively strained AlGaInAs QWs. The QWs were positioned at five antinodes of the optical field with a distribution of 2-2-2-2-2 using AlGaInAs spacer layers and an InP window layer. The PL peak of the QWs was centered at 1520 nm at room temperature. The DBR was grown by MBE on GaAs substrate and comprised 35 $Al_{0.9}Ga_{0.1}As$/GaAs layers pairs.

After the wafer fusion process, the InP substrate was removed by wet-etching and the structure was cut into chips of 2.5 $\times$ 2.5 mm^2. Thermal management was performed using an CVD intracavity diamond heat spreader with dimensions of 3 $\times$ 3 $\times$ 0.3 mm^3. The top surface of the diamond was AR-coated for the pump and signal wavelengths with TiO_2-SiO_2 layers.

The SDL was tested in a V-cavity with a curved folding mirror and a plane 1.5 % output coupler (OC). The optical pumping was performed with a 980 nm fiber-coupled

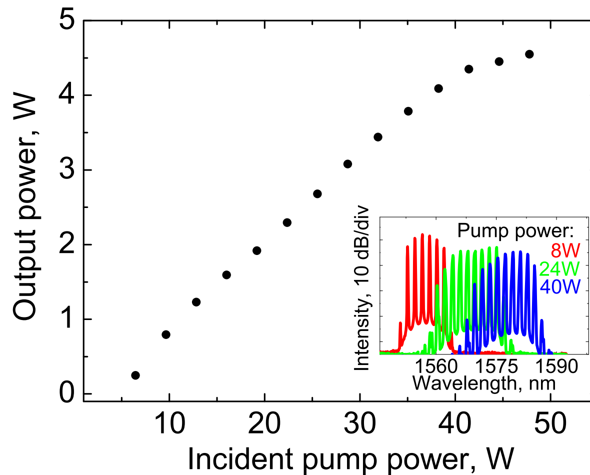

Figure 4.4: Output characteristics of the 1.58 μm SDL. The optical spectra are shown in the inset at various pump powers. The multiline spectra originate from the Fabry–Pérot etalon effect induced by the intracavity diamond heat spreader.

diode laser that was focused onto a spot with a 300 μm diameter on the gain element. The fundamental mode of the V-cavity was designed to match the pump spot and the temperature of the gain element was set to 8 °C. The output characteristics are shown in Fig. 4.4 with a maximum output power of 4.6 W. The beam quality parameter M^2 was measured to be below 1.25 at all pump powers.

4.4.2 Single-frequency wafer-fused SDL emitting at 1.56 μm

The gain element presented in the previous section was also utilized for single-frequency operation [P6]. The external cavity was a V-cavity as before, but now two UV-grade fused silica etalons with thicknesses of 1 mm and 0.75 mm were inserted into the cavity to obtain single-frequency operation. The temperature of the gain element was kept at 15 °C. It was controlled using a Peltier element without water circulation to avoid mechanical vibrations. The SDL was also placed inside a styrofoam box to protect it from noise originating from the environment.

The output power characteristics in single-frequency operation are shown in Fig. 4.5 with a maximum output power of 1 W. The corresponding optical spectrum is shown in the inset. The single-frequency operation was confirmed with a scanning FPI with a free

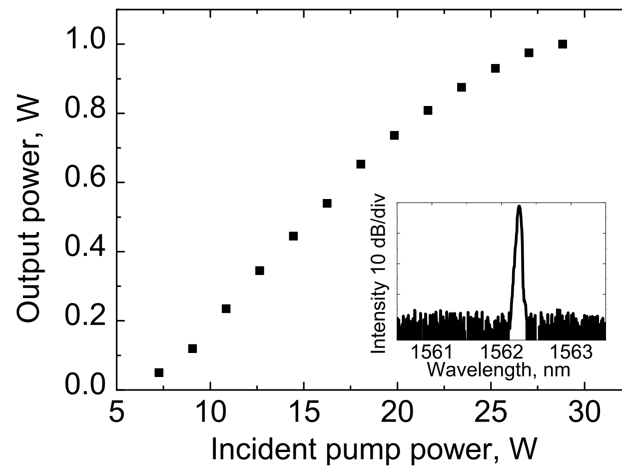

Figure 4.5: Output characteristics of the single-frequency SDL. The optical spectrum taken at output power of 1 W is shown in the inset.

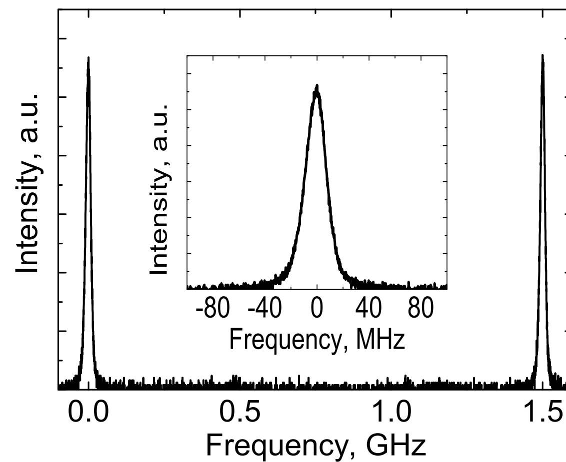

Figure 4.6: Scanning Fabry–Pérot spectrum taken at output power of 950 mW. The free-spectral range of the FPI is 1.5 GHz. A close-up of the 18 MHz (FWHM) line is shown in the inset.

spectral range of 1.5 GHz. The FPI spectrum is shown in Fig. 4.6 with a close-up of the resolution-limited 18 MHz (FWHM) line in the inset.

The SDL linewidth was also characterised using DSHI measurements that were introduced in section 3.4.3. The DSHI spectrum with a 5 km fiber delay is shown in

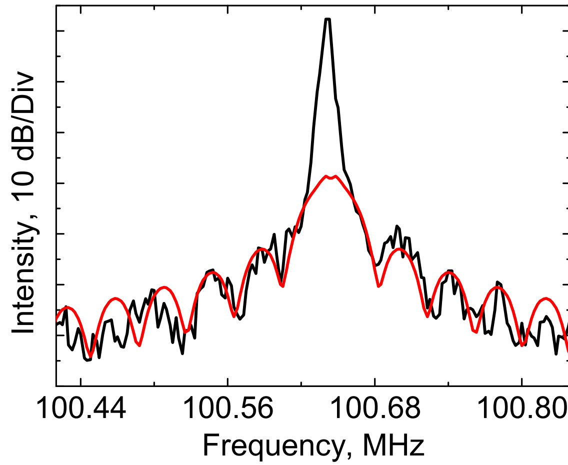

Figure 4.7: Delayed self-heterodyne interferometer spectrum taken at output power of 600 mW. Red line: fitting of Eq. 4.4.

Fig. 4.7. The oscillating pattern is centered at 100 MHz which corresponds to the frequency shift of the AOM, and has a 40 kHz period which corresponds to the 5 km fiber delay. For clarity, the oscillating pattern in Fig. 4.7 was also fitted with a Lorentzian function describing the power spectrum [241]

$$S(\nu) \propto \frac{\Delta\nu_{\mathrm{L}}}{\nu^2 + \Delta\nu_{\mathrm{L}}^2} \left(1 - e^{2\pi\Delta\nu_{\mathrm{L}}} \left[\cos(2\pi\nu\tau_{\mathrm{d}}) + 2\pi\Delta\nu_{\mathrm{L}}\tau_{\mathrm{d}}\mathrm{sinc}(2\pi\nu\tau_{\mathrm{d}})\right]\right) \tag{4.4}$$

to provide a reference for the overall signal shape excluding the peak in the middle [174, 176, 242, 243]. Here ν is the laser frequency, $\Delta\nu_{\mathrm{L}}$ the FWHM of the assumed Lorentzian line and τ_{d} the delay time. The upper limits for the laser linewidth are 27 kHz and 13 kHz for Gaussian and Lorentzian spectral distributions, respectively.

Chapter 5

Frequency conversion in semiconductor disk lasers

5.1 Introduction

Nonlinear optics describes the behaviour of light in a medium with a nonlinear response. These phenomena enable the conversion of the fundamental frequencies of lasers into a broad range of wavelengths. A review of such frequency conversion processes in SDLs is given at the beginning of this chapter. This is followed by an introduction to second-harmonic generation (SHG) or frequency-doubling. The concept of SHG is then extended to intracavity SHG, where the nonlinear crystal is placed inside the laser cavity. The chapter is concluded by a presentition of intracavity frequency-doubled SDLs emitting at the wavelengths of 650 nm and 785 nm.

5.2 Nonlinear frequency conversion in SDLs

In solid state lasers, intracavity SHG can easily magnify the intensity fluctuations of the laser due to longitudinal mode coupling via sum-frequency generation (SFG) and spatial hole burning (SHB) [244, 245]. This phenomenon is called the ”green problem”. It can be severe in gain media with long upper state lifetimes, because they store gain and allow the intensity fluctuations to grow over several cavity roundtrips [246]. However, SDLs are essentially free from these instabilities, because they have short upper state lifetimes that enable instantaneous gain (on the time scale of the optical cavity round-

trip time) and resonant periodic gain structures that prevent SHB [7, 247]. In addition, SDLs possess much higher intracavity powers at a given pump power than solid state lasers [6], which enables more efficient SHG. Therefore, SDLs are highly suitable for intracavity SHG, as also shown in Refs. [248, 249].

The most impressive results for frequency-doubled SDLs have been obtained at the blue-green-yellow wavelengths with GaAs-based structures emitting at 920–1180 nm [53, 250]. However, SDLs have also been used for third harmonic generation at 355 nm [251], fourth harmonic generation at 244 nm [252], THz emission by difference-frequency generation (DFG) [253, 254], visible emission with SFG [255, 256] and for pumping intracavity Raman lasers [257]. SDLs are also very suitable for intracavity optical parametric oscillators (ICOPO), because their short upper state lifetime makes them free of relaxation oscillations [258, 259]. Such a configuration has been utilized for generating radiation at wavelengths 3–5 μm [260–263].

5.3 Second-harmonic generation

The purpose of this section is to present an intuitive introduction to SHG. The treatment is started by considering a plane wave with a frequency ω_1 and a uniform intensity distribution. The electric field can now be expressed as

$$\widetilde{E}_1(z,t) = E_1(z)e^{-i\omega_1 t} + \text{c.c.}, \tag{5.1}$$

where c.c. denotes the complex conjugate. As the field propagates through an anisotropic dielectric medium, it can displace the electrons in the crystal atoms and induce a net polarization into the material [264]. The relationship between the applied electric field and the induced polarization can be expressed by a power series

$$\widetilde{P}(t) = \varepsilon_0(\chi^{(1)}\widetilde{E}_1(t) + \chi^{(2)}\widetilde{E}_1^2 + \chi^{(3)}\widetilde{E}_1^3 + \dots) = \widetilde{P}^{(1)}(t) + \widetilde{P}^{(2)}(t) + \widetilde{P}^{(3)}(t) + \dots, \tag{5.2}$$

where ε_0 is the permittivity and the coefficients $\chi^{(n)}$ are the n-th order susceptibilities of the material. For SHG, the essential term is the second order polarization

$$\widetilde{P}^{(2)} = 2\varepsilon_0\chi^{(2)}E_1E_1^* + \varepsilon_0\chi^{(2)}E_1^2e^{-i2\omega_1 t} + \varepsilon_0\chi^{(2)}E_1^{*2}e^{i2\omega_1 t}, \tag{5.3}$$

where the first term relates to optical rectification. The second term is proportional to the square of the electric field and can generate radiation at a second-harmonic frequency

$\omega_2 = 2\omega_1$. The third term is the complex conjugate of the second term and therefore describes the same physical process.

In order to solve the wave equation in the presence of a nonlinear polarization source term, the second-harmonic field is written as

$$\widetilde{E}_2(z,t) = E_2(z)e^{-i\omega_2 t} + \text{c.c.} = A_2(z)e^{i(k_2 z-\omega_2 t)} + \text{c.c.}, \tag{5.4}$$

where A_2 varies slowly with the distance z and

$$k_2 = \frac{n_2\omega_2}{c} \tag{5.5}$$

$$\omega_2 = \frac{2\pi c}{\lambda_2} \tag{5.6}$$

$$n_2 = \left[\varepsilon^{(1)}(\omega_2)\right]^{1/2}. \tag{5.7}$$

The corresponding nonlinear polarization source term for the second-harmonic frequency is given by

$$\widetilde{P}^{(2)} = \varepsilon_0\chi^{(2)}E_1^2 e^{-i\omega_2 t} + \text{c.c.} = 2\varepsilon_0 d_{\text{eff}}A_1^2 e^{i(2k_1 z-\omega_2 t)} + \text{c.c.}, \tag{5.8}$$

where A_1 is the slowly varying amplitude of the fundamental frequency. The coefficient d_{eff} is the effective nonlinear coefficient that collects together all the relevant contributions from the tensor element $\frac{1}{2}\chi^{(2)}$ and describes the strength of the nonlinear interaction in the material [265]. By substituting equations 5.4 and 5.8 into the wave equation, applying the slowly varying amplitude approximation and assuming an undepleted fundamental field (A_1=constant), the intensity of the second-harmonic field can be expressed as [266]

$$I_2 = \frac{8\pi^2}{n_1^2 n_2 \lambda_1^2 c\varepsilon_0}(d_{\text{eff}}I_1 L)^2 \text{sinc}^2\left(\frac{\Delta kL}{2}\right), \tag{5.9}$$

where L is the crystal length and I_1 the intensity of the fundamental field. Equation 5.9 implies that the intensity of the second-harmonic signal grows with the square of the effective nonlinear coefficient, crystal length and the intensity of the fundamental field.

The sinc^2-term in equation 5.9 also implies that the SHG efficiency depends critically on the phase mismatch Δk=2k_1-k_2 between the fundamental and the second-harmonic waves, as illustrated in Fig. 5.1(a). The most efficient SHG is obtained when Δk=0, because a constant phase relationship is conserved between the fundamental wave and the second-harmonic waves that are generated along the crystal. This means that the

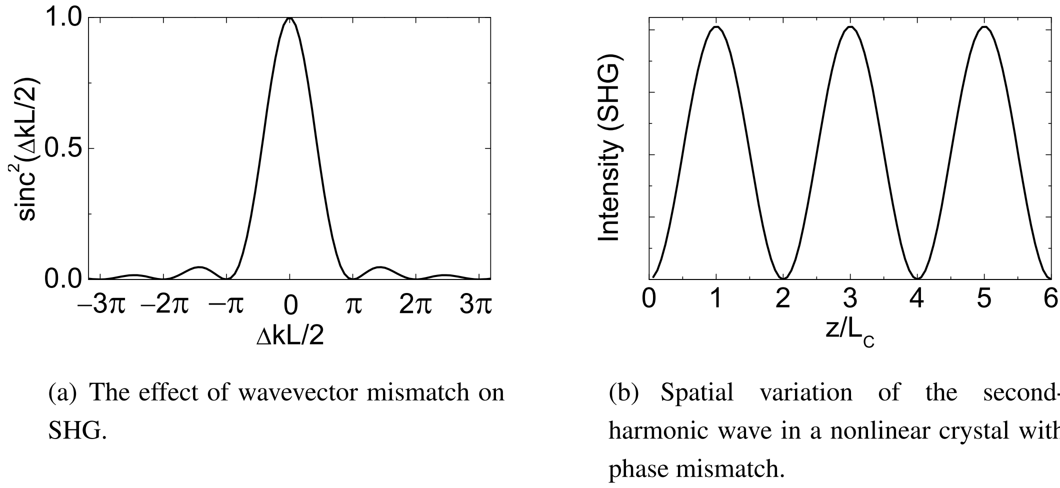

(a) The effect of wavevector mismatch on SHG.

(b) Spatial variation of the second-harmonic wave in a nonlinear crystal with phase mismatch.

Figure 5.1: Phase matching in SHG.

second-harmonic waves interfere constructively over the length of the crystal and that the second-harmonic signal accumulates with distance. However, if the phase matching condition is not fulfilled, the second-harmonic waves that are generated at different points in the nonlinear crystal start to interfere destructively and couple back into the fundamental wave. In this case, the second-harmonic field oscillates with a period $2L_c$ along the length of the crystal, as illustrated in Fig. 5.1(b). The distance L_c is called the coherence length and is the distance at which the second-harmonic wave reaches its first maximum. It depends on Δk and is given by [267]

$$L_c = \frac{\pi}{\Delta k}. \tag{5.10}$$

Phase matching (Δk=0) is not trivially obtained in nonlinear crystals, because the refractive index depends on the wavelength. Most materials exhibit normal dispersion with $n_1 < n_2$, so that

$$\Delta k = (2k_1 - k_2) = \frac{2n_1\omega_1}{c} - \frac{n_2\omega_2}{c} = \frac{4\pi}{\lambda_1}(n_2 - n_1) \neq 0. \tag{5.11}$$

However, material dispersion can be offset in birefringent crystals, wherein the fundamental and the second-harmonic wave can experience the same refractive index if they have different polarizations. These relative polarization directions of the fundamental and second-harmonic waves are also be used to categorize the SHG processes into different types. In type I phase matching, the two fundamental waves have the same polarization, and the second-harmonic wave has a polarization orthogonal to the fundamental

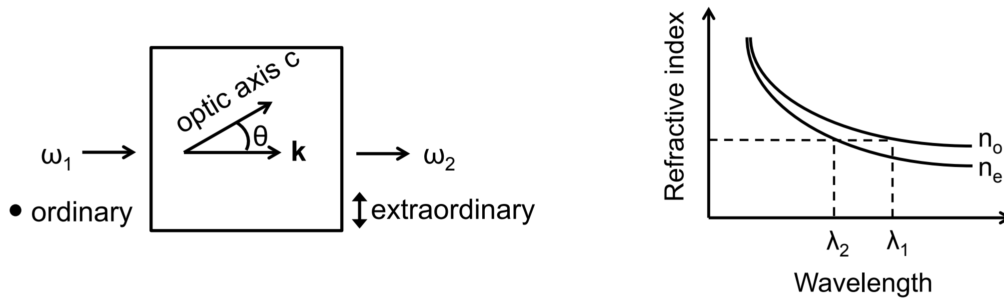

(a) Ordinary and extraordinary polarization components for SHG with type I phase matching in a negative uniaxial crystal. The symbol • depicts polarization perpendicular to the page and the symbol ↕ polarization in the plane of the page.

(b) Phase matching in a negative uniaxial crystal. The refractive index dispersion is compensated for by the birefringence of the nonlinear crystal.

Figure 5.2: Birefringent phase matching in a negative uniaxial crystal.

waves. In type II phase matching, the fundamental waves have orthogonal polarizations, and the second-harmonic wave has a polarization parallel to one of the fundamental waves.

The birefringent nonlinear crystals are characterised by the direction(s), in which the incoming light experiences no birefringence, regardless of its polarization state. Uniaxial crystals have one and biaxial crystals two of these optic axes [265]. The treatment here is limited to uniaxial crystals, where the concept of birefringent phase matching is most simply described with the ordinary n_o and extraordinary n_e refractive indices. The ordinary polarization direction is perpendicular to the plane containing the optic axis and the wave propagation vector $\boldsymbol{k}$, while the extraordinary polarization direction is in the plane containing the wave propagation vector $\boldsymbol{k}$ and the optic axis.

Uniaxial nonlinear crystals can be divided into positive uniaxial ($n_\mathrm{o} < n_\mathrm{e}$) and negative uniaxial ($n_\mathrm{o} > n_\mathrm{e}$) crystals depending on the relative magnitude of n_o and n_e. In the case of normal dispersion ($n_1 < n_2$), one would choose a negative uniaxial crystal with the fundamental wave propagating as an ordinary wave and the second-harmonic as an extraordinary wave. Such a case is illustrated in Figs. 5.2(a) and 5.2(b).

The phase matching angle θ in critically phase matched (CPM) nonlinear crystals is defined by the laser frequency (wavelength), because n_e depends on the angle θ that

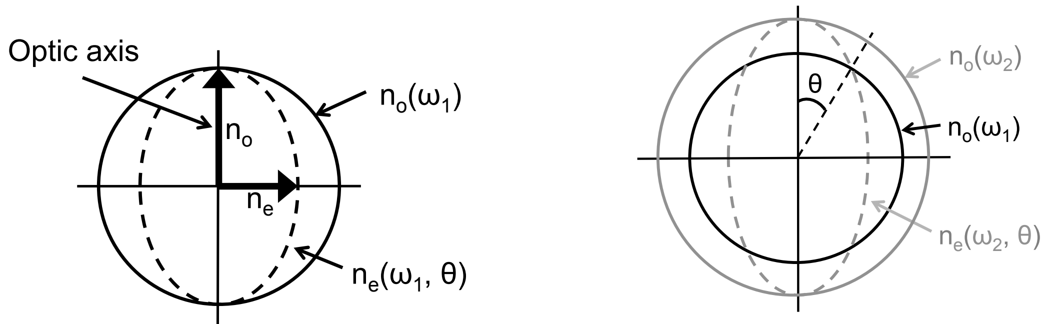

(a) Refractive index at the fundamental frequency ω_1 for a negative uniaxial crystal.

(b) Phase matching in a negative uniaxial crystal.

Figure 5.3: Refractive index ellipsoids for a negative uniaxial crystal as adapted from [267].

is shown in Fig. 5.2(a). The dependence of $n_\mathrm{o}(\omega_1)$ and $n_\mathrm{e}(\omega_1, \theta)$ on θ is illustrated in Fig. 5.3(a) for a negative uniaxial crystal. The refractive index circle for $n_\mathrm{o}(\omega_1)$ is shown again in Fig. 5.3(b), but now the refractive index ellipsoid of the second-harmonic frequency $n_\mathrm{e}(\omega_2, \theta)$ is also included. The refractive indices for the fundamental and second-harmonic wave coincide at an angle θ, so the phase matching condition $n_\mathrm{e}(\omega_2, \theta) = n_\mathrm{o}(\omega_1)$ is fulfilled.

The disadvantage of CPM is spatial walk-off since "for any direction of phase propagation the direction of energy propagation (Poynting vector) is given by the normal vector to the surface" of the refractive index ellipsoid [268]. The second-harmonic wave therefore propagates in a slightly different direction than the fundamental wave, because the normal of the ordinary refractive index circle is different from the normal of the extraordinary refractive index ellipsoid. The consequences of spatial walk-off include elliptic output beams with reduced conversion efficiencies, reduced acceptance angles and reduced acceptance bandwidths [269].

Spatial walk-off is avoided in noncritically phase matched (NCPM) crystals, because the angle θ is chosen to be 90° and the phase matching is achieved by tuning the temperature of the nonlinear crystal. This is possible since n_e is often more sensitive to temperature than n_o. This method is also less critical to the angle of the crystal and is therefore called non-critical phase matching. However, the required temperatures are often well above room temperature, which can make this method slightly inconvenient.

Finally, phase matching can also be achieved using so called quasi-phase matching,

where the sign of d_{eff} is inverted periodically after every L_c. Such a procedure allows the second-harmonic wave to grow cumulatively over the length of the crystal.

5.4 Intracavity second-harmonic generation

This section presents the fundamentals of intracavity SHG and follows the treatment given for solid state lasers in Refs. [267, 270]. Here, the nonlinear crystal is placed inside the laser cavity, where it acts as a nonlinear output coupler that couples out light at the second-harmonic frequency. This configuration can provide higher conversion efficiencies than external SHG, because the intracavity power of the laser is typically 1-2 orders of magnitude higher than the output power. Furthermore, intracavity SHG allows recirculation of the non-converted portion of the fundamental radiation, so that only a small fraction of the fundamental intracavity power needs to be converted at each round-trip for efficient SHG. For instance, for a laser with an optimal output coupler of 4 %, an intracavity conversion efficiency of 4 % corresponds to an external conversion efficiency of 100 %.

The steady-state condition for intracavity SHG is determined by equating the round-trip saturated gain with the linear and nonlinear losses

$$\frac{g_0}{1+\frac{I_1}{I_S}} = \delta + \kappa I_1, \tag{5.12}$$

where g_0 is the unsaturated small-signal round-trip gain, I_S the saturation intensity and δ the linear loss in the laser cavity. The quantity κ is the nonlinear coupling coefficient and is defined as

$$I_2 = \kappa I_1^2 \tag{5.13}$$

(with perfect phase matching) and given by

$$\kappa = \frac{8\pi^2 d_{\text{eff}}^2}{n_1^2 n_2 \lambda_1^2 c \varepsilon_0}\left(\frac{I_{1,\text{nc}}}{I_{1,\text{ge}}}\right) L^2. \tag{5.14}$$

Here the factor $I_{1,\text{nc}}/I_{1,\text{ge}}$ accounts for the different power densities in the gain element and the nonlinear crystal, since the quantities $I_{1,\text{nc}}$ and $I_{1,\text{ge}}$ denote the intensity of the fundamental field in the nonlinear crystal and the gain element, respectively. For a four-level solid state gain medium, the saturation intensity is given by

$$I_S = \frac{h\nu}{\sigma_{\text{em}}\tau_f}, \tag{5.15}$$

where h is Planck's constant, τ_f the fluorescence or upper state lifetime, and σ_{em} the emission cross section. Such an approximation has been used for SDLs [37], but an alternative approach has also been presented [271].

In the small-signal regime with negligible intracavity power depletion, the fundamental intracavity power and the conversion efficiency grow linearly while the second-harmonic power grows quadratically with increasing pump power. However, at higher pump powers the SHG process starts to deplete the fundamental intracavity power and the laser reaches a saturated regime. Consequently, the growth of the fundamental intracavity power and the conversion efficiency slow down significantly, while the second-harmonic power grows linearly with increasing pump power [255, 272, 273].

The maximum second-harmonic power as a function of κ can be obtained by differentiating Eq. 5.12 and setting $\frac{dI_1}{d\kappa}$=0, which leads to

$$\kappa_{max} = \frac{\delta}{I_S}. \tag{5.16}$$

Thus, the optimal magnitude of nonlinearity is proportional to the cavity loss and inversely proportional to the saturation intensity. In practice, the optimal nonlinear output coupling is obtained by varying the spot size of the fundamental field in the nonlinear crystal [274]. Higher conversion efficiencies are obtainable by increasing the spot size (or intensity) ratio between the gain element and the nonlinear crystal, as also implied by Eq. 5.14.

In an ideal case, the linear insertion loss of the nonlinear crystal is small compared to δ, so the optimal output coupling value and the obtainable output power are the same for the fundamental and second-harmonic radiation [275]. However, the maximum second-harmonic power can be limited by insertion losses of the nonlinear crystal and losses from additional optical components such as birefringent filters, etalons and cavity mirrors. This issue is particularly critical for low-gain lasers whose performance can be degraded by even a very small increase in intracavity losses.

5.5 Intracavity second-harmonic generation with 1.3–1.6 μm SDLs

The final section of this chapter covers the results that were obtained with intracavity SHG using the gain elements presented in sections 4.3.1 and 4.4.1 [P7, P8]. The SDLs

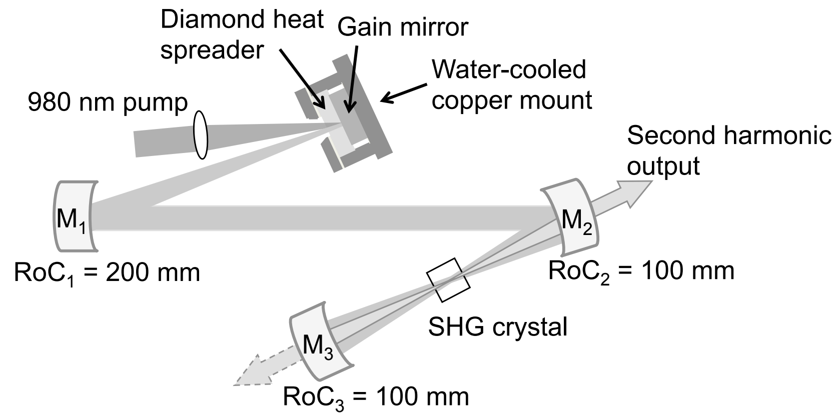

Figure 5.4: The cavity configuration for second-harmonic generation.

emitted at the wavelengths of 1.3 μm and 1.57 μm and produced second-harmonic outputs at 650 nm and 785 nm, respectively. Such frequency-doubled SDLs emitting at 1.3–1.6 μm enable convenient access to the wavelength range 650–800 nm that is not easily reached with directly emitting SDLs, as already covered in section 2.5. The best results from directly emitting SDLs in this wavelength range include 1 W at 675 nm using GaInP QWs [276] and 52 mW at 716–755 nm using InP QDs [277]. The potential applications of these devices cover a wide range that includes biophotonics [278], medicine [279], laser projection technology [280], Raman spectroscopy [281, 282], and the replacement of expensive titanium:sapphire lasers [15].

5.5.1 Frequency-doubled SDL at 650 nm

The SDL emitting at 1.3 μm was frequency-doubled using a critically phase-matched (CPM) Type-I 4-mm long BBO crystal. The mode diameter on the BBO crystal was 140 μm and the Rayleigh range 20 mm. The facets of the crystal were AR-coated for both the fundamental and the second-harmonic signals. The temperature of the gain element was kept at 7 °C, but the temperature of the BBO crystal was not controlled due to its wide thermal acceptance bandwidth [283]. A schematic of the laser cavity is shown in Fig. 5.4, where the second-harmonic output was obtained through mirrors M_2 and M_3, which were highly transmissive for the second-harmonic signal. The combined output power characteristic is shown in Fig. 5.5 with a maximum power of about 3 W. The optical spectra at various pump powers are given in the inset.

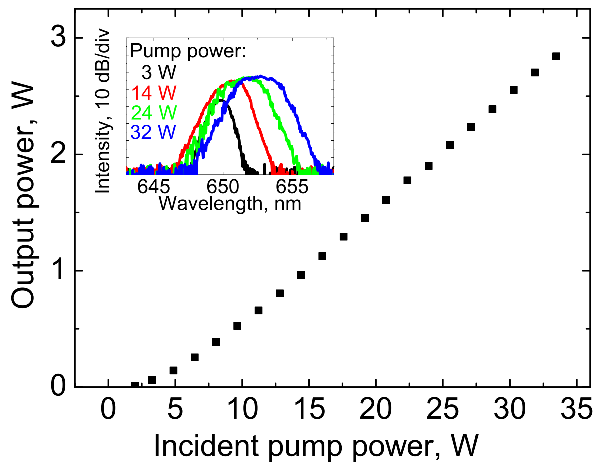

Figure 5.5: The output characteristics of the frequency-doubled SDL emitting at 650 nm. The optical spectra at various pump powers are shown in the inset.

5.5.2 Frequency-doubled SDL at 785 nm

The SDL emitting at 1.57 μm was frequency-doubled using a CPM Type-I 6-mm long LBO crystal. The mode diameter at the LBO crystal was 140 μm and the Rayleigh range 20 mm. The facets of the crystal were AR coated for both the fundamental and the second-harmonic signals. The temperature of the gain element was kept at 15 °C, whereas the temperature of the LBO crystal was kept at 25 °C to preserve the phase matching condition in the crystal [284]. A schematic of the laser cavity is shown in Fig. 5.4, where the second-harmonic output was obtained solely through mirror M_2, because M_3 was highly reflective for the second-harmonic signal. The output power characteristics are shown in Fig. 5.6 with a maximum output power of 1 W. The optical spectra at various pump powers are given in the inset.

The shape of the output characteristic resembles a laser with a relatively low conversion efficiency, in which the intracavity power grows linearly and the second-harmonic signal quadratically with pump power [285, 286]. This behavior was most likely due to two factors. First, the conversion efficiency in the LBO crystal is quite low, which implies low intracavity power depletion and therefore quadratic dependence between the pump power and the second-harmonic power. Second, the fundamental SDL wavelength shifted several nm with pump power, but the LBO crystal was aligned for maximum

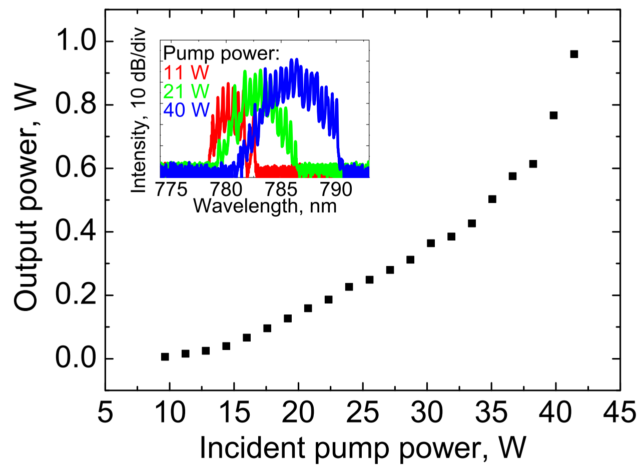

Figure 5.6: The output characteristics of the frequency-doubled 785 nm SDL. The optical spectra at various pump powers are shown in the inset.

frequency-doubled output power. Consequently, the LBO crystal was most likely phase-matched only at the longer wavelengths with higher pump powers. This problem could not be alleviated by forcing the laser to operate at the maximum SHG wavelength using birefringent filters and etalons, because they introduced excess losses which reduced the output power.

Chapter 6

Conclusion

This thesis covers issues related to semiconductor disk lasers with an emphasis on flip-chip bonding, semiconductor-dielectric-metal compound mirrors, the integration of GaAs-based DBRs onto InP-based active regions, single-frequency operation and intracavity second-harmonic generation. The first three issues relate to the SDL gain element processing, while the latter two issues relate to the SDL cavity configuration. The main achievements are summarized below.

- Gold-gold thermocompression bonding was demonstrated for flip-chip SDLs emitting at 1 μm. The thin Au bonding layer was shown to provide high thermal conductance between the SDL gain element and the CVD diamond heat spreader, which enabled 45-50 % higher output powers than conventional bonding with indium. Therefore, the bonding procedure provides a step towards an ideal flip-chip SDL, where the bottom of the gain element is in direct contact with the heat spreader.
- The DBR reflectivity was enhanced by placing a thin Al_2O_3 dielectric layer between the semiconductor DBR and the highly reflecting Al metallization layer. The design enabled 30 % thinner DBRs than the conventional design, where the DBR is finished with a highly reflecting Au layer. The thin Al_2O_3 layer was also shown to introduce a negligible contribution to the thermal resistance of the SDL. The validity of the design was demonstrated with SDLs emitting at 1.05 μm. However, the biggest benefits are expected for flip-chip SDLs emitting beyond 1 μm, because the DBR thickness increases with wavelength.
- Three procedures for bonding GaAs-based DBRs onto InP-based active regions

were presented. Such integration is essential for SDLs emitting in the 1.3–1.6 μm wavelength range, because InP-based materials lack the appropriate compounds for the DBR section while GaAs-based materials lack the appropriate compounds for the gain section. The bonding methods comprised wafer fusion at 650 °C, intermediate layer bonding with SiO_2 layers at 200 °C, and intermediate layer bonding with a monolayer of (3-Mercaptopropyl)tri-methoxysilane (MPTMS) at 200 °C. The three methods enabled multi-watt output powers in the 1.3–1.6 μm wavelength range. In particular, output powers over 6 W were demonstrated with wafer-fused SDLs emitting at 1.3 μm in the intracavity diamond configuration and in the flip-chip configuration. The results also included 4.6 W of output power at 1.58 μm in the intracavity diamond configuration.

- A single-frequency SDL was demonstrated at 1.05 μm using a GaAs-based flip-chip structure. The output power reached 4.6 W and the coherence length was > 1.7 km in optical fiber. Single-frequency operation was also demonstrated with a wafer-fused SDL emitting at 1.56 μm in the intracavity diamond configuration. In this case, the output power reached 1 W and the coherence length was > 5 km in optical fiber. Such a combination of high output power and narrow linewidth is particularly interesting for light detection and ranging, free space communications and high resolution spectroscopy.
- Second-harmonic generation was demonstrated with wafer-fused SDLs emitting at 1.3 μm and 1.57 μm in the intracavity diamond configuration. The output powers reached 3 W at 650 nm and 1 W at 785 nm. These frequency-doubled SDLs avoid the drawbacks associated with directly emitting SDLs in the 650–800 nm wavelength range. These drawbacks include low carrier confinement in the quantum wells which leads to high temperature sensitivity, DBR layers with relatively low refractive index contrast and low thermal conductivity, and the requirement for pump lasers emitting in the visible wavelength range.

Finally, the work in this thesis can be considered a step towards high-brightness flip-chip SDLs emitting in the wavelength range 1.25–1.7 μm. Such progress would avoid the drawbacks of intracavity diamonds, mimic the impressive evolution of flip-chip SDLs emitting in the 1 μm wavelength region, and enable high-brightness light sources in the wavelength range 625–850 nm. Moreover, the emission wavelength of these devices could be tailored to match the desired application simply by altering the composition of the gain material.

Bibliography

[1] M. Kuznetsov, F. Hakimi, R. Sprague, and A. Mooradian, "High-power (> 0.5-W CW) diode-pumped vertical-external-cavity surface-emitting semiconductor lasers with circular TEM_{00} beams," *IEEE Photonics Technology Letters*, vol. 9, no. 8, pp. 1063–1065, 1997.

[2] A. Giesen, H. Hügel, A. Voss, K. Wittig, U. Brauch, and H. Opower, "Scalable concept for diode-pumped high-power solid-state lasers," *Applied Physics B: Lasers and Optics*, vol. 58, no. 5, pp. 365–372, 1994.

[3] J. Hastie, S. Calvez, and M. Dawson, "Semiconductor disk lasers (VECSELs)," in *Semiconductor Lasers: Fundamentals and Applications*, A. Baranov and E. Tournie, Eds. Woodhead Publishing, 2013, p. 341.

[4] A. Garnache, M. Myara, A. Laurain, A. Bouchier, J. Perez, P. Signoret, I. Sagnes, and D. Romanini, "Single frequency free-running low noise compact extended-cavity semiconductor laser at high power level," in *Proceedings of International Conference on Space Optics*, vol. S17, 2008, pp. 257–258.

[5] A. Garnache, A. Laurain, M. Myara, J.-P. Perez, L. Cerutti, A. Michon, G. Beaudoin, I. Sagnes, P. Cermak, and D. Romanini, "Design and properties of high-power highly coherent single-frequency VECSEL emitting in the near- to mid-IR for photonic applications," in *Proceedings of SPIE*, vol. 7919, 2011, pp. 791 914:1–791 914:11.

[6] M. Arrigoni, B. Morioka, and A. Lepert, "Optically pumped semiconductor lasers: Green OPSLs poised to enter scientific pump-laser market," *Laser Focus World*, Oct. 2009.

[7] G. Baili, F. Bretenaker, M. Alouini, L. Morvan, D. Dolfi, and I. Sagnes, "Experimental investigation and analytical modeling of excess intensity noise in semiconductor class-A lasers," *Journal of Lightwave Technology*, vol. 26, no. 8, pp. 952–961, 2008.

[8] "Advances in laser diode and OPSL technologies render ion and metal vapor lasers obsolete," Coherent Inc., white paper,

https://www.coherent.com/downloads/Diodes_and_OPSL_vs_HeCd.pdf, accessed 2014-10-14.

[9] C. Kannengiesser, V. Ostroumov, V. Pfeufer, W. Seelert, C. Simon, R. von Elm, and A. Zuck, "Ten years optically pumped semiconductor lasers: review, state-of-the-art, and future developments," in *Proceedings of SPIE*, vol. 7578, 2010, pp. 75 780W:1–75 780W:11.

[10] M. Schulze and A. Masters, "Optically pumped semiconductor lasers expand the scope of potential applications," *Laser Focus World*, Dec. 2006.

[11] B. Morioka, "High-power optically pumped semiconductor laser applications," in *Proceedings of SPIE*, vol. 7919, 2011, pp. 791 913:1–791 914:11.

[12] A. Richter, E. Heumann, G. Huber, V. Ostroumov, and W. Seelert, "Power scaling of semiconductor laser pumped Praseodymium-lasers," *Optics Express*, vol. 15, no. 8, pp. 5172–5178, 2007.

[13] A. Chamorovskiy and O. Okhotnikov, "Nonlinear fibre-optic devices pumped by semiconductor disk lasers," *Quantum Electronics*, vol. 42, no. 11, pp. 964–979, 2012.

[14] Y. Jeong, L. Vazquez-Zuniga, Y. Kwon, S. Lee, and H. Kim, "High-power fiber laser technology for wavelength conversion," in *IEEE Proceedings of 6th International Conference on Advanced Infocomm Technology*, 2013, p. 42.

[15] M. Schmid, "Optically in-well-pumped VECSELs: An attractive new source in the near-IR," *Photonics Spectra*, vol. 38, no. 11, pp. 58–65, 2004.

[16] K. Iga, "Surface-emitting laser – its birth and generation of new optoelectronics field," *IEEE Journal of Selected Topics in Quantum Electronics*, vol. 6, no. 6, pp. 1201–1215, 2000.

[17] J.-F. Seurin, A. L. D'Asaro, and C. Ghosh, "A new application for VCSELs: High-power pump lasers," *Photonics Spectra*, vol. 41, no. 7, pp. 66–68, 2007.

[18] J. McInerney, A. Mooradian, A. Lewis, A. Shchegrov, E. Strzelecka, D. Lee, J. Watson, M. Liebman, G. Carey, B. Cantos, W. Hitchens, and D. Heald, "High-power surface emitting semiconductor laser with extended vertical compound cavity," *Electronics Letters*, vol. 39, no. 6, pp. 523–525, 2003.

[19] C. Zaugg, S. Gronenborn, H. Moench, M. Mangold, M. Miller, U. Weichmann, W. Pallmann, M. Golling, B. Tilma, and U. Keller, "Absorber and gain chip optimization to improve performance from a passively modelocked electrically pumped

vertical external cavity surface emitting laser," *Applied Physics Letters*, vol. 104, no. 12, pp. 121 115:1–121 115:5, 2014.

[20] P. Zhao, B. Xu, R. van Leeuwen, T. Chen, L. Watkins, D. Zhou, P. Gao, G. Xu, Q. Wang, and C. Ghosh, "Compact 4.7 W, 18.3% wall-plug efficiency green laser based on an electrically pumped VECSEL using intracavity frequency doubling," *Optics letters*, vol. 39, no. 16, pp. 4766–4768, 2014.

[21] P. Kreuter, B. Witzigmann, D. Maas, Y. Barbarin, T. Südmeyer, and U. Keller, "On the design of electrically pumped vertical-external-cavity surface-emitting lasers," *Applied Physics B*, vol. 91, no. 2, pp. 257–264, 2008.

[22] Y. Barbarin, M. Hoffmann, W. Pallmann, I. Dahhan, P. Kreuter, M. Miller, J. Baier, H. Moench, M. Golling, T. Südmeyer, B. Witzigmann, and U. Keller, "Electrically pumped vertical external cavity surface emitting lasers suitable for passive mode-locking," *IEEE Journal of Selected Topics in Quantum Electronics*, vol. 17, no. 6, pp. 1779–1786, 2011.

[23] J. Orchard, D. T. Childs, L. Lin, B. Stevens, D. Williams, and R. Hogg, "Tradeoffs in the realization of electrically pumped vertical external cavity surface emitting lasers," *IEEE Journal of Selected Topics in Quantum Electronics*, vol. 17, no. 6, pp. 1745–1752, 2011.

[24] M. Kuznetsov, F. Hakimi, R. Sprague, A. Mooradian, M. Inc, and M. Acton, "Design and characteristics of high-power (> 0.5-W CW) diode-pumped vertical-external-cavity surface-emitting semiconductor lasers with circular TEM_{00} beams," *IEEE Journal of Selected Topics in Quantum Electronics*, vol. 5, no. 3, pp. 561–573, 1999.

[25] A. Giesen and J. Speiser, "Fifteen years of work on thin-disk lasers: results and scaling laws," *IEEE Journal of Selected Topics in Quantum Electronics*, vol. 13, no. 3, pp. 598–609, 2007.

[26] K.-S. Kim, J. Yoo, G. Kim, S. Lee, S. Cho, J. Kim, T. Kim, and Y. Park, "Enhancement of pumping efficiency in a vertical-external-cavity surface-emitting laser," *IEEE Photonics Technology Letters*, vol. 19, no. 23, pp. 1925–1927, 2007.

[27] P. Savolainen, "Puolijohdelasereiden peilipäätyjen pinnoitus," Master's thesis, Tampere University of Technology, 1992.

[28] D. Babic and S. Corzine, "Analytic expressions for the reflection delay, penetration depth, and absorptance of quarter-wave dielectric mirrors," *IEEE Journal of Quantum Electronics*, vol. 28, no. 2, pp. 514–524, 1992.

[29] M. Raja, S. Brueck, M. Osinski, C. Schaus, J. G. McInerney, T. Brennan, and B. Hammons, "Resonant periodic gain surface-emitting semiconductor lasers," *IEEE Journal of Quantum Electronics*, vol. 25, no. 6, pp. 1500–1512, 1989.

[30] S. Corzine, R. Geels, J. Scott, R.-H. Yan, and L. Coldren, "Design of Fabry–Pérot surface-emitting lasers with a periodic gain structure," *IEEE Journal of Quantum Electronics*, vol. 25, no. 6, pp. 1513–1524, 1989.

[31] N. Schulz, J. Hopkins, M. Rattunde, D. Burns, and J. Wagner, "High-brightness long-wavelength semiconductor disk lasers," *Laser & Photonics Reviews*, vol. 2, no. 3, pp. 160–181, 2008.

[32] K. Wilcox, A. Tropper, H. Beere, D. Ritchie, B. Kunert, B. Heinen, and W. Stolz, "4.35 kW peak power femtosecond pulse mode-locked VECSEL for supercontinuum generation," *Optics Express*, vol. 21, no. 2, pp. 1599–1605, 2013.

[33] C. Borgentun, J. Bengtsson, A. Larsson, F. Demaria, A. Hein, and P. Unger, "Optimization of a broadband gain element for a widely tunable high-power semiconductor disk laser," *IEEE Photonics Technology Letters*, vol. 22, no. 13, pp. 978–980, 2010.

[34] R. Bedford, M. Kolesik, J. Chilla, M. Reed, T. Nelson, and J. Moloney, "Power-limiting mechanisms in VECSELs," in *Proceedings of SPIE*, vol. 5814, 2005, pp. 199–208.

[35] E. Kuhn, A. Thranhardt, C. Buckers, S. W. Koch, J. Hader, and J. Moloney, "Numerical study of the influence of an antireflection coating on the operating properties of vertical-external-cavity surface-emitting lasers," *Journal of Applied Physics*, vol. 106, no. 6, pp. 063 105–063 105, 2009.

[36] A. Zakharian, J. Hader, J. Moloney, and S. Koch, "VECSEL threshold and output power-shutoff dependence on the carrier recombination rates," *IEEE Photonics Technology Letters*, vol. 17, no. 12, pp. 2511–2513, 2005.

[37] U. Keller and A. Tropper, "Passively modelocked surface-emitting semiconductor lasers," *Physics Reports*, vol. 429, no. 2, pp. 67–120, 2006.

[38] M. Mangold, V. J. Wittwer, O. D. Sieber, M. Hoffmann, I. L. Krestnikov, D. A. Livshits, M. Golling, T. Südmeyer, and U. Keller, "VECSEL gain characterization," *Optics Express*, vol. 20, no. 4, pp. 4136–4148, 2012.

[39] A. Laurain, J. Hader, Y.-Y. Lai, T.-L. Wang, M. Yarborough, G. Balakrishnan, T. Rotter, P. Ahirwar, and J. Moloney, "Influence of non-radiative carrier losses on pulsed and continuous VECSEL performance," in *Proceedings of SPIE*, vol. 8242, 2012, pp. 82 420S:1–82 420S:10.

[40] N. Schulz, M. Rattunde, C. Ritzenthaler, B. Rosener, C. Manz, K. Kohler, and J. Wagner, "Effect of the cavity resonance-gain offset on the output power characteristics of GaSb-based VECSELs," *IEEE Photonics Technology Letters*, vol. 19, no. 21, pp. 1741–1743, 2007.

[41] T.-L. Wang, Y. Kaneda, J. Hader, J. Moloney, B. Kunert, W. Stolz, and S. Koch, "Strategies for power scaling VECSELs," in *Proceedings of SPIE*, vol. 8242, 2012, pp. 824 209:1–824 209:8.

[42] R. Häring, R. Paschotta, A. Aschwanden, E. Gini, F. Morier-Genoud, and U. Keller, "High-power passively mode-locked semiconductor lasers," *IEEE Journal of Quantum Electronics*, vol. 38, no. 9, pp. 1268–1275, 2002.

[43] A. Maclean, R. Birch, P. Roth, A. Kemp, and D. Burns, "Limits on efficiency and power scaling in semiconductor disk lasers with diamond heatspreaders," *Journal of Optical Society of America B*, vol. 26, no. 12, pp. 2228–2236, 2009.

[44] A. Chernikov, J. Herrmann, M. Scheller, M. Koch, B. Kunert, W. Stolz, S. Chatterjee, S. Koch, T. Wang, Y. Kaneda, J. Yarborough, J. Hader, and J. Moloney, "Influence of the spatial pump distribution on the performance of high power vertical-external-cavity surface-emitting lasers," *Applied Physics Letters*, vol. 97, no. 19, pp. 191 110:1–191 110:3, 2010.

[45] L. Hunziker, Q.-Z. Shu, D. Bauer, C. Ihli, G. Mahnke, M. Rebut, J. Chilla, A. Caprara, H. Zhou, E. Weiss, and K. Murray, "Power-scaling of optically pumped semiconductor lasers," in *Proceedings of SPIE*, vol. 6451, 2007, pp. 64 510A:1–64 510A:6.

[46] S. Chatterjee, A. Chernikov, J. Herrmann, M. Scheller, M. Koch, B. Kunert, W. Stolz, S. Koch, T.-L. Wang, Y. Kaneda, J. Yarborough, J. Hader, and J. Moloney, "Power scaling and heat management in high-power VECSELs," in *Proceesings of Conference on Lasers and Electro-Optics*, May 2011, p. 1.

[47] V. Ostroumov, C. Simon, H. Schwarze, R. von Elm, W. Seelert, and J. Lindfors, "1 W 488 nm CW air cooled optically pumped semiconductor laser," in *Proceedings of SPIE*, vol. 6871, 2008, pp. 687 118:1–687 118:7.

[48] S. Kaspar, M. Rattunde, T. Töpper, R. Moser, S. Adler, C. Manz, K. Köhler, and J. Wagner, "Recent advances in 2-μm GaSb-based semiconductor disk laser – power scaling, narrow-linewidth and short-pulse operation," *IEEE Journal of Selected Topics in Quantum Electronics*, vol. 19, no. 4, pp. 1 501 908:1–1 501 908:8, 2013.

[49] C. Hessenius, M. Fallahi, J. Moloney, and R. Bedford, “Lateral lasing and ASE reduction in VECSELs,” in *Proceedings of SPIE*, vol. 7919, 2011, pp. 791 909:1–791 909:8.

[50] T. Töpper, M. Rattunde, S. Kaspar, R. Moser, C. Manz, K. Köhler, and J. Wagner, “High-power 2.0 μm semiconductor disk laser – Influence of lateral lasing,” *Applied Physics Letters*, vol. 100, no. 19, pp. 192 107:1–192 107:3, 2012.

[51] E. Saarinen, A. Härkönen, S. Suomalainen, and O. Okhotnikov, “Power scalable semiconductor disk laser using multiple gain cavity,” *Optics Express*, vol. 14, no. 26, pp. 12 868–12 871, 2006.

[52] L. Fan, M. Fallahi, J. Hader, A. Zakharian, J. Moloney, J. Murray, R. Bedford, W. Stolz, and S. W. Koch, “Multichip vertical-external-cavity surface-emitting lasers: a coherent power scaling scheme,” *Optics Letters*, vol. 31, no. 24, pp. 3612–3614, 2006.

[53] J. Chilla, Q.-Z. Shu, H. Zhou, E. Weiss, M. Reed, and L. Spinelli, “Recent advances in optically pumped semiconductor lasers,” in *Proceedings of SPIE*, vol. 6451, 2007, pp. 645 109:1–645 109:10.

[54] B. Rosener, M. Rattunde, R. Moser, C. Manz, K. Kohler, and J. Wagner, “GaSb-based optically pumped semiconductor disk laser using multiple gain elements,” *IEEE Photonics Technology Letters*, vol. 21, no. 13, pp. 848–850, 2009.

[55] Z. Liau, “Semiconductor wafer bonding via liquid capillarity,” *Applied Physics Letters*, vol. 77, no. 5, pp. 651–653, 2000.

[56] S. Calvez, J. Hastie, M. Guina, O. Okhotnikov, and M. Dawson, “Semiconductor disk lasers for the generation of visible and ultraviolet radiation,” *Laser & Photonics Reviews*, vol. 3, no. 5, pp. 407–434, 2009.

[57] W. Koechner, *Solid-state laser engineering*, 6th ed. Springer, 2006, Chapter 5.

[58] C. Wang, G. Wang, A. Hicks, D. Dudley, H. Pang, and N. Hodgson, “High-power Q-switched TEM_{00} mode diode-pumped solid state lasers with > 30 W output power at 355 nm,” in *Proceedings of SPIE*, vol. 6100, 2006, pp. 610 019:1–610 019:14.

[59] L. Hunziker, C. Ihli, and D. Steingrube, “Miniaturization and power scaling of fundamental mode optically pumped semiconductor lasers,” *IEEE Journal of Selected Topics in Quantum Electronics*, vol. 13, no. 3, pp. 610–618, 2007.

[60] A. Caprara, “Aberration insensitive resonators for OPS lasers,” in *Proceedings of SPIE*, vol. 7193, 2009, pp. 719 314:1–719 314:16.

[61] B. Hitz, “Multiwatt VECSEL output is wavelength-tunable,” *Photonics Spectra*, March, 2006.

[62] C. Hessenius, M. Lukowski, J. Moloney, and M. Fallahi, “Wavelength tuning of VECSELs by cavity geometry,” in *Proceedings of SPIE*, vol. 8242, 2012, pp. 82 420B:1–82 420B:8.

[63] A. Kemp, G. Valentine, and D. Burns, “Progress towards high-power, high-brightness neodymium-based thin-disk lasers,” *Progress in Quantum Electronics*, vol. 28, no. 6, pp. 305–344, 2004.

[64] L. A. Spinelli and A. Caprara, “Resonant pumping of thin-disk laser with an optically pumped external-cavity surface-emitting semiconductor laser,” Dec. 17 2009, US Patent App. 12/641,184.

[65] A. Chernikov, J. Herrmann, M. Koch, B. Kunert, W. Stolz, S. Chatterjee, S. W. Koch, T.-L. Wang, Y. Kaneda, J. Yarborough, J. Hader, and J. Moloney, “Heat management in high-power vertical-external-cavity surface-emitting lasers,” *IEEE Journal of Selected Topics in Quantum Electronics*, vol. 17, no. 6, pp. 1772–1778, 2011.

[66] Y. Chen and Y. Lan, “Dynamics of helical-wave emission in a fiber-coupled diode end-pumped solid-state laser,” *Applied Physics B*, vol. 73, no. 1, pp. 11–14, 2001.

[67] J. Berger, D. Anthon, A. Caprara, J. Chilla, S. Govorkov, A. Lepert, W. Mefferd, Q.-Z. Shu, and L. Spinelli, “20 watt CW TEM_{00} intracavity doubled optically pumped semiconductor laser at 532 nm,” in *Proceedings of SPIE*, vol. 8242, 2012, pp. 824 206:1–824 206:7.

[68] B. Heinen, T.-L. Wang, M. Sparenberg, A. Weber, B. Kunert, J. Hader, S. Koch, J. Moloney, M. Koch, and W. Stolz, “106 W continuous-wave output power from vertical-external-cavity surface-emitting laser,” *Electronics Letters*, vol. 48, no. 9, pp. 516–517, 2012.

[69] S. Ranta, M. Tavast, T. Leinonen, N. Van Lieu, G. Fetzer, and M. Guina, “1180 nm VECSEL with output power beyond 20 W,” *Electronics Letters*, vol. 49, no. 1, pp. 59–60, 2013.

[70] S. Yellen, R. Waters, Y. Chen, B. Soltz, S. Fischer, D. Fekete, and J. Ballantyne, “20 000 h InGaAs quantum well lasers,” *Electronics Letters*, vol. 26, no. 25, pp. 2083–2084, 1990.

[71] W. Horn, “High power diode lasers for industrial applications,” *Laser Technik Journal*, vol. 4, no. 3, pp. 62–65, 2007.

[72] B. Sumpf, K.-H. Hasler, P. Adamiec, F. Bugge, F. Dittmar, J. Fricke, H. Wenzel, M. Zorn, G. Erbert, and G. Trankle, “High-brightness quantum well tapered lasers,” *IEEE Journal of Selected Topics in Quantum Electronics*, vol. 15, no. 3, pp. 1009–1020, 2009.

[73] A. Karim, S. Björlin, J. Piprek, and J. Bowers, “Long-wavelength vertical-cavity lasers and amplifiers,” *IEEE Journal of Selected Topics in Quantum Electronics*, vol. 6, no. 6, pp. 1244–1253, 2000.

[74] J. Piprek, D. Babić, and J. Bowers, “Simulation and analysis of 1.55 μm double-fused vertical-cavity lasers,” *Journal of Applied Physics*, vol. 81, no. 8, pp. 3382–3390, 1997.

[75] A. F. Phillips, S. J. Sweeney, A. R. Adams, and P. J. Thijs, “The temperature dependence of 1.3- and 1.5-μm compressively strained InGaAs(P) MQW semiconductor lasers,” *IEEE Journal of Selected Topics in Quantum Electronics*, vol. 5, no. 3, pp. 401–412, 1999.

[76] H. Lindberg, M. Strassner, E. Gerster, J. Bengtsson, and A. Larsson, “Thermal management of optically pumped long-wavelength InP-based semiconductor disk lasers,” *IEEE Journal of Selected Topics in Quantum Electronics*, vol. 11, no. 5, pp. 1126–1134, 2005.

[77] L. Mawsi, S. Rusli, A. Al-Muhanna, and J. Wade, “Short-wavelength (0.7 μm < λ < 0.78 μm) high-power InGaAsP-active diode lasers,” *IEEE Journal of Selected Topics in Quantum Electronics*, vol. 5, no. 3, pp. 785–791, 1999.

[78] G. Erbert, F. Bugge, A. Knauer, J. Sebastian, A. Thies, H. Wenzel, M. Weyers, and G. Trankle, “High-power tensile-strained GaAsP-AlGaAs quantum-well lasers emitting between 715 and 790 nm,” *IEEE Journal of Selected Topics in Quantum Electronics*, vol. 5, no. 3, pp. 780–784, 1999.

[79] M. Emanuel, J. Skidmore, M. Jansen, and R. Nabiev, “High-power InAlGaAs-GaAs laser diode emitting near 731 nm,” *IEEE Photonics Technology Letters*, vol. 9, no. 11, pp. 1451–1453, 1997.

[80] K. Johnson, M. Hibbs-Brenner, W. Hogan, and M. Dummer, “Advances in red VCSEL technology,” *Advances in Optical Technologies*, vol. 2012, 2012.

[81] M. Schmid, S. Benchabane, F. Torabi-Goudarzi, R. Abram, A. Ferguson, and E. Riis, “Optical in-well pumping of a vertical-external-cavity surface-emitting laser,” *Applied Physics Letters*, vol. 84, no. 24, pp. 4860–4862, 2004.

[82] S. McGinily, R. Abram, K. Gardner, E. Riis, A. Ferguson, and J. Roberts, “Novel gain medium design for short-wavelength vertical-external-cavity surface-emitting laser,” *IEEE Journal of Quantum Electronics*, vol. 43, no. 6, pp. 445–450, 2007.

[83] M. Rahim, A. Khiar, F. Felder, M. Fill, and H. Zogg, “4.5 μm wavelength vertical external cavity surface emitting laser operating above room temperature,” *Applied Physics Letters*, vol. 94, pp. 201 112:1–201 112:3, 2009.

[84] M. Rahim, F. Felder, M. Fill, and H. Zogg, “Optically pumped 5 μm IV-VI VECSEL with Al-heat spreader,” *Optics Letters*, vol. 33, no. 24, pp. 3010–3012, 2008.

[85] T. Wunderer, J. E. Northrup, Z. Yang, M. Teepe, A. Strittmatter, N. M. Johnson, P. Rotella, and M. Wraback, “In-well pumping of InGaN/GaN vertical-external-cavity surface-emitting lasers,” *Applied Physics Letters*, vol. 99, no. 20, pp. 201 109:1–201 109:3, 2011.

[86] S. Vetter and S. Calvez, “Thermal management of near-infrared semiconductor disk lasers with AlGaAs mirrors and lattice (mis)matched active regions,” *IEEE Journal of Quantum Electronics*, vol. 48, no. 3, pp. 345–352, 2012.

[87] K. Kim, J. Yoo, S. Cho, S. Lee, S. Lim, J. Kim, J. Lee, T. Kim, and Y. Park, “1060 nm vertical-external-cavity surface-emitting lasers with an optical-to-optical efficiency of 44% at room temperature,” *Applied Physics Letters*, vol. 88, pp. 091 107:1–091 107:3, 2006.

[88] K. Kim, J. Yoo, S. Lee, S. Lim, J. Kim, J. Lee, S. Cho, T. Kim, and Y. Park, “Highly efficient InGaAs QW vertical external cavity surface emitting lasers emitting at 1060nm,” *Journal of Crystal Growth*, vol. 287, no. 2, pp. 629–632, 2006.

[89] J. Kim, J. Yoo, S. Cho, K. Kim, G. Kim, J. Lee, S. Lee, T. Kim, and Y. Park, “Effect of the properties of an intracavity heat spreader on second harmonic generation in vertical-external-cavity surface-emitting laser,” *Journal of Applied Physics*, vol. 101, pp. 073 101:1–073 101:4, 2007.

[90] A. Kemp, G. Friel, T. Lake, R. Conroy, and B. Sinclair, “Polarization effects, birefringent filtering, and single-frequency operation in lasers containing a birefringent gain crystal,” *IEEE Journal of Quantum Electronics*, vol. 36, no. 2, pp. 228–235, 2000.

[91] P. Millar, R. Birch, A. Kemp, and D. Burns, “Synthetic diamond for intracavity thermal management in compact solid-state lasers,” *IEEE Journal of Quantum Electronics*, vol. 44, no. 8, pp. 709–717, 2008.

[92] T. Leinonen, V.-M. Korpijärvi, A. Härkönen, and M. Guina, “Recent advances in the development of yellow-orange GaInNAs-based semiconductor disk lasers,” in *Proceedings of SPIE*, vol. 8242, 2012, pp. 824 208:1–824 208:7.

[93] I. Friel, S. Clewes, H. Dhillon, N. Perkins, D. Twitchen, and G. Scarsbrook, “Control of surface and bulk crystalline quality in single crystal diamond grown by chemical vapour deposition,” *Diamond and Related Materials*, vol. 18, no. 5-8, pp. 808–815, 2009.

[94] X. Liu, R. Davis, L. Hughes, M. Rasmussen, R. Bhat, C. Zah, and J. Stradling, “A study on the reliability of indium solder die bonding of high power semiconductor lasers,” *Journal of Applied Physics*, vol. 100, pp. 013 104:1–013 104:11, 2006.

[95] G. Matijasevic, C. Lee, and C. Wang, “Au-Sn alloy phase diagram and properties related to its use as a bonding medium,” *Thin Solid Films*, vol. 223, no. 2, pp. 276–287, 1993.

[96] C. Lee, C. Wang, and G. Matijasevic, “Au-In bonding below the eutectic temperature,” *IEEE Transactions on components, hybrids, and manufacturing technology*, vol. 16, no. 3, pp. 311–316, 1993.

[97] S. Farrens, “Metal based wafer level packaging,” in *Proceedings of the International Wafer-Level Packaging Conference*, 2008, pp. 1–7.

[98] S. Weiss, E. Zakel, and H. Reichl, “Mounting of high power laser diodes on diamond heatsinks,” *IEEE Transactions on Components and Packaging Technologies*, vol. 19, no. 1, pp. 46–53, 1996.

[99] T. Wang, Y. Kaneda, J. Yarborough, J. Hader, J. Moloney, A. Chernikov, S. Chatterjee, S. Koch, B. Kunert, and W. Stolz, “High-power optically pumped semiconductor laser at 1040 nm,” *IEEE Photonics Technology Letters*, vol. 22, no. 9, pp. 661–663, 2010.

[100] G. Humpston and D. Jacobson, *Principles of Soldering*. ASM International, 2004, p. 226.

[101] B. Williams, S. Kumar, Q. Hu, and J. Reno, “Operation of terahertz quantum-cascade lasers at 164 K in pulsed mode and at 117 K in continuous-wave mode,” *Optics Express*, vol. 13, no. 9, pp. 3331–3339, 2005.

[102] Y. Ding, C. Wang, L. Mingyu, and B. Han-Sur, “Aging effects on fracture behavior of 63Sn37Pb eutectic solder during tensile tests under the SEM,” *Materials Science & Engineering A*, vol. 384, pp. 314–323, 2004.

[103] J. Ronnie Teo, Z. Wang, X. Shi, G. Li, and S. Yuan, "Influence of bonding temperature and applied load on the bonding integrity and optical performance of face-down bonded ridge-waveguide lasers," *Journal of Electronic Materials*, vol. 36, no. 12, pp. 1635–1642, 2007.

[104] A. Chakraborty and J. Earthman, "Numerical models of creep cavitation in single phase, dual phase and fully lamellar titanium aluminide," *Acta Materialia*, vol. 45, no. 11, pp. 4615–4626, 1997.

[105] P. Lall, M. Pecht, and E. Hakim, *Influence of temperature on microelectronics and system reliability*. CRC Press, 1997, chapter 3.

[106] S. Weiss, V. Bader, G. Azdasht, P. Kasulke, E. Zakel, and H. Reichl, "Fluxless die bonding of high power laser bars using the AuSn-metallurgy," in *IEEE Proceedings of the 47th Electronic Components and Technology Conference*. IEEE, 1997, pp. 780–787.

[107] R. Bedford, T. Dang, and D. Tomich, "Recent VECSEL developments for sensors applications," in *Proceedings of SPIE*, vol. 8242, 2012, pp. 82 420W:1–82 420W:9.

[108] A. Lasalmonie and J. Strudel, "Influence of grain size on the mechanical behaviour of some high strength materials," *Journal of Materials Science*, vol. 21, no. 6, pp. 1837–1852, 1986.

[109] K. Puttlitz and K. Stalter, *Handbook of lead-free solder technology for microelectronic assemblies*. CRC Press, 2004, pp. 172–174, 336.

[110] D. Frear, S. Burchett, H. Morgan, and J. Lau, *The Mechanics of Solder Alloy Interconnects*. Springer, 1994, pp. 286–288.

[111] H. Conrad, Z. Guo, Y. Fahmy, and D. Yang, "Influence of microstructure size on the plastic deformation kinetics, fatigue crack growth rate, and low-cycle fatigue of solder joints," *Journal of Electronic Materials*, vol. 28, no. 9, pp. 1062–1070, 1999.

[112] B. Chandran, W. Schmidt, and M. Gordon, "A novel bonding technique to bond CTE mismatched devices," in *IEEE Proceedings of the 46th Electronic Components and Technology Conference*, 1996, pp. 1151–1158.

[113] G. Humpston and D. Jacobson, *Principles of soldering*. ASM International, 2004, p. 39.

[114] N. Lee, *Reflow Soldering Processes and Troubleshooting: SMT, BGA, CSP, and Flip Chip Technologies*. Newnes, 2002, p. 240.

[115] W. Engelmaier, “Solder joints in electronics: design for reliability,” *Design and Reliability of Solders and Solder Interconnections*, pp. 9–19, 1997.

[116] P. Hacke, A. Sprecher, and H. Conrad, “Microstructure coarsening during thermo-mechanical fatigue of Pb-Sn solder joints,” *Journal of Electronic Materials*, vol. 26, no. 7, pp. 774–782, 1997.

[117] K. Jung and H. Conrad, “Microstructure coarsening during static annealing of 60Sn40Pb solder joints: I stereology,” *Journal of Electronic Materials*, vol. 30, no. 10, pp. 1294–1302, 2001.

[118] K. Jung and H. Conrad, “Microstructure coarsening during static annealing of 60Sn40Pb solder joints: II eutectic coarsening kinetics,” *Journal of Electronic Materials*, vol. 30, no. 10, pp. 1303–1307, 2001.

[119] K. Jung, and H. Conrad, “Microstructure coarsening during static annealing of 60Sn40Pb solder joints: III intermetallic compound growth kientics,” *Journal of Electronic Materials*, vol. 30, no. 10, pp. 1308–1312, 2001.

[120] C. LaBounty, A. Karim, X. Fan, G. Zeng, P. Abraham, Y. Okuno, and J. Bowers, “Wafer-fused thin film cooler semiconductor laser structures,” in *Proceedings of International Conference on Thermoelectrics XX*, 2001, pp. 397–400.

[121] T. McLaren, S. Kang, W. Zhang, T. Ju, and Y. Lee, “Thermosonic bonding of an optical transceiver based on an 8×8 vertical cavity surface emitting laser array,” *IEEE Transactions on Components, Packaging, and Manufacturing Technology, Part B: Advanced Packaging*, vol. 20, no. 2, pp. 152–160, 1997.

[122] P. Lawyer, D. Choudhury, M. Wetzel, and D. Rensch, “Thermosonic bonding of high-power semiconductor devices for integration with planar microstrip circuitry,” in *Proceedings of International Electronics Manufacturing Technology Symposium*. IEEE, Oct. 1998, pp. 390–393.

[123] E. Higurashi, T. Imamura, T. Suga, and R. Sawada, “Low-temperature bonding of laser diode chips on silicon substrates using plasma activation of Au films,” *IEEE Photonics Technology Letters*, vol. 19, no. 24, pp. 1994–1996, 2007.

[124] D. Tauber, M. Horita, J. Piprek, P. Abraham, A. Holmes, and J. Bowers, “The microstrip laser,” *IEEE Photonics Technology Letters*, vol. 10, no. 4, pp. 478–480, 1998.

[125] E. Higurashi, D. Chino, T. Suga, and R. Sawada, “Au-Au surface-activated bonding and its application to optical microsensors with 3-D structure,” *IEEE Journal of Selected Topics in Quantum Electronics*, vol. 15, no. 5, pp. 1500–1505, 2009.

[126] R. Takigawa, E. Higurashi, T. Suga, and T. Kawanishi, “Passive alignment and mounting of $LiNbO_3$ waveguide chips on Si substrates by low-temperature solid-state bonding of Au,” *IEEE Journal of Selected Topics in Quantum Electronics*, vol. 17, no. 3, pp. 652–658, 2011.

[127] A. Mahapatro, A. Scott, A. Manning, and D. Janes, “Gold surface with sub-nm roughness realized by evaporation on a molecular adhesion monolayer,” *Applied Physics Letters*, vol. 88, no. 15, pp. 151 917–151 917, 2006.

[128] R. Takigawa, E. Higurashi, T. Suga, and R. Sawada, “Low-temperature bonding of laser diode chips on Si substrates with oxygen and hydrogen atmospheric-pressure plasma activation,” in *IEEE International Conference on Electronic Packaging Technology & High Density Packaging*, 2009, pp. 475–477.

[129] H. Ron, S. Matlis, and I. Rubinstein, “Self-assembled monolayers on oxidized metals. 2. gold surface oxidative pretreatment, monolayer properties, and depression formation,” *Langmuir*, vol. 14, no. 5, pp. 1116–1121, 1998.

[130] Q.-Y. Tong, “Room temperature metal direct bonding,” *Applied Physics Letters*, vol. 89, no. 18, pp. 182 101:1–182 101:3, 2006.

[131] B. Heinen, F. Zhang, M. Sparenberg, B. Kunert, M. Koch, and W. Stolz, “On the measurement of the thermal resistance of vertical-external-cavity surface-emitting lasers (VECSELs),” *IEEE Journal of Quantum Electronics*, vol. 48, no. 7, pp. 934–940, 2012.

[132] M. Ettenberg, “A new dielectric facet reflector for semiconductor lasers,” *Applied Physics Letters*, vol. 32, pp. 724–725, 1978.

[133] T. Nguyen, C. Shen, X. Wu, T. Pinnington, J. Krogen, B. Witzigmann, C. Tsai, L. Cote, M. Geva, D. Huynh, A. Konkar, and P. Chen, “Design and fabrication of 1.3-μm vertical-cavity surface-emitting lasers using dielectric reflectors,” *IEEE Photonics Technology Letters*, vol. 15, no. 11, pp. 1498–1500, 2003.

[134] C. Symonds, J. Dion, I. Sagnes, M. Dainese, M. Strassner, L. Leroy, and J. Oudar, “High performance 1.55 μm vertical external cavity surface emitting laser with broadband integrated dielectric-metal mirror,” *Electronics Letters*, vol. 40, no. 12, pp. 734–735, 2004.

[135] J. Tourrenc, S. Bouchoule, A. Khadour, J. Harmand, A. Miard, J. Decobert, N. Lagay, X. Lafosse, I. Sagnes, L. Leroy, and J.-L. Oudar, “Thermal optimization of 1.55 μm OP-VECSEL with hybrid metal–metamorphic mirror for single-mode high power operation,” *Optical and Quantum Electronics*, vol. 40, no. 2, pp. 155–165, 2008.

[136] M. Devautour, , A. Michon, G. Beaudoin, I. Sagnes, L. Cerutti, and A. Garnache, "Thermal management for high power single frequency tunable diode-pumped VECSEL emitting in the near- and mid-IR," *IEEE Journal of Selected Topics in Quantum Electronics*, vol. 19, no. 4, pp. 1 701 108:1–1 701 108:8, 2013.

[137] J. Hader, T.-L. Wang, J. Yarborough, C. Dineen, Y. Kaneda, J. Moloney, B. Kunert, W. Stolz, and S. Koch, "VECSEL optimization using microscopic many-body physics," *IEEE Journal of Selected Topics in Quantum Electronics*, vol. 17, no. 6, pp. 1753–1762, 2011.

[138] J. Lloyd, "Reliability of copper metallization," Reports from Lloyd Technology Associates, Inc., http://www.nepp.nasa.gov/docuploads/A2D5D15B-6378-47E6-81C8C2DE12699E17/Reliability_of_Cu_metallization.pdf 1998, accessed 2014-07-11.

[139] R. Bedford and M. Fallahi, "Analysis of high-reflectivity metal-dielectric mirrors for edge-emitting lasers," *Optics Letters*, vol. 29, no. 9, pp. 1010–1012, 2004.

[140] Z. Zhang, T. Nakagawa, H. Takada, K. Torizuka, T. Sugaya, T. Miura, and K. Kobayashi, "Low-loss broadband semiconductor saturable absorber mirror for mode-locked Ti:Sapphire lasers," *Optics Communications*, vol. 176, no. 1, pp. 171–175, 2000.

[141] Z. Zhang, K. Torizuka, T. Itatani, K. Kobayashi, T. Sugaya, T. Nakagawa, and H. Takahashi, "Broadband semiconductor saturable-absorber mirror for a self-starting mode-locked Cr:Forsterite laser," *Optics Letters*, vol. 23, no. 18, pp. 1465–1467, 1998.

[142] Z. Zhang, T. Nakagawa, K. Torizuka, T. Sugaya, and K. Kobayashi, "Gold-reflector-based semiconductor saturable absorber mirror for femtosecond mode-locked Cr^{4+}:YAG lasers," *Applied Physics B*, vol. 70, no. 1, pp. S59–S62, 2000.

[143] J. Lloyd, J. Clemens, and R. Snede, "Copper metallization reliability," *Microelectronics Reliability*, vol. 39, no. 11, pp. 1595–1602, 1999.

[144] W. Rapson, "The bonding of gold and gold alloys to non-metallic materials," *Gold Bulletin*, vol. 12, no. 3, pp. 108–114, 1979.

[145] G. Zydzik, L. Van Uitert, S. Singh, and T. Kyle, "Strong adhesion of vacuum-evaporated gold to oxide or glass substrates," *Applied Physics Letters*, vol. 31, no. 10, pp. 697–699, 1977.

[146] K. Bacher and J. Harris, "A wet etching technique for accurate etching of GaAs/AlAs distributed bragg reflectors," *Journal of the Electrochemical Society*, vol. 142, no. 7, pp. 2386–2388, 1995.

[147] H. Lu, L. Sun, S. Ding, M. Xu, D. Zhang, and L. Wang, “Characterization of atomic-layer-deposited Al_2O_3/GaAs interface improved by NH_3 plasma pretreatment,” *Applied Physics Letters*, vol. 89, no. 15, pp. 152 910–152 910, 2006.

[148] O. Okhotnikov, Ed., *Semiconductor Disk Lasers: Physics and Technology*. John Wiley & Sons, 2010, p. 89.

[149] A. Jasik, W. Wierzchowski, J. Muszalski, J. Gaca, M. Wójcik, and K. Pierściński, “The reduction of the misfit dislocation in non-doped AlAs/GaAs DBRs,” *Journal of Crystal Growth*, vol. 311, no. 16, pp. 3975–3977, 2009.

[150] B. Saleh and M. Teich, *Fundamentals of Photonics*. Wiley Series in Pure and Applied Optics, 1991, pp. 318–321.

[151] A. Garnache, A. Ouvrard, L. Cerutti, D. Barat, A. Vicet, F. Genty, Y. Rouillard, D. Romanini, E. Cerda-Mendez, and S. de San Luis Potosi, “2–2.7 μm single frequency tunable Sb-based lasers operating in CW at RT: Microcavity and external–cavity VCSELs, DFB,” in *Proceedings of SPIE*, vol. 6184, 2006, pp. 61 840N:1–61 840N:15.

[152] R. Paschotta, “Derivation of the Schawlow-Townes linewidth of lasers,” Encyclopedia of Laser Physics and Technology, http://www.rp-photonics.com/Schawlow-Townes_linewidth.pdf accessed on 2014-10-14.

[153] R. Paschotta, “Linewidth,” Encyclopedia of Laser Physics and Technology, http://www.rp-photonics.com/linewidth_enhancement_factor.html accessed 2014-10-14.

[154] C. Henry, “Theory of the linewidth of semiconductor lasers,” *IEEE Journal of Quantum Electronics*, vol. 18, no. 2, pp. 259–264, 1982.

[155] A. Ouvrard, A. Garnache, L. Cerutti, F. Genty, and D. Romanini, “Single-frequency tunable Sb-based VCSELs emitting at 2.3 μm,” *IEEE Photonics Technology Letters*, vol. 17, no. 10, pp. 2020–2022, 2005.

[156] A. Garnache, A. Ouvrard, and D. Romanini, “Single–frequency operation of external–cavity VCSELs: Non-linear multimode temporal dynamics and quantum limit.” *Optics Express*, vol. 15, no. 15, pp. 9403–9417, 2007.

[157] F. Zhang, B. Heinen, M. Wichmann, C. Möller, B. Kunert, A. Rahimi-Iman, W. Stolz, and M. Koch, “A 23-watt single-frequency vertical-external-cavity surface-emitting laser,” *Optics Express*, vol. 22, no. 11, pp. 12 817–12 822, 2014.

[158] A. Laurain, C. Mart, J. Hader, J. V. Moloney, B. Kunert, and W. Stolz, "Optical noise of stabilized high-power single frequency optically pumped semiconductor laser," *Optics Letters*, vol. 39, no. 6, pp. 1573–1576, 2014.

[159] A. Laurain, M. Myara, G. Beaudoin, I. Sagnes, and A. Garnache, "Multiwatt–power highly–coherent compact single–frequency tunable vertical–external–cavity–surface–emitting–semiconductor–laser," *Optics Express*, vol. 18, no. 14, pp. 14 627–14 636, 2010.

[160] M. Myara, M. Sellahi, A. Laurain, A. Michon, I. Sagnes, and A. Garnache, "Noise properties of NIR and MIR VECSELs," in *Proceedings of SPIE*, vol. 8606, 2013, pp. 86 060Q:1–86 060Q:13.

[161] S. Spießberger, M. Schiemangk, A. Sahm, A. Wicht, H. Wenzel, A. Peters, G. Erbert, and G. Tränkle, "Micro-integrated 1 watt semiconductor laser system with a linewidth of 3.6 kHz," *Optics Express*, vol. 19, no. 8, pp. 7077–7083, 2011.

[162] A. Garnache, V. Lecocq, L. Ferrières, A. Benselama, M. Myara, L. Cerutti, I. Sagnes, and S. Denet, "Industrial integration of high coherence tunable VECSEL in the NIR and MIR," in *Proceedings of SPIE*, vol. 8966, 2014, pp. 89 660V:1–89 660V:10.

[163] M. Raja, S. Brueck, M. Osiński, C. Schaus, J. McInerney, T. Brennan, and B. Hammons, "Novel wavelength-resonant optoelectronic structure and its application to surface-emitting semiconductor lasers," *Electronics Letters*, vol. 24, no. 18, pp. 1140–1142, 1988.

[164] B. Cocquelin, D. Holleville, G. Lucas-Leclin, I. Sagnes, A. Garnache, M. Myara, and P. Georges, "Tunable single-frequency operation of a diode-pumped vertical external-cavity laser at the cesium D_2 line," *Applied Physics B: Lasers and Optics*, vol. 95, no. 2, pp. 315–321, 2009.

[165] M. Jacquemet, M. Domenech, G. Lucas-Leclin, P. Georges, J. Dion, M. Strassner, I. Sagnes, and A. Garnache, "Single-frequency cw vertical external cavity surface emitting semiconductor laser at 1003 nm and 501 nm by intracavity frequency doubling," *Applied Physics B: Lasers and Optics*, vol. 86, no. 3, pp. 503–510, 2007.

[166] F. Camargo, S. Janicot, I. Sagnes, A. Garnache, P. Georges, and G. Lucas-Leclin, "Evaluation of the single-frequency operation of a short vertical external-cavity semiconductor laser at 852 nm," in *Proceesings of SPIE*, vol. 8242, 2012, pp. 82 420F:1–82 420F:8.

[167] Y. Kaneda, M. Fallahi, J. Hader, J. Moloney, S. Koch, B. Kunert, and W. Stoltz, "Continuous-wave single-frequency 295 nm laser source by a frequency-quadrupled

optically pumped semiconductor laser," *Optics Letters*, vol. 34, no. 22, pp. 3511–3513, 2009.

[168] H. Lindberg, A. Larsson, and M. Strassner, "Single-frequency operation of a high-power, long-wavelength semiconductor disk laser," *Optics Letters*, vol. 30, no. 17, pp. 2260–2262, 2005.

[169] B. Rösener, M. Rattunde, R. Moser, S. Kaspar, T. Töpper, C. Manz, K. Köhler, and J. Wagner, "Continuous-wave room-temperature operation of a 2.8 μm GaSb-based semiconductor disk laser," *Optics Letters*, vol. 36, no. 3, pp. 319–321, 2011.

[170] B. Rösener, S. Kaspar, M. Rattunde, T. Töpper, C. Manz, K. Köhler, O. Ambacher, and J. Wagner, "2 μm semiconductor disk laser with a heterodyne linewidth below 10 kHz," *Optics Letters*, vol. 36, no. 18, pp. 3587–3589, 2011.

[171] S. Kaspar, M. Rattunde, T. Topper, C. Manz, K. Kohler, and J. Wagner, "Semiconductor disk laser at 2.05 μm wavelength with $<$ 100 kHz linewidth at 1 W output power," *Applied Physics Letters*, vol. 100, no. 3, pp. 031 109–031 109, 2012.

[172] T. Okoshi, K. Kikuchi, and A. Nakayama, "Novel method for high resolution measurement of laser output spectrum," *Electronics Letters*, vol. 16, no. 16, pp. 630–631, 1980.

[173] M. Han and A. Wang, "Analysis of a loss-compensated recirculating delayed self-heterodyne interferometer for laser linewidth measurement," *Applied Physics B*, vol. 81, no. 1, pp. 53–58, 2005.

[174] L. Richter, H. Mandelberg, M. Kruger, and P. McGrath, "Linewidth determination from self-heterodyne measurements with subcoherence delay times," *IEEE Journal of Quantum Electronics*, vol. 22, no. 11, pp. 2070–2074, 1986.

[175] P. Horak and W. Loh, "On the delayed self-heterodyne interferometric technique for determining the linewidth of fiber lasers," *Optics Express*, vol. 14, no. 9, pp. 3923–3928, 2006.

[176] M. Van Exter, S. Kuppens, and J. Woerdman, "Excess phase noise in self-heterodyne detection," *IEEE Journal of Quantum Electronics*, vol. 28, no. 3, pp. 580–584, 1992.

[177] J. Geng, C. Spiegelberg, and S. Jiang, "Narrow linewidth fiber laser for 100-km optical frequency domain reflectometry," *IEEE Photonics Technology Letters*, vol. 17, no. 9, pp. 1827–1829, 2005.

[178] C. Akcay, P. Parrein, and J. Rolland, "Estimation of longitudinal resolution in optical coherence imaging," *Applied Optics*, vol. 41, no. 25, pp. 5256–5262, 2002.

[179] C. Wilmsen, H. Temkin, and L. Coldren, *Vertical-cavity surface-emitting lasers: design, fabrication, characterization, and applications*. Cambridge University Press, 2001, vol. 24, Chapter 4.

[180] J. Tourrenc, S. Bouchoule, A. Khadour, J. Decobert, A. Miard, J. Haimand, and X. Oudar, "High power single-longitudinal-mode OP-VECSEL at 1.55 μm with hybrid metal-metamorphic Bragg mirror," *Electronics Letters*, vol. 43, no. 14, pp. 754–755, 2007.

[181] J. Dudley, M. Ishikawa, D. Babic, B. Miller, R. Mirin, W. Jiang, J. Bowers, and E. Hu, "144 °C operation of 1.3 μm InGaAsP vertical cavity lasers on GaAs substrates," *Applied Physics Letters*, vol. 61, no. 26, pp. 3095–3097, 1992.

[182] D. Babić, J. Dudley, K. Streubel, R. Mirin, E. Hu, and J. Bowers, "Optically pumped all-epitaxial wafer-fused 1.52 μm vertical-cavity lasers," *Electronics Letters*, vol. 30, no. 9, pp. 704–706, 1994.

[183] J. Lyytikäinen, J. Rautiainen, L. Toikkanen, A. Sirbu, A. Mereuta, A. Caliman, E. Kapon, and O. Okhotnikov, "1.3-μm optically-pumped semiconductor disk laser by wafer fusion," *Optics Express*, vol. 17, no. 11, pp. 9047–9052, 2009.

[184] J. Rautiainen, J. Lyytikäinen, A. Sirbu, A. Mereuta, A. Caliman, E. Kapon, and O. Okhotnikov, "2.6 W optically-pumped semiconductor disk laser operating at 1.57-μm using wafer fusion," *Optics Express*, vol. 16, no. 26, pp. 21 881–21 886, 2008.

[185] G. Celler and S. Cristoloveanu, "Frontiers of silicon-on-insulator," *Journal of Applied Physics*, vol. 93, no. 9, pp. 4955–4978, 2003.

[186] W. Noell, P.-A. Clerc, L. Dellmann, B. Guldimann, H.-P. Herzig, O. Manzardo, C. R. Marxer, K. J. Weible, R. Dandliker, and N. de Rooij, "Applications of SOI-based optical MEMS," *IEEE Journal of Selected Topics in Quantum Electronics*, vol. 8, no. 1, pp. 148–154, 2002.

[187] G. Herrera, T. Bauer, M. Blain, P. Dodd, R. Dondero, E. Garcia, P. Galambos, D. Hetherington, J. Hudgens, F. McCormick, G. Nielson, C. Nordquist, M. Okandan, R. Olsson, K. Ortiz, M. Platzbecker, P. Resnick, R. Shul, M. Shaw, C. Sullivan, and M. Watts, "SOI-enabled MEMS processes lead to novel mechanical, optical, and atomic physics devices," in *Proceedings of IEEE International SOI Conference*. IEEE, 2008, pp. 5–8.

[188] S. Christiansen, R. Singh, and U. Gosele, "Wafer direct bonding: From advanced substrate engineering to future applications in micro/nanoelectronics," in *Proceedings of IEEE*, vol. 94, no. 12, 2006, pp. 2060–2106.

[189] G. Roelkens, J. Van Campenhout, J. Brouckaert, D. Van Thourhout, R. Baets, P. Romeo, P. Regreny, A. Kazmierczak, C. Seassal, X. Letartre, G. Hollinger, J. Fedeli, L. Cioccio, and C. Lagahe-Blanchard, "III-V/Si photonics by die-to-wafer bonding," *Materials Today*, vol. 10, no. 7-8, pp. 36–43, 2007.

[190] D. Liang and J. Bowers, "Photonic integration: Si or InP substrates?" *Electronics Letters*, vol. 45, no. 12, pp. 578–581, 2009.

[191] D. Liang, and J. Bowers, "Recent progress in lasers on silicon," *Nature Photonics*, vol. 4, no. 8, pp. 511–517, 2010.

[192] O. Moutanabbir and U. Gösele, "Heterogeneous integration of compound semiconductors," *Annual Review of Materials Research*, vol. 40, pp. 469–500, 2010.

[193] Z.-H. Zhu, F. E. Ejeckam, Y. Qian, J. Zhang, Z. Zhang, G. L. Christenson, and Y. Lo, "Wafer bonding technology and its applications in optoelectronic devices and materials," *IEEE Journal of Selected Topics in Quantum Electronics*, vol. 3, no. 3, pp. 927–936, 1997.

[194] A. Black, A. Hawkins, N. Margalit, D. Babic, J. AL Holmes, Y.-L. Chang, P. Abraham, J. E. Bowers, and E. Hu, "Wafer fusion: materials issues and device results," *IEEE Journal of Selected Topics in Quantum Electronics*, vol. 3, no. 3, pp. 943–951, 1997.

[195] F. Dimroth, M. Grave, P. Beutel, U. Fiedeler, C. Karcher, T. N. Tibbits, E. Oliva, G. Siefer, M. Schachtner, A. Wekkeli *et al.*, "Wafer bonded four-junction GaInP/GaAs//GaInAsP/GaInAs concentrator solar cells with 44.7% efficiency," *Progress in Photovoltaics: Research and Applications*, vol. 22, no. 3, pp. 277–282, 2014.

[196] Q. Tong and U. Gösele, "Wafer bonding and layer splitting for microsystems," *Advanced Materials*, vol. 11, no. 17, pp. 1409–1425, 1999.

[197] Q.-Y. Tong, G. Fountain, and P. Enquist, "Room temperature SiO_2/SiO_2 covalent bonding," *Applied Physics Letters*, vol. 89, no. 4, pp. 042 110:1–042 110:3, 2006.

[198] Q.-Y. Tong, E. Schmidt, U. Gosele, and M. Reiche, "Hydrophobic silicon wafer bonding," *Applied Physics Letters*, vol. 64, no. 5, pp. 625–627, 1994.

[199] K. Ljungberg, A. Söderbärg, and Y. Backlund, "Spontaneous bonding of hydrophobic silicon surfaces," *Applied Physics Letters*, vol. 62, no. 12, pp. 1362–1364, 1993.

[200] Q.-Y. Tong, T.-H. Lee, U. Gösele, M. Reiche, J. Ramm, and E. Beck, "The role of surface chemistry in bonding of standard silicon wafers," *Journal of The Electrochemical Society*, vol. 144, no. 1, pp. 384–389, 1997.

[201] Z. Liau and D. Mull, "Wafer fusion: A novel technique for optoelectronic device fabrication and monolithic integration," *Applied Physics Letters*, vol. 56, no. 8, pp. 737–739, 1990.

[202] Y. Lo, R. Bhat, D. Hwang, M. Koza, and T. Lee, "Bonding by atomic rearrangement of InP/InGaAsP 1.5 μm wavelength lasers on GaAs substrates," *Applied Physics Letters*, vol. 58, no. 18, pp. 1961–1963, 1991.

[203] R. Ram, J. Dudley, J. Bowers, L. Yang, K. Carey, and S. Rosner, "GaAs to InP wafer fusion," *Journal of Applied Physics*, vol. 78, no. 6, pp. 4227–4237, 1995.

[204] R. Horng, W. Peng, D. Wuu, W. Ho, and Y. Huang, "Surface treatment and electrical properties of directly wafer-bonded InP epilayer on GaAs substrate," *Solid-State Electronics*, vol. 46, no. 8, pp. 1103–1108, 2002.

[205] A. Mircea, A. Caliman, V. Iakovlev, A. Mereuta, G. Suruceanu, C.-A. Berseth, P. Royo, A. Syrbu, and E. Kapon, "Cavity mode-gain peak tradeoff for 1320-nm wafer-fused VCSELs with 3-mW single-mode emission power and 10-Gb/s modulation speed up to 70 °C," *IEEE Photonics Technology Letters*, vol. 19, no. 2, pp. 121–123, 2007.

[206] A. Syrbu, A. Mircea, A. Mereuta, A. Caliman, C.-A. Berseth, G. Suruceanu, V. Iakovlev, M. Achtenhagen, A. Rudra, and E. Kapon, "1.5-mW single-mode operation of wafer-fused 1550-nm VCSELs," *IEEE Photonics Technology Letters*, vol. 16, no. 5, pp. 1230–1232, 2004.

[207] A. Sirbu, A. Mereuta, A. Caliman, N. Volet, Q. Zhu, V. Iakovlev, J. Rautiainen, J. Lyytikäinen, O. Okhotnikov, J. Walczak, M. Wasiak, T. Czyszanowski, and E. Kapon, "High power optically pumped VECSELs emitting in 1310-nm and 1550-nm bands," in *Proceedings of SPIE*, vol. 7919, 2011, pp. 791 903:1–791 903:11.

[208] T. Akatsu, A. Plößl, R. Scholz, H. Stenzel, and U. Gösele, "Wafer bonding of different III–V compound semiconductors by atomic hydrogen surface cleaning," *Journal of Applied Physics*, vol. 90, p. 3856, 2001.

[209] S. Ogawa, M. Imada, and S. Noda, "Analysis of thermal stress in wafer bonding of dissimilar materials for the introduction of an InP-based light emitter into a GaAs-based three-dimensional photonic crystal," *Applied Physics Letters*, vol. 82, no. 20, pp. 3406–3408, 2003.

[210] C.-T. Ko and K.-N. Chen, "Low temperature bonding technology for 3D integration," *Microelectronics Reliability*, vol. 52, no. 2, pp. 302–311, 2012.

[211] I. Radu, "In memoriam Ulrich Gösele: Wafer bonding á la carte," in *Electrochemical Society Meeting Abstracts*, no. 27, 2010, pp. 1742–1742.

[212] U. Gösele and Q. Tong, "Semiconductor wafer bonding," *Annual review of materials science*, vol. 28, no. 1, pp. 215–241, 1998.

[213] D. Liang and J. Bowers, "Highly efficient vertical outgassing channels for low-temperature InP-to-silicon direct wafer bonding on the silicon-on-insulator substrate," *Journal of Vacuum Science & Technology B*, vol. 26, no. 4, pp. 1560–1568, 2008.

[214] S. Hayashi, D. Bruno, R. Sandhu, and M. Goorsky, "Wafer bonding for III–V on insulator structures," *Journal of Electronic Materials*, vol. 32, no. 8, pp. 877–881, 2003.

[215] D. Liang, A. Fang, H. Park, T. Reynolds, K. Warner, D. Oakley, and J. Bowers, "Low-temperature, strong SiO_2-SiO_2 covalent wafer bonding for III–V compound semiconductors-to-silicon photonic integrated circuits," *Journal of Electronic Materials*, vol. 37, no. 10, pp. 1552–1559, 2008.

[216] F. Niklaus, G. Stemme, J.-Q. Lu, and R. Gutmann, "Adhesive wafer bonding," *Journal of Applied Physics*, vol. 99, no. 3, pp. 031 101:1–031 101:28, 2006.

[217] G. Kräuter, A. Schumacher, U. Gösele, T. Jaworek, and G. Wegner, "Room temperature silicon wafer bonding with ultra-thin polymer films," *Advanced Materials*, vol. 9, no. 5, pp. 417–420, 1997.

[218] G. Kräuter, Y. Bluhm, C. Batz-Sohn, and U. Gösele, "The joining of parallel plates via organic monolayers: chemical reactions in a spatially confined system," *Advanced Materials*, vol. 11, no. 12, pp. 1035–1038, 1999.

[219] J. Haisma, N. Hattu, J. Pulles, E. Steding, and J. Vervest, "Direct bonding and beyond," *Applied Optics*, vol. 46, no. 27, pp. 6793–6803, 2007.

[220] D. Pasquariello and K. Hjort, "Plasma-assisted InP-to-Si low temperature wafer bonding," *IEEE Journal of Selected Topics in Quantum Electronics*, vol. 8, no. 1, pp. 118–131, 2002.

[221] T. Suni, K. Henttinen, I. Suni, and J. Mäkinen, "Effects of plasma activation on hydrophilic bonding of Si and SiO_2," *Journal of the Electrochemical Society*, vol. 149, no. 6, pp. G348–G351, 2002.

[222] X. Lin, G. Liao, Z. Tang, and T. Shi, "UV surface exposure for low temperature hydrophilic silicon direct bonding," *Microsystem Technologies*, vol. 15, no. 2, pp. 317–321, 2009.

[223] S. Ranta, T. Hakkarainen, M. Tavast, J. Lindfors, T. Leinonen, and M. Guina, "Strain compensated 1120 nm GaInAs/GaAs vertical external-cavity surface-emitting laser grown by molecular beam epitaxy," *Journal of Crystal Growth*, vol. 335, no. 1, pp. 4–9, 2011.

[224] L. Fan, C. Hessenius, M. Fallahi, J. Hader, H. Li, J. Moloney, W. Stolz, S. Koch, J. Murray, and R. Bedford, "Highly strained InGaAs/GaAs multiwatt vertical-external-cavity surface-emitting laser emitting around 1170 nm," *Applied Physics Letters*, vol. 91, pp. 131 114:1–1 311 141:3, 2007.

[225] T. Jouhti, C. Peng, E. Pavelescu, J. Konttinen, L. Gomes, O. Okhotnikov, and M. Pessa, "Strain-compensated GaInNAs structures for 1.3-μm lasers," *IEEE Journal of Selected Topics in Quantum Electronics*, vol. 8, no. 4, pp. 787–794, 2002.

[226] A. Albrecht, T. Rotter, C. Hains, A. Stintz, J. Moloney, K. Malloy, and G. Balakrishnan, "Multi-watt 1.25 μm quantum dot VECSEL," *Electronics Letters*, vol. 46, no. 12, pp. 856–857, 2010.

[227] A. Rantamaki, J. Rautiainen, L. Toikkanen, I. Krestnikov, M. Butkus, E. U. Rafailov, and O. Okhotnikov, "Flip chip quantum-dot semiconductor disk laser at 1200 nm," *IEEE Photonics Technology Letters*, vol. 24, no. 15, pp. 1292–1294, 2012.

[228] G. Adolfsson, S. Wang, M. Sadeghi, and A. Larsson, "High-performance long-wavelength InGaAs/GaAs multiple quantum-well lasers grown by molecular beam epitaxy," *Electronics Letters*, vol. 43, no. 8, pp. 454–456, 2007.

[229] A. Albrecht, C. Hains, T. Rotter, A. Stintz, K. Malloy, G. Balakrishnan, and J. Moloney, "High power 1.25 μm InAs quantum dot vertical external-cavity surface-emitting laser," *Journal of Vacuum Science & Technology B*, vol. 29, no. 3, pp. 03C113:1–03C113:4, 2011.

[230] A. Albrecht, T. Rotter, C. Hains, A. Stintz, G. Xin, T.-L. Wang, Y. Kaneda, J. Moloney, K. Malloy, and G. Balakrishnan, "High-power 1.25 μm InAs QD VECSEL based on resonant periodic gain structure," in *Proceedings of SPIE*, vol. 7919, 2011, pp. 791 904:1–791 904:6.

[231] J.-M. Hopkins, S. Smith, C. Jeon, H. Sun, D. Burns, S. Calvez, M. Dawson, T. Jouhti, and M. Pessa, "0.6 W CW GaInNAs vertical external-cavity surface emitting laser operating at 1.32 μm," *Electronics Letters*, vol. 40, no. 1, pp. 30–31, 2004.

[232] E. Le Ru, P. Howe, T. Jones, and R. Murray, "Strain-engineered InAs/GaAs quantum dots for long-wavelength emission," *Physical Review B*, vol. 67, no. 16, pp. 165 303:1–165 303:5, 2003.

[233] V.-M. Korpijärvi, M. Guina, J. Puustinen, P. Tuomisto, J. Rautiainen, A. Härkönen, A. Tukiainen, O. Okhotnikov, and M. Pessa, "MBE grown GaInNAs-based multi-watt disk lasers," *Journal of Crystal Growth*, vol. 311, no. 7, pp. 1868–1871, 2009.

[234] A. Sirbu, A. Rantamäki, E. J. Saarinen, V. Iakovlev, A. Mereuta, J. Lyytikäinen, A. Caliman, N. Volet, O. G. Okhotnikov, and E. Kapon, "High performance wafer-fused semiconductor disk lasers emitting in the 1300 nm waveband," *Optics Express*, vol. 22, no. 24, pp. 29 398–29 403, 2014.

[235] K. Black, P. Abraham, A. Karim, J. Bowers, and E. Hu, "Improved luminescence from InGaAsP/InP MQW active regions using a wafer fused superlattice barrier," in *IEEE 11th International Conference on Indium Phosphide and Related Materials (IPRM)*, 1999, pp. 357–360.

[236] I. Bakish, V. Artel, T. Ilovitsh, M. Shubely, Y. Ben-Ezra, A. Zadok, and C. Sukenik, "Self-assembled monolayer assisted bonding of Si and InP," *Optics Materials Express*, vol. 2, pp. 1141–1148, 2012.

[237] J. Heikkinen, R. Gumenyuk, A. Rantamäki, T. Leinonen, M. Melkumov, E. M. Dianov, and O. G. Okhotnikov, "A 1.33 μm picosecond pulse generator based on semiconductor disk mode-locked laser and bismuth fiber amplifier," *Optics Express*, vol. 22, no. 10, pp. 11 446–11 455, 2014.

[238] H. Lindberg, M. Strassner, J. Bengtsson, and A. Larsson, "InP-based optically pumped VECSEL operating CW at 1550 nm," *IEEE Photonics Technology Letters*, vol. 16, no. 2, pp. 362–364, 2004.

[239] H. Lindberg, M. Strassner, E. Gerster, and A. Larsson, "0.8 W optically pumped vertical external cavity surface emitting laser operating CW at 1550 nm," *Electronics Letters*, vol. 40, no. 10, pp. 601–602, 2004.

[240] G. Baili, L. Morvan, G. Pillet, S. Bouchoule, Z. Zhao, J.-L. Oudar, L. Ménager, S. Formont, F. Van Dijk, M. Faugeron, M. Alouini, F. Bretenaker, and D. Dolfi, "Ultralow noise and high-power VECSEL for high dynamic range and broadband RF/optical links," *Journal of Lightwave Technology*, vol. 32, no. 20, pp. 3489–3494, 2014.

[241] G. Genty, M. Kaivola, and H. Ludvigsen, “Measurements of linewidth variations within external-cavity modes of a grating-cavity laser,” *Optics Communications*, vol. 203, no. 3, pp. 295–300, 2002.

[242] L. Mercer, “1/f frequency noise effects on self-heterodyne linewidth measurements,” *Journal of Lightwave Technology*, vol. 9, no. 4, pp. 485–493, 1991.

[243] H. Ludvigsen, M. Tossavainen, and M. Kaivola, “Laser linewidth measurements using self-homodyne detection with short delay,” *Optics Communications*, vol. 155, no. 1, pp. 180–186, 1998.

[244] T. Baer, “Large-amplitude fluctuations due to longitudinal mode coupling in diode-pumped intracavity-doubled Nd:YAG lasers,” *Journal of Optical Society of America B*, vol. 3, no. 9, pp. 1175–1180, 1986.

[245] D. Anthon, D. Sipes, T. Pier, and M. Ressl, “Intracavity doubling of CW diode-pumped Nd:YAG lasers with KTP,” *IEEE Journal of Quantum Electronics*, vol. 28, no. 4, pp. 1148–1157, 1992.

[246] G. James, C. Bracikowski, K. Wiesenfeld, E. Harrell, and R. Roy, “Elimination of chaos in an intracavity-doubled Nd:YAG laser,” *Optics Letters*, vol. 15, no. 20, pp. 1141–1143, 1990.

[247] “Introducing the Verdi G10, Technology proven in the most noise sensitive applications,” Coherent Inc, white paper, https://www.coherent.com/downloads/VerdiG10WhitePaperRevFINAL.pdf, accessed 2014-10-14.

[248] R. Hartke, E. Heumann, G. Huber, M. Kühnelt, and U. Steegmüller, “Efficient green generation by intracavity frequency doubling of an optically pumped semiconductor disk laser,” *Applied Physics B*, vol. 87, no. 1, pp. 95–99, 2007.

[249] R. Hartke, V. Baev, K. Seger, O. Back, E. Heumann, G. Huber, M. Kühnelt, and U. Steegmüller, “Experimental study of the output dynamics of intracavity frequency doubled optically pumped semiconductor disk lasers,” *Applied Physics Letters*, vol. 92, no. 10, pp. 101 107:1–101 107:3, 2008.

[250] E. Kantola, T. Leinonen, S. Ranta, M. Tavast, and M. Guina, “High-efficiency 20 W yellow VECSEL,” *Optics Express*, vol. 22, no. 6, pp. 6372–6380, 2014.

[251] Q.-Z. Shu, A. Caprara, J. Berger, D. Anthon, H. Jerman, and L. Spinelli, “Intracavity-tripled optically-pumped semiconductor laser at 355 nm,” in *Proceedings of SPIE*, vol. 7193, 2009, pp. 719 319:1–719 319:7.

[252] Y. Kaneda, J. Yarborough, L. Li, N. Peyghambarian, L. Fan, C. Hessenius, M. Fallahi, J. Hader, J. Moloney, Y. Honda, M. Nishioka, Y. Shimizu, K. Miyazono, H. Shimatani, M. Yoshimura, Y. Mori, Y. Kitaoka, and T. Sasaki, "Continuous-wave all-solid-state 244 nm deep-ultraviolet laser source by fourth-harmonic generation of an optically pumped semiconductor laser using $CsLiB_6O_{10}$ in an external resonator," *Optics Letters*, vol. 33, no. 15, pp. 1705–1707, 2008.

[253] M. Scheller, J. Yarborough, J. Moloney, M. Fallahi, M. Koch, and S. Koch, "Room temperature continuous wave milliwatt terahertz source," *Optics Express*, vol. 18, no. 26, pp. 27 112–27 117, 2010.

[254] J. Paul, M. Scheller, A. Laurain, A. Young, S. Koch, and J. Moloney, "Narrow linewidth single-frequency terahertz source based on difference frequency generation of vertical-external-cavity source-emitting lasers in an external resonance cavity," *Optics Letters*, vol. 38, no. 18, pp. 3654–3657, 2013.

[255] A. Härkonen, J. Rautiainen, T. Leinonen, Y. A. Morozov, L. Orsila, M. Guina, M. Pessa, and O. G. Okhotnikov, "Intracavity sum-frequency generation in dual-wavelength semiconductor disk laser," *IEEE Photonics Technology Letters*, vol. 19, no. 19, pp. 1550–1552, 2007.

[256] M. Andersen, P. Schlosser, J. Hastie, P. Tidemand-Lichtenberg, M. Dawson, and C. Pedersen, "Singly-resonant sum frequency generation of visible light in a semiconductor disk laser," *Optics Express*, vol. 17, no. 8, pp. 6010–6017, 2009.

[257] D. Parrotta, A. Kemp, M. Dawson, and J. Hastie, "Multi-watt, continuous-wave, tunable diamond Raman laser with intracavity frequency doubling to the visible," *IEEE Journal of Selected Topics in Quantum Electronics*, vol. 19, no. 4, pp. 1 400 108:1–1 400 108:8, 2013.

[258] D. Stothard, M. Ebrahimzadeh, and M. Dunn, "Low-pump-threshold continuous-wave singly resonant optical parametric oscillator," *Optics Letters*, vol. 23, no. 24, pp. 1895–1897, 1998.

[259] D. J. Stothard and M. H. Dunn, "Relaxation oscillation suppression in continuous-wave intracavity optical parametric oscillators," *Optics Express*, vol. 18, no. 2, pp. 1336–1348, 2010.

[260] D. Stothard, J. Hopkins, D. Burns, and M. Dunn, "Stable, continuous-wave, intracavity, optical parametric oscillator pumped by a semiconductor disk laser (VECSEL)." *Optics Express*, vol. 17, no. 13, pp. 10 648–10 658, 2009.

[261] A. Caprara, "2 W CW OPO in mid-IR pumped by OPSL laser intra-cavity radiation," in *Proceedings of SPIE*, vol. 7919, 2011, pp. 79 190A:1–79 190A:13.

[262] N. Hempler, G. Robertson, C. Hamilton, G. T. Maker, and G. P. Malcolm, "Advances in narrow-linewidth continuous wave semiconductor disk laser pumped optical parametric oscillators," in *Proceedings of SPIE*, vol. 8242, 2012, pp. 82 420J:1–82 420J:8.

[263] M. Siltanen, T. Leinonen, and L. Halonen, "Decreased oscillation threshold of a continuous-wave OPO using a semiconductor gain mirror," *Optics Express*, vol. 19, no. 20, pp. 19 675–19 680, 2011.

[264] W. Risk, T. Gosnell, and A. Nurmikko, *Compact blue-green lasers*. Cambridge University Press, 2003.

[265] C. Webb and J. Jones, *Handbook of Laser Technology and Applications: Laser design and laser systems*. CRC Press, 2004, vol. 2, C3.1.

[266] R. Boyd, *Nonlinear optics*. Elsevier, 2008.

[267] W. Koechner, *Solid-state laser engineering*, 6th ed. Springer, 2006, Chapter 10.

[268] G. Boyd, A. Ashkin, J. Dziedzic, and D. Kleinman, "Second-harmonic generation of light with double refraction," *Physical Review*, vol. 137, no. 4A, pp. A1305–A1320, 1965.

[269] A. Smith, D. Armstrong, and W. Alford, "Increased acceptance bandwidths in optical frequency conversion by use of multiple walk-off-compensating nonlinear crystals," *Journal of Optical Society of America B*, vol. 15, no. 1, pp. 122–141, 1998.

[270] R. Smith, "Theory of intracavity optical second-harmonic generation," *IEEE Journal of Quantum Electronics*, vol. 6, no. 4, pp. 215–223, 1970.

[271] J.-Y. Kim and J. Shim, "An analytical model of the intracavity optical second harmonic generation in a vertical-external-cavity surface-emitting laser," *IEEE Journal of Quantum Electronics*, vol. 44, no. 8, pp. 755–762, 2008.

[272] J. Bartschke, R. Knappe, K.-J. Boller, and R. Wallenstein, "Investigation of efficient self-frequency-doubling Nd:YAB lasers," *IEEE Journal of Quantum Electronics*, vol. 33, no. 12, pp. 2295–2300, 1997.

[273] A. Hein, S. Menzel, and P. Unger, "High-power high-efficiency optically pumped semiconductor disk lasers in the green spectral region with a broad tuning range," *Applied Physics Letters*, vol. 101, no. 11, pp. 111 109:1–111 109:4, 2012.

[274] T. Kellner, F. Heine, and G. Huber, “Efficient laser performance of Nd:YAG at 946 nm and intracavity frequency doubling with $LiJO_3$, β-BaB_2O_4, and LiB_3O_5,” *Applied Physics B: Lasers and Optics*, vol. 65, no. 6, pp. 789–792, 1997.

[275] J. Geusic, H. Levinstein, S. Singh, R. Smith, and L. Van Uitert, “Continuous 0.532-μm solid-state source using $Ba_2NaNb_5O_{15}$,” *Applied Physics Letters*, vol. 12, no. 9, pp. 306–308, 1968.

[276] J. Hastie, L. Morton, A. Kemp, M. Dawson, A. Krysa, and J. Roberts, “Tunable ultraviolet output from an intracavity frequency-doubled red vertical-external-cavity surface-emitting laser,” *Applied Physics Letters*, vol. 89, no. 6, pp. 061 114:1–061 114:3, 2006.

[277] P. Schlosser, J. Hastie, S. Calvez, A. Krysa, and M. Dawson, “InP/AlGaInP quantum dot semiconductor disk lasers for CW TEM_{00} emission at 716–755 nm,” *Optics Express*, vol. 17, no. 24, pp. 21 782–21 787, 2009.

[278] M. Heilemann, S. van de Linde, M. Schüttpelz, R. Kasper, B. Seefeldt, A. Mukherjee, P. Tinnefeld, and M. Sauer, “Subdiffraction-resolution fluorescence imaging with conventional fluorescent probes,” *Angewandte Chemie International Edition*, vol. 47, no. 33, pp. 6172–6176, 2008.

[279] D. Shcherbakova, O. Subach, and V. Verkhusha, “Red fluorescent proteins: advanced imaging applications and future design,” *Angewandte Chemie International Edition*, vol. 51, no. 43, pp. 10 724–10 738, 2012.

[280] J. Chilla, H. Zhou, E. Weiss, A. Caprara, Q. Shou, S. Govorkov, M. Reed, and L. Spinelli, “Blue and green optically-pumped semiconductor lasers for display,” in *Proceedings of SPIE*, vol. 5740, 2005, pp. 41–47.

[281] C. Kannengiesser, W. Seelert, V. Ostroumov, R. von Elm, S. Hilbich, M. Bracker, and J. Lindfors, “Ultra-narrow bandwidth OPS laser in the green-yellow wavelength range for Raman spectroscopy,” in *Proceedings of SPIE*, vol. 7193, 2009, pp. 71 931A:1–71 931A:8.

[282] J. Tedesco and J. Slater, “785-nm laser benefits Raman spectroscopy,” *Laser Focus World*, Sept. 2000.

[283] J. Lee, S. Lee, T. Kim, and Y. Park, “7 W high-efficiency continuous-wave green light generation by intracavity frequency doubling of an end-pumped vertical external-cavity surface emitting semiconductor laser,” *Applied Physics Letters*, vol. 89, pp. 241 107:1–241 107:3, 2006.

[284] J. Kim, S. Cho, S. Lee, G. Kim, J. Lee, J. Yoo, K. Kim, T. Kim, and Y. Park, "Highly efficient green VECSEL with intra-cavity diamond heat spreader," *Electronics Letters*, vol. 43, no. 2, pp. 105–107, 2007.

[285] J. Bartschke, K. Boller, R. Wallenstein, I. Klimov, V. Tsvetkov, and I. Shcherbakov, "Diode-pumped passively Q-switched self-frequency-doubling Nd:YAB laser," *Journal of the Optical Society of America B*, vol. 14, no. 12, pp. 3452–3456, 1997.

[286] C. Wang, L. Reekie, Y. Chow, and W. Gambling, "Efficient blue light generation from a diode laser pumped Nd:YAG laser," *Optics Communications*, vol. 167, no. 1, pp. 155–158, 1999.

Tampereen teknillinen yliopisto
PL 527
33101 Tampere

Tampere University of Technology
P.O.B. 527
FI-33101 Tampere, Finland

ISBN 978-952-15-3480-5
ISSN 1459-2045